Characterising Internal Tides in a Region of Dynamic Circulation: The East Australian Current at 27oS

Author:
Vitarelli De Queiroz, Eduardo

Publication Date:
2021

DOI:
https://doi.org/10.26190/unsworks/1990

Thesis/Dissertation Sheet

Surname/Family Name	:	**Vitarelli de Queiroz**
Given Name/s	:	**Eduardo**
Abbreviation for degree as given in the University calendar	:	**PhD**
Faculty	:	**Science**
School	:	**Mathematics and Statistics**
Thesis Title	:	**Characterising Internal Tides in a Region of Dynamic Circulation: The East Australian Current at 27ºS**

Internal tides can generate ocean mixing, surface convergences and near-bottom currents, so their predictability is of interest. Internal tides can become temporally incoherent when they interact with topographic features or mesoscale ocean dynamics such as eddies and boundary currents, making prediction challenging. Using in situ observations of temperature, salinity and velocities from an array of deep ocean moorings, this study characterises the strength and variability of the internal tides, in both time and space, off eastern Australia (~ 27°S) during 2012-2013. The data are unique as the mooring array spans the East Australian Current (EAC), a dynamic and eddy-rich Western Boundary Current.

The internal tide energy in the EAC is, generally, greater in the diurnal frequency band than the semidiurnal band (2.73 kW m^{-1} and 0.46 kW m^{-1}, respectively). Internal tide variability is compared to local barotropic tidal forcing, stratification and eddy kinetic energy to determine the influence of and interaction with mesoscale EAC circulation. The results reveal that the diurnal internal tide is locally generated above the continental slope and the strength is modulated by the passing of cyclonic fronts and eddies that alter the local stratification and velocity field. Peaks in semidiurnal internal tide energy are sporadic and may result from a combination of remote and local generation.

We show for the first time that cyclonic frontal eddies along the inshore edge of the Western Boundary Current enhance the near bottom stratification above the continental slope and modulate the diurnal internal tide at the study area. The intensification of the internal tides modulates the vertical displacement of the water column (as observed in temperature and vertical velocity).

A case study of a mesoscale cyclonic eddy passing through the study site reveals that the eddy acts as a catalyst triggering interaction (energy transfer) between the barotropic tide and the internal tide. We show that the response manifests horizontally (increasing horizontal velocities), rather than vertically (vertical temperature and velocities remain stable) during the passage of the eddy.

The results provide insight into the origin and variability of the internal tide off eastern Australia and the interaction with the western boundary current and the passage of cyclonic fronts. Studying the characteristics of internal tides and their interaction with mesoscale ocean circulation helps us quantify their variability and improve their predictability particularly in dynamic regions, which is non-trivial in contrast to the deterministic barotropic tides that generate them.

FOR OFFICE USE ONLY Date of completion of requirements for Award:

Characterising Internal Tides in a Region of Dynamic Circulation: The East Australian Current at 27°S

Eduardo Vitarelli de Queiroz

A thesis in fulfilment of the requirements for the degree of

Doctor of Philosophy

School of Mathematics and Statistics

Faculty of Science

August 2021

ORIGINALITY STATEMENT

‘I hereby declare that this submission is my own work and to the best of my knowledge it contains no materials previously published or written by another person, or substantial proportions of material which have been accepted for the award of any other degree or diploma at UNSW or any other educational institution, except where due acknowledgement is made in the thesis. Any contribution made to the research by others, with whom I have worked at UNSW or elsewhere, is explicitly acknowledged in the thesis. I also declare that the intellectual content of this thesis is the product of my own work, except to the extent that assistance from others in the project's design and conception or in style, presentation and linguistic expression is acknowledged.’

Signed ……

Date 25/08/2021

Signed ……..

Date ……08/02/2022……..

Signed ……..

Date ……08/02/2022……..

INCLUSION OF PUBLICATIONS STATEMENT

UNSW is supportive of candidates publishing their research results during their candidature as detailed in the UNSW Thesis Examination Procedure.

Publications can be used in their thesis in lieu of a Chapter if:

- The student contributed greater than 50% of the content in the publication and is the "primary author", ie. the student was responsible primarily for the planning, execution and preparation of the work for publication
- The student has approval to include the publication in their thesis in lieu of a Chapter from their supervisor and Postgraduate Coordinator.
- The publication is not subject to any obligations or contractual agreements with a third party that would constrain its inclusion in the thesis

Please indicate whether this thesis contains published material or not.

☒ *This thesis contains no publications, either published or submitted for publication (if this box is checked, you may delete all the material on page 2)*

☐ *Some of the work described in this thesis has been published and it has been documented in the relevant Chapters with acknowledgement (if this box is checked, you may delete all the material on page 2)*

☐ *This thesis has publications (either published or submitted for publication) incorporated into it in lieu of a chapter and the details are presented below*

CANDIDATE'S DECLARATION

I declare that:

- I have complied with the Thesis Examination Procedure
- where I have used a publication in lieu of a Chapter, the listed publication(s) below meet(s) the requirements to be included in the thesis.

Name	**Signature**	**Date (dd/mm/yyyy)**
Eduardo Vitarelli de Queiroz		**25/08/2021**

Table of Contents

Acknowledgements

First, I would like to express my sincere gratitude to my supervisors Prof. Moninya Roughan, Colette Kerry and Shane Keating for the continuous support of my PhD. It has been an honour to work under your supervision and I have been learning a lot during this journey. Each meeting, comment and suggestion were very constructive and welcome. I am especially grateful to Moninya for the opportunity to work on this research, for the patience, motivation, and the great support on my PhD, also allowing me to participate in conferences, workshops and two expeditions aboard the RV Investigator.

My sincere thanks to the Coastal and Regional Oceanography Team, for their insightful comments and encouragement.

Mooring data were sourced from the Integrated Marine Observing System (IMOS) - IMOS is a National Collaborative Research Infrastructure Strategy (NCRIS), supported by the Australian Government. It is operated by a consortium of institutions as an unincorporated joint venture, with the University of Tasmania as Lead Agent. I acknowledge the significant contribution of B. Sloyan and the IMOS Deep water mooring team in the data collection.

After I started working on the mooring data from 2012-2013, I wanted to know more about the data collection, so I sought out an opportunity to participate in 2 cruises above the RV Investigator, including the mooring re-deployment in May September 2017. I acknowledge the coordinates of the cruises B. Sloyan and Iain Suthers.

I also acknowledge the Tuition Fee Scholarship to Eduardo Vitarelli de Queiroz funded by UNSW Sydney.

Heartfelt thanks to my second family, Raj, Mel and Aayan, and soccer team, Hamlet, Matt Miguel, Mathew, Max, Helen, Victor and Bernard for all support in my everyday life and for all the fun we have had in the last years. Thanks to Aline S. Martinez for all your support.

Last but not the least, I would like to thank my parents, Augusto Cesar de Queiroz and Valeria Maria Vitarelli de Queiroz, for supporting me spiritually throughout writing this thesis. Without their precious support, it would be much more difficult to conduct this research.

Abbreviations & Symbols

EAC: East Australian Current

EKE: Eddy kinetic energy

SST: Sea surface temperature

SSHa: Sea Surface Height anomaly

N^2: Buoyancy frequency squared

SD: Spectral density

K_1, O_1, M_2 and S_2: Harmonics constituents

f: Inertial frequency

SEQ200, SEQ400, EAC1, EAC2, EAC3, EAC4 and EAC5: Moorings

QC: Quality control

u_{qc}, v_{qc}, w_{qc}: QC'd Velocity

u_{dt}, v_{dt}, w_{dt}: Detided velocity current

U_d, V_d, W_d: Diurnal velocity component

U_{bt}, V_{bt}: Barotropic tide velocity component

U_{sd}, V_{sd}, W_{sd}: Semidiurnal velocity component

T_{qc}: Temperature

T_d: Diurnal temperature component

T_{sd}: Semidiurnal temperature component

EAC-ROMS: Model output

CP: Coherent Portion

T: Period

H: Surface elevation

u_{bt}: Barotropic velocity

ρ: Density

g: Gravity

t: Time

z: Depth

θ: Tidal period

Ø: Phase

u'_{θ}: Velocity perturbations

p'_{θ}: Pressure perturbations

F_{bc}: Baroclinic Flux

C: Conversion of the barotropic energy into baroclinic energy

Ɛ: Criticality

h: Topographic slope

s: Internal wave slope

τ: Wind stress

U_{10}: Wind speed at 10 m above the surface

ρ_{air}: Air density

C_D: Dimensionless drag coefficient

k: Horizontal wavenumber

ω: Frequency

CEs: Cyclonic eddies

List of Figures

Figure 28: Time series of the coherent portion and the spectral density ($^oC^2$/(1/day)) of the semidiurnal frequency using temperature anomaly **a)** near the surface (90 m) and **c)** near-bottom (364 m) above the continental slope (mooring SEQ400). Correlation coefficients between the coherent portion and the spectral density of the diurnal frequency and trend lines **b)** near the surface and **d)** near-bottom.

Figure 29: Barotropic tide height (in m, black), at SEQ400 location, estimated using TPXO at the diurnal and semidiurnal frequencies. Time series of temperature anomaly at 364 m depth (at SEQ400, grey) and the coherent portion (as a percentage) calculated using harmonics **a)** K_1 and O_1; **b)** M_2 and S_2 of the temperature anomaly time series (364 m). **c)** Zoom between 01 February 2013 and 01 May 2013 using harmonics M_2 and S_2.

Figure 30: Barotropic (dashed line) and mean and standard deviation baroclinic (squares) phases of the tide constituents K_1 (blue), O_1 (green), M_2 (red) and S_2 (yellow) at SEQ200 (184 m), SEQ400 (364 m), EAC1 (337 m), EAC2 (407 m), EAC3 (399 m), EAC4 (373 m) and EAC5 (312 m) respectively.

Figure 31: Baroclinic sea surface amplitude induced by internal tides. Four harmonics are analysed **a)** K_1, **b)** O_1, **c)** M_2 and **d)** S_2. The dashed line delineates the study area. The data is from an altimetry product (HRET) provided by Zaron (2019).

Figure 32: Spatial map showing the time-mean criticality in the region for the **a)** diurnal and **b)** semidiurnal tidal band. The contour lines show the 100, 200, 400, 2000 m isobaths. This was calculated using model output, for the same period of the observed data, from EAC-ROMS model output of the region (Kerry et al. 2016).

Figure 33: Time series of the wind stress (N m^{-2}) and the spectral density ($^oC^2$/(1/day)) of the diurnal frequency using temperature anomaly **a)** near the surface (90 m) and **c)** near-bottom (364 m) of the continental slope (mooring SEQ400). Correlation coefficients between the wind stress and the spectral density of the diurnal frequency (between 1st April 2012 and 1st June 2013) and trend lines **b)** near the surface and **d)** near-bottom.

Figure 34: Monthly rotary velocity spectrum at mooring SEQ400 (364 m). Blue and red represent clockwise and counter-clockwise motions, respectively. The harmonic constituents, K_1 and M_2, and near-inertial frequency (f) are plotted with a grey dashed line.

Figure 35: a) Time series of diurnal spectral density (SD) of temperature between 01 May 2012 and 01 June 2013, at the SEQ400 mooring at 364 m depth. **b)** Buoyancy frequency squared

(N^2), between 270 and 364 m depth at the mooring SEQ400. The arrows (S1, S2, S3 and S4) indicate the peaks in stratification (23/07/2012, 06/02/2013, 07/03/2013 and 14/04/2013) that precede intensification of the internal tide. Correlation between the buoyancy frequency squared and SD during the period between **c)** 01/07/2012 and 01/10/2012 green dashed box in b; **d)** 01/02/2013 and 18/05/2013 orange dashed box in b, and **e)** 21/02/2013 and 21/03/2013 (black dashed box in b). The red line is the trend line.

Figure 36: Diurnal barotropic tide height (in m, black) at SEQ400 estimated using TPXO and time series of temperature anomaly (diurnal frequency) at 364 m depth (at SEQ400, grey). The arrows indicate the dates of the passage of the frontal eddies identified using SSTs (Figure 37). The black arrows are the dates S1-S4 showed in Figure 35.

Figure 37: Sea surface temperature (^{o} C) of the 12 frontal eddies observed using satellite data for the dates **a)** 25/04/2012, **b)** 02/07/2012 (explored in Chapter 5), **c)** 27/07/2012, **d)** 14/08/2012, **e)** 17/10,2012, **f)** 01/11/2012, **g)** 14/11,2012, **h)** 14/12/2012, **i)** 06/02/2013, **j)** 07/03/2013, **k)** 17/04/2013 and **l)** 02/06/2013.

Figure 38: Sea surface density (colour, kg/m^3) and sea surface height (0.33, 0.34, 0.35 and 0.48 m contours) using the model output for **a)** scenario S1, 23/07/2012, **b)** scenario S2, 06/02/2013, **c)** scenario S3, 07/03/2013 and **d)** scenario S4, 14/04/2013 (indicated in Figure 35b). Note the colour scales are different for each event and the densities have 1000 subtracted from them for better visualisation. Mooring locations are shown by white geometric shapes, as shown in Chapter 2, Figure 4.

Figure 39: a) Sea surface temperature, **b)** sea surface salinity on 07/03/2013 (Scenario S3 in Figure 35b, Figure 38c) from the model output. The contour lines are 0.33, 0.34, 0.35 and 0.48 m. Mooring locations are shown by white geometric shapes, as shown in Chapter 2, Figure 4.

Figure 40: Cross-sections of one day mean of the components of the velocity, **a)** zonal and **b)** meridional, analysed 7th March 2013 from the EAC-ROMS model output. Mooring locations are shown by dashed lines, as shown in Chapter 2.

Figure 41: Cross-section of one day mean of the **a)** buoyancy frequency squared (N^2), **b)** temperature and **c)** salinity analysed on 7th March 2013 from the EAC-ROMS model output. Mooring locations are shown by dashed lines, as shown in Chapter 2 Figure 5.

Figure 42: Cross-section of the root mean square (RMS) of the diurnal internal tide velocities anomaly in the **a)** zonal (U_d), **b)** meridional (V_d) and **c)** vertical (W_d) directions from the moored data on 7th March 2013 (Scenario S3, Figure 34). The contours are isolines of the N^2 (s^{-2}) calculated from the EAC-ROMS model output (Figure 40a).

Figure 43: a) Diurnal (constituents K_1 and O_1) tide surface height (in black) estimated using TPXO and Sea Surface Height anomaly (in blue) observed from detided altimetry data. Observed data from the mooring SEQ400 is used to calculate the **b)** Eddy kinetic energy (EKE) at 400 m depth and buoyancy frequency (N^2) calculated between 270 and 364 m depth, **c)** Profile of the pressure anomaly, **d)** near-bottom (364 m depth) temperature anomaly and **e)** near-bottom (400 m depth) vertical velocity anomaly at the diurnal frequency.

Figure 44: Snapshots of sea surface temperature (° C) from satellite showing examples of cyclonic eddies passing through the study area from **a)** 14th August 2012, **b)** 25th April 2012 and **c)** 17th October 2012. Note the colour scale changes each snapshot. Mooring locations are shown by white geometric shapes, as shown in Figure 4 (Chapter 2).

Figure 45: Snapshots of the sea surface height (m) of the frontal cyclonic eddies from the model output in the study area (27°S) on **a)** 23/07/2012, **b)** 06/02/2013, **c)** 07/03/2013, **d)** 14/04/2013, **e)** 17/10/2012; and **f)** a frontal cyclonic eddy observed south of the study area (30°S) on 03/02/2013 that was analysed by Schaeffer et al. (2017). The contour lines are 0.33, 0.34, 0.35 and 0.48 m.

Figure 46: Satellite images of sea surface temperature (SST) showing the development and advection of the cyclonic eddy between 14th June and 10th July 2012 (**a**-**e**). The dashed contour lines are negative sea surface height anomaly (SSHa) and the continuous contour lines are positive SSHa. Mooring locations are shown by white geometric shapes, as shown in Figure 4.

Figure 47: Time series of the eddy kinetic energy calculated from the detided velocity observed at the moorings SEQ 200, SEQ400, EAC1, EAC2, EAC3, EAC4 and EAC5 (**a**-**g**) as shown in Figure 5. The detided velocity data (EAC1) is shown in Figure 51. Note the different vertical scales on the panels as the moorings get deeper. The dashed line represents the period between 14th June and 10th July 2012 that the eddy is observed in the study area (Figure.46)

Figure 48: Sea surface temperature (SST) showing the cyclonic eddy in the study area surrounded by the poleward flowing EAC on 2nd July 2012. The arrows indicate the geostrophic

velocities. Mooring locations are shown by white geometric shapes, as shown in Figure 4. The contours are 200m and 1000m isobath.

Figure 49: Cross-sections of one day mean of the components of the velocity from the ROMS model, **a)** zonal and **b)** meridional, analysed on 2nd July 2012. The dotted lines show the core of the eddy (v ~ 0). Mooring locations are indicated by dashed lines, as shown in Chapter 2 Figure 5.

Figure 50: Cross-section of one day mean of the **a)** buoyancy frequency squared (N^2), **b)** temperature and **c)** salinity analysed on 2nd July 2012 at latitude 27°S. The data are from the EAC-ROMS model and the mooring locations are shown by dashed lines, as shown in Chapter 2 Figure 5.

Figure 51: Wavenumber spectra of the barotropic tide from a cross-section at 27°S calculated using sea surface height from the global tide model TPXO (red line, barotropic tide) and wavenumber spectra calculated using SSH from the EAC-ROMS model (blue line, eddy field) during the time that the cyclonic eddy passed through the domain (14th June and 10th July 2012). The black horizontal bands show the range of the mesoscales (1/250 and 1/75 cycles per km) and sub-mesoscales (1/45 and 1/20 cycles per km) and highlight that the barotropic tide only has energy at wavenumber scales smaller than 1/50 cycles per km (< 0.02 cycles per km).

Figure 52: Time series of the velocity components, **a)** zonal (U_{bt}) and meridional (V_{bt}), of the diurnal barotropic tide calculated using TPXO model (harmonics K_1 and O_1). Detided current velocities components, **b)** zonal (u_{dt}) and **c)** meridional (v_{dt}) and velocity components of the diurnal internal tide, **d)** zonal (U_d) and **e)** meridional (V_d), observed at the mooring EAC1 (over the 1000 m isobath, EAC1). The dashed line represents the period between 5th June and 10th July 2012 that the velocity of the barotropic tide is proportional to the velocity of the current.

Figure 53: Time series (5 months) of the ratio of the velocities components **a)** zonal and **b)** meridional ($\frac{u_{dt}}{U_{bt}}; \frac{v_{dt}}{V_{bt}}$) between the detided current velocities (u_{dt} and v_{dt} Figure 52b,c) and the barotropic tide velocities (U_{bt} and V_{bt}, Figure 51a). The dashed line represents the period between 5th June and 10th July 2012 when the proportion through the water column is close to one (in red) for both, zonal and meridional components.

Figure 54: Time series between 24th May and 24th July 2012 of **a)** the magnitude of the horizontal velocity of the diurnal barotropic tide (from TPXO model), **b)** subtidal eddy kinetic

energy (EKE) from the low pass filtered observed velocities (mooring EAC1) and **c)** magnitude of the horizontal velocity of the diurnal internal tide observed from the mooring EAC1.

Figure 55: Time series of the magnitude of the horizontal velocity (speed) of the velocity filtered to the diurnal band. observed from the moorings SEQ200, SEQ400, EAC1, EAC2, EAC3, EAC4 and EAC5 (**a**-**g**).

Figure 56: Time series of temperature in the diurnal tidal band through the water column observed from the mooring EAC1 over the 1000m isobath. The dashed line represents the period between 5th June and 10th July 2012.

Figure 57: Cross-sections of the RMS of the velocity of the diurnal internal tide components **a)** meridional (V_d), **b)** zonal (U_d), and **c)** vertical (W_d), using velocities from the mooring array on 2nd July. The location of the moorings is in order from left to right: SEQ200, SEQ400, EAC1, EAC2, EAC3, EAC4 and EAC5 as shown in Figure 5. The dashed lines are stratification (N^2 (S^{-2})) isolines calculated from the EAC-ROMS model output.

Figure 58: Time series of the observed wind stress between 1st May 2012 and 1st June 2013 collected at 10 m above the sea level at coordinates 27.53^{o}S 153.33^{o}E. The dashed line represents the period between 5th June and 10th July 2012 when the eddy is detected in the study area.

Figure 59: Rotary velocity spectrum at mooring SEQ400 (364 m) calculated during the passage of the eddy, for the period between 14th June and 10th July 2012. Blue and red represent clockwise and counter-clockwise motions, respectively. The harmonic constituents, K_1 and M_2, and near-inertial frequency (f) are plotted with a grey dashed line.

List of Tables

Chapter 1: Introduction

1.1 Background and Motivation

Waves in the ocean occur when fluid, dislocated from equilibrium, is returned to its original position by restoring forces. A familiar example is surface gravity waves generated by a pebble tossed in a pond: in that case, the initial perturbation is the pebble, and the restoring force is gravity or buoyancy. Internal waves are gravity waves that oscillate within, rather than on the surface, of a stratified fluid (Stokes 1847). The concept of internal waves was registered by Benjamin Franklin in a letter in 1762 as he was crossing the Atlantic by ship. As the ship rolled in the waves, he was watching a swinging lamp with a layer of water and a layer of oil. He noticed that there were very large waves at the internal interface between the two layers, but none at the surface (Gill 1982). The amplitude and period of these internal waves in the ocean are both highly variable; wave heights can vary from millimetres to more than 100 m (Alford et al. 2016), and time scales range from a few minutes to a day (Munk 1950).

Buoyancy and the Coriolis force act as the main restoring forces of internal waves in the ocean (Gerkema and Zimmerman 2008; Vallis 2017). The buoyancy frequency varies according to stratification, which in turn is caused by the vertical density gradient through the water column (Garret and Munk 1979; Maze 1987). As variations in density throughout the water column are determined by temperature, salinity, and pressure, they are often highly variable on a local scale. The Coriolis force, due to the Earth's diurnal rotation, deflects water masses that are moving in the ocean to the left of the direction of travel in the Southern hemisphere and the right in the Northern hemisphere. This deflection effect is not the same at all latitudes: it is greater near the poles and tends to zero close to the equator (Gill 1982; Alford et al. 2016). In the absence of other forces, the Coriolis effect causes fluid to travel in circular trajectories, known as inertial oscillations, which are counter-clockwise in the Southern hemisphere and clockwise in the Northern hemisphere. Their angular frequency is given by the Coriolis frequency, which depends on the rotational rate of the Earth and the latitude.

1.1.1 The Spectrum of Waves in the Ocean

A wave spectrum is a quantitative measurement of the energy of waves in the ocean as a function of frequency (period) or wavenumber, the spatial frequency of a wave (Figure 1).

Internal waves in the ocean fill a continuous spectrum bounded by the frequencies defined by buoyancy frequency at the lower bound (dozens of cycles per hour) and the Coriolis frequency at the upper (period between 10^3 and 10^6 seconds), that range from about 4 cycles per hour to frequencies lower than one cycle per day (Garret and Munk 1975). The Coriolis frequency varies with latitude, while the buoyancy frequency, due to the influence of local stratification, varies with location, depth, and time. The internal tide spectrum is characterized by peaks at the upper end with low frequencies (periods of 12 hours and 24 hours).

There are two main mechanisms of generation of these low-frequency internal waves (Figure 2). One is barotropic (surface) tides flowing over steep topography, generating what are termed 'internal tides'. The second mechanism is the disturbance of the ocean mixed layer close to the surface caused principally by wind stress, resulting in waves known as 'near-inertial waves'. There is a third mechanism (Figure 2) that generates internal lee waves over rough topography in deep water, not studied here.

Barotropic tides are related to the gravitational forces between the Earth, the moon, and the sun, which together with the rotation of the Earth, produce diurnal (once daily) and semi-diurnal (twice daily) barotropic tides. Diurnal and semi-diurnal barotropic tides have distinct harmonic constituents, with the main constituents being M_2 (semidiurnal principal lunar), S_2 (semidiurnal principal solar), K_1 (diurnal principal declination tide) and O_1 (diurnal principal declination tide). Each of these has a specific amplitude, frequency, and phase, which together compose the tides observed in the ocean. These tides cycle through different amplitudes according to moon phases, resulting in spring and neap tides.

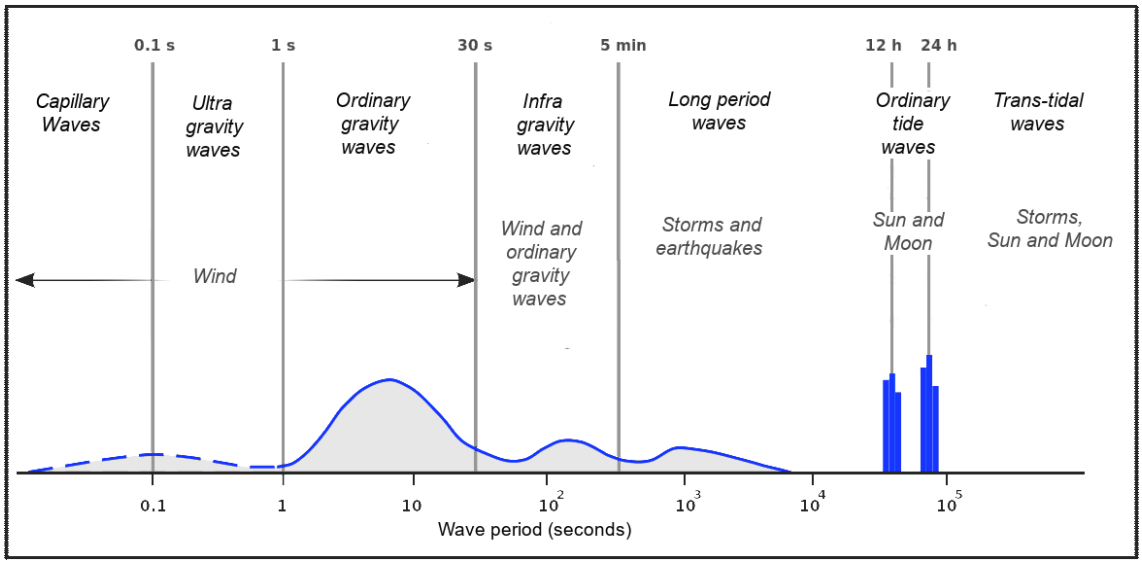

Figure 1: Relative amplitude and classification of ocean waves according to the wave period showing the forces responsible for various portions of the spectrum (Modified from Munk 1950). Internal tides typically occur at the upper end of the spectrum (period of 12 and 24 h).

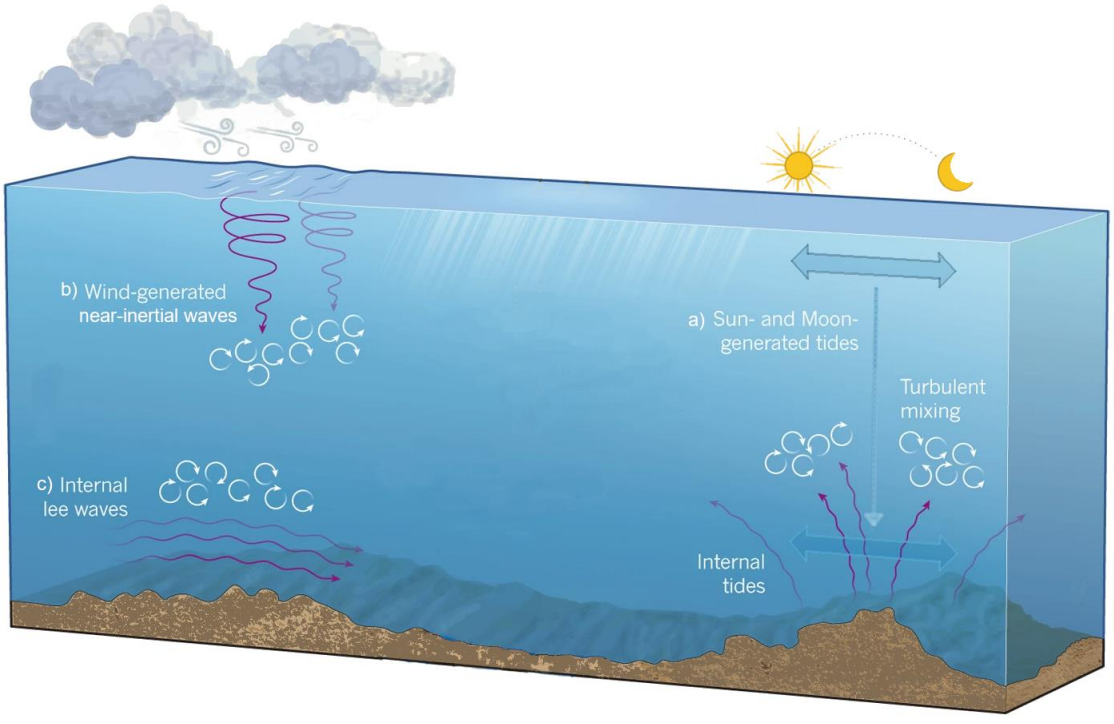

Figure 2: Schematic representation of Internal waves generated by three main mechanisms: **a)** tidal flow over steep topography; **b)** wind stress on the ocean surface; and **c)** quasi-steady flow over rough topography (modified from MacKinnon et al. 2013, Figure 1).

Although barotropic tides and internal tides share similar characteristics, there are significant differences. Both barotropic and internal tides have a similar frequency and phase (Seiwell 1941). Both types propagate horizontally and fill the global ocean. However, the amplitude of internal tides (metres to tens of meters) is generally higher than the barotropic tide (Thorpe 1992). This is due to the smaller difference in densities between the layers of the ocean and the ocean-atmosphere interface in which the barotropic tide is generated. Another important distinction is that internal tides can propagate towards the ocean floor, reaching over 3000 m, and so have implications in mixing the layers of the ocean and generating turbulence in the otherwise quiescent deep ocean (Chuang and Wang 1981; Pingree et al. 1986). Hence internal tides play a very important role in mixing in the global ocean.

The other mechanism of low-frequency wave generation is strong wind stress, which can produce near-inertial waves that are influenced by the Coriolis force. Compared to internal tides, near-inertial waves have smaller vertical displacements. In addition, they are far more intermittent in time and space and the currents are counter-clockwise polarized in the Southern Hemisphere (Fu 1981). Both the amplitude and frequency of near-inertial waves varies with latitude. The amplitude is stronger towards the poles. The frequency of the near-inertial waves can be close to both the semidiurnal and diurnal internal tide frequency. When the near-inertial frequency is equal to the barotropic tidal frequency, it is known as diurnal or semidiurnal critical latitude (Robertson et al. 2017). As with internal tides, near-inertial waves contribute to ocean variability by mixing the ocean layers and generating turbulence throughout the water column, having a global impact (Egbert and Ray 2000; Alford 2003). They also can propagate thousands of kilometres, far from their source regions, before dissipating (Alford 2003; Alford et al. 2016).

1.1.2 The Influence of the Continental Slope on Internal Tides

a) Generation

Barotropic tidal flow over regions of steep topography such as continental slopes and oceanic ridges generates internal waves at tidal frequencies (Baines 1974; Baines 1982; Maze 1987). The generation of the internal tide depends on background stratification, barotropic tide forcing and slope of the bottom topography (Townsend 1965; Baines 1982; Holloway and Merrifield 1999; Griffiths and Grimshaw 2007; Kelly and Nash 2010). The barotropic tidal

current is predominantly horizontal, but over bottom slopes, a vertical current occurs and heaves isopycnal (constant density) surfaces up and down at tidal frequencies (Gerkema and Zimmerman 2008). The magnitude of the internal tides can be estimated by considering the slope at which the internal tides propagate and the topographic slope of the potential generation site (Craig 1987). Even weak barotropic tidal currents can generate an energetic internal tide over steep topography (Holloway and Merrifield 1999).

b) Propagation

Unlike surface waves, whose energy propagates horizontally, the internal tide energy propagates horizontally and vertically (Gerkema and Zimmerman 2008). The difference is due to the different nature of the stratification supporting the waves. Surface waves propagate along with the air-water interface where there is a sharp change in density. Internal waves, on the other hand, propagate in the ocean's interior where density changes are continuously distributed over the vertical, allowing energy to be carried from one depth level to another (Eckart 1961; Maze 1987). The propagation follows a diagonal path into the deep ocean (Prinsenber and Rattray 1975), filling the global oceans (Dushaw et al. 1995, Shriver et al. 2012). The velocity of propagation of internal tide depends on the depth of the bottom and the local density distribution (Munk 1941).

c) Dissipation

Internal waves can change the mixed layer depth spatially and temporally (Garret and Munk 1972; Gregg and Briscoe 1979) and they can contribute to mixing at locations far away from their generation sites (D'Asaro 1978). The effect of the internal waves can also be observed on the bottom of the ocean, generating large sand waves with similar amplitude and wavelengths (Stride and Tucker 1960).

The mixing generated throughout the water column is possible due to the vertical propagation of internal waves. The dissipation of the internal waves results in significant near-bottom mixing (Alford 2010; Martini et al. 2011; Wang et al. 2016) with characteristics of those expected for homogeneous fully turbulent fluids (Caldwell 1976). Shoaling internal tides can also break on the continental slope (Farmer et al. 2011) and propagate upslope independently of the internal tide, mixing the water masses near the bottom (Martini et al. 2013). The

barotropic tide dissipates most of its energy by bottom friction in shallow seas; a significant part, about 30%, is dissipated over ridges in the open ocean where the energy can be transferred to internal tides (Egbert and Ray 2000). The dissipation of the internal tide plays an important role in the mixing of the deep oceans, maintaining the thermohaline circulation and modulating climate (Munk and Wunsch 1998; Niwa and Hibiya 2011).

1.1.3 The Influence of Ocean Circulation on Internal Tide Generation

Mesoscale circulation such as ocean boundary currents can modulate the generation and propagation of internal tides in different ways (Chavanne et al. 2010). They can change the vertical structure of the stratification (Liu et al. 2015; Nan et al. 2011) and background circulation (Colosi and Munk 2006) above the continental slope and thus affect the generation of the internal tides.

In eddy-rich areas, resonant interactions between the mesoscale eddy field and the barotropic tide can facilitate energy transfer to the internal tide (Olbers 1981; Polzin 2010; Dumphy et al. 2017). The effect of the background current on internal tides is stronger in the horizontal rather than vertical motion (Haurwitz 1948; Lelong and Kunze 2013) and the spatially varying phase speed can have a similar rotation as the eddy (Huang et al. 2018). The most efficient generation of the internal tides occurs if the horizontal scale of the barotropic tide current is comparable to that of the eddies (Lelong and Kunze 2013). While this mechanism has often been theorised, it has rarely been observed in the ocean because of the mismatch of the current between the eddies and the barotropic tides in the ocean.

1.1.4 Importance of the Internal Tides

Internal tides are important in many aspects of the ocean. The internal tide can induce vertical mixing resulting in the transfer of heat into deep oceans (Jithin and Francis 2020). The dissipation of internal tide energy contributes to the mixing of the deep oceans that modulates the Earth's climate (Alford 2003). The estimated global tidal energy input into internal tidal waves is 1 TW (Wunsch 2000). While the global energy conversion from geostrophic currents into internal lee waves is 0.2 TW (Nikurashin and Ferrari 2013), about 0.3–1.2 TW of kinetic energy is transferred from the wind to near-inertial motions (Alford 2001). Turbulent dissipation of internal tide energy in the deep oceans may provide about half of the mixing

required to maintain the thermohaline circulation, which modulates the earth's climate (Munk and Wunsch 1998; Niwa and Hibiya 2011). Understanding the generation, propagation and dissipation of internal tides is key to understanding the energy budget of the ocean and developing mixing parameterizations for global climate models (Mazloff et al. 2020). Future changes in stratification may affect the internal tide field globally, with important implications for coastal ecosystems (DeCarlo et al. 2015).

Internal tides can provide nutrients from deep oceans to the shallow water and modulate the zooplankton community (Cooper 1947; Pingree et al. 1986). Internal tides oscillate vertically at the nitricline, which separates the nutrients in the ocean, and when the thermocline rises to near the surface (crest of the internal wave), the increase of nutrients within the euphotic zone can produce phytoplankton blooms (Armstrong and Lafond 1966). They affect coral reefs providing heterotrophic nutrition that makes them more resilient to disturbance (Roder et al. 2010). Internal tides also may play a role in bringing cool water to reefs in a warming ocean, creating "thermal refugia" (Storlazzi et al. 2020).

1.1.5 Internal Tides off Eastern Australia

There have been a handful of investigations into internal tides off eastern Australia. Using field observations, Griffin et al. (1987) identified three main forcing mechanisms associated with the internal tides off north-eastern Australia (Latitude 25^{o}S): the local wind stress, coastal trapped waves (low frequency) propagating from south of Fraser Island, and the northward flow of a cyclonic eddy. Further to the south, off Sydney (Latitude 33^{o}S), observed temperatures show that the internal tides also contribute to upwelling onto the continental shelf. The amplitude of the internal tide at the shelf off Sydney is large compared to the barotropic tide (Gibbs and Middleton 1997). The internal tides are generated on the continental slope and their generation and propagation depend on the local stratification. Despite the amplitude of the semidiurnal barotropic tide being higher than diurnal, the diurnal internal tides have larger amplitudes. The authors did not investigate the cause of the stronger diurnal internal tide.

Investigations into internal tides along the east coast of Australia have increased in the recent year mostly focussed on the Tasman continental slope poleward of 40^{o}S. The highly pronounced internal tidal beam originating over the Macquarie Ridge, south of New Zealand, crosses the Tasman sea (Boettger et al. 2015; Johnston and Rudnick 2015) and is reflected at

the Tasman continental slope (Klymak et al. 2016). A modelling study of internal tides near the diurnal critical latitude (between 27°S and 30°S) off eastern Australia, shows that tides become resonant at local seamounts increasing generation and energy transfers to internal tide harmonics (Robertson et al. 2017).

Internal tides off Brisbane, Eastern Australia (27°S), were the focus of a brief study by Alford et al. (2017) who investigated their generation using some of the same observations that will be used in this thesis (described in Chapter 2). The authors suggest that most of the incident semidiurnal internal tide energy is generated remotely (near New Caledonia and the Solomon Islands). However, no details were provided regarding the magnitude of the velocity, temperature, and fluxes of the shoaling semidiurnal internal tides. The diurnal frequencies generated locally were attributed to the near-inertial waves and the generation of the diurnal internal tide above the continental slope were not investigated. In addition, this region spans the dynamic East Australian Current the western boundary current of the south pacific subtropical gyre. In this thesis, I address these knowledge gaps, including the temporal and spatial characteristics, the origin, and the variability of the internal tides above the continental slope off Eastern Australia at Latitude 27^{o}S and the modulation by the mesoscale circulation and EAC eddies.

1.2 Project Summary and Objectives

The relevance of the continental slope for the generation of the internal tide and mixing near the bottom of the ocean is well known. However, analysis of the internal tides near the coast and below the surface is still a challenge resulting from a lack of observational data. Satellite sensors cannot collect data below the surface, and their utility is limited by the coast. Sub-surface data near the bottom of the ocean is limited to sparse in-situ observations.

This research aims to characterise the diurnal and semidiurnal internal tides above the continental slope off eastern Australia at Latitude 27^{o}S using a comprehensive in situ observational dataset. This region is of interest because it is located in a region of dynamic circulation, within the influence of a western boundary current, the East Australian Current. At this latitude, the EAC is considered to be most coherent (Sloyan et al. 2016), and there is also the presence of mesoscale eddies (Ribbe and Brieva 2016; Ismail et al. 2017; Roughan et al. 2017).

Ocean currents and eddies can influence the internal tides in different ways, including their generation, propagation, and dissipation. Understanding the mechanisms of interaction between the internal tide and ocean features, such as eddies, can provide information about dynamic models and predictability. This study investigates the origin of the internal tide (local and remote) and the varying internal tide in a region of energetic mesoscale circulation. Then we investigate mechanisms that modulate the internal tide at the study area. Understanding the influence of the ocean circulation such as the East Australian Current and its eddies on the variability of the internal tide as these interactions is important as it can change the local current and stratification over the continental slope.

To this end, three fundamental research questions are addressed:

i) What are the characteristics and origin of the diurnal and semidiurnal internal tides in a vigorous western boundary current? (Chapter 3)

ii) How do the frontal eddies influence the internal tide over the continental slope? (Chapter 4)

iii) Does the interaction between mesoscale cyclonic eddies and the barotropic tide favour internal tide generation? (Chapter 5)

The data set, used in this research, and the study area are described in Chapter 2. The design of the analysis of the three main topics are described in Chapters 3, 4 and 5 respectively:

Chapter 3) Characteristics and Origin of the Internal Tides off Eastern Australia

We characterise the internal tides using estimates of the baroclinic tide (strength, energy flux and phase) as calculated from a comprehensive observational dataset. We investigate the origin of the internal tide through comparison with ocean conditions such as barotropic spring-neap tide cycle, the coherent portion (stationarity) of the internal tide and criticality of the study area to understand where the internal tide is likely to be generated. We also quantify the mean baroclinic energy flux to understand the propagation and generation characteristics of the internal tide. The results provide the characteristics of the internal tides off Eastern Australia and an insight into the origin for both diurnal and semidiurnal tidal frequencies.

Chapter 4) Modulation of the Diurnal Internal Tide over the Continental Slope

We investigate the main mechanisms that modulate the diurnal internal tide above the continental slope in the study area. To do so, we analyse the variability of the internal tide and compare it to the barotropic tide, vertical structure (stratification) and ocean circulation. We compare the stratification with the internal tide energy and how these change with the

passage of frontal eddies on the inshore edge of the East Australian Current. The results give an insight into the variability of the diurnal internal tides above the continental slope and the mechanism of internal tide generation off Eastern Australia.

Chapter 5) Do barotropic Tide-Eddy Interactions excite the Internal Tides?

We investigate the interaction of a mesoscale cyclonic eddy and the internal tide. Mesoscale eddies can act as a catalyst triggering interaction (energy transfer) between the barotropic tide and the internal tide. The energy transfer is horizontally (increasing horizontal velocities), rather than vertically (vertical temperature and velocities remain stable) during the passage of an eddy. A case study of a mesoscale cyclonic eddy is analysed in this study. We compare the parameters of velocity and wavenumbers between an eddy field and the barotropic tide to investigate if there are conditions for interaction between them, and intensification of the diurnal internal tide. We analysed the response of the internal tide with the passage of the eddy and compare the horizontal (velocity) and the vertical scales (velocity and temperature) of the internal tide with the eddy. Due to the mismatch of the horizontal scales of mesoscale eddies and internal tides this mechanism does not occur often but can play a role in the ocean dynamics.

Chapter 2: Study Site and Data Sets

In this thesis, we make use of a range of comprehensive data sets. These include the first in situ observations from a full depth transport resolving mooring array deployed off Eastern Australia, at ~27°S (Sloyan et al. 2016), designed to measure the core of the East Australian Current (EAC). These data provide insight into the internal tides and ocean dynamics through the water column. We use the output from TPXO, a suite of fully global tide models (Egbert and Erofeeva 2002) that solves sea level elevations and velocities associated with the barotropic tides. Satellite-derived observations of sea surface temperature (SST) and sea surface height anomaly (SSHa) are used to analyse the mesoscale circulation. We also use the output from a high-resolution data assimilating model of the EAC System (Kerry et al. 2016; Kerry et al. 2020) to support the analysis. These datasets and their processing are described below.

2.1 The Study Area

The study area is an approximately 100 km square region, located at ~ 27°S off eastern Australia and is dominated by the East Australian Current (EAC) (Figure 3). In this region, the EAC has been shown to be most coherent, and it is also well studied (Hamon 1965; Bowen et al. 2005; Sloyan et al. 2016). The continental shelf at the study area is about 53 km wide. A steep continental slope is present that extends from about 322 m to 4206 m depth over 41 km. There is also the presence of seamounts offshore more than 4000 m high (Figure 4).

2.1.1 East Australian Current

The circulation dynamics off eastern Australia are highly energetic and variable (Oke et al. 2019). The circulation is dominated by the western boundary current of the South Pacific Subtropical Gyre (Figure 3), the East Australian Current. The EAC transports warmer waters from the Coral Sea poleward into the Tasman Sea (Middleton et al. 1996). The current typically separates from the coast between 31°S and 33°S forming an energetic mesoscale eddy field in the Tasman Sea (Bowen et al. 2005; Ridgway et al. 2008; Cetina-Heredia 2014). The EAC drives much of the variability in the continental shelf circulation off south-eastern Australia (Wood et al. 2016), with eddy shedding having a significant impact on the shelf circulation (Schaeffer et

al. 2014; Ribbat et al. 2020). The EAC intrusions onto the shelf can increase the stratification even during winter (Middleton et al. 1996; Archer et al. 2017).

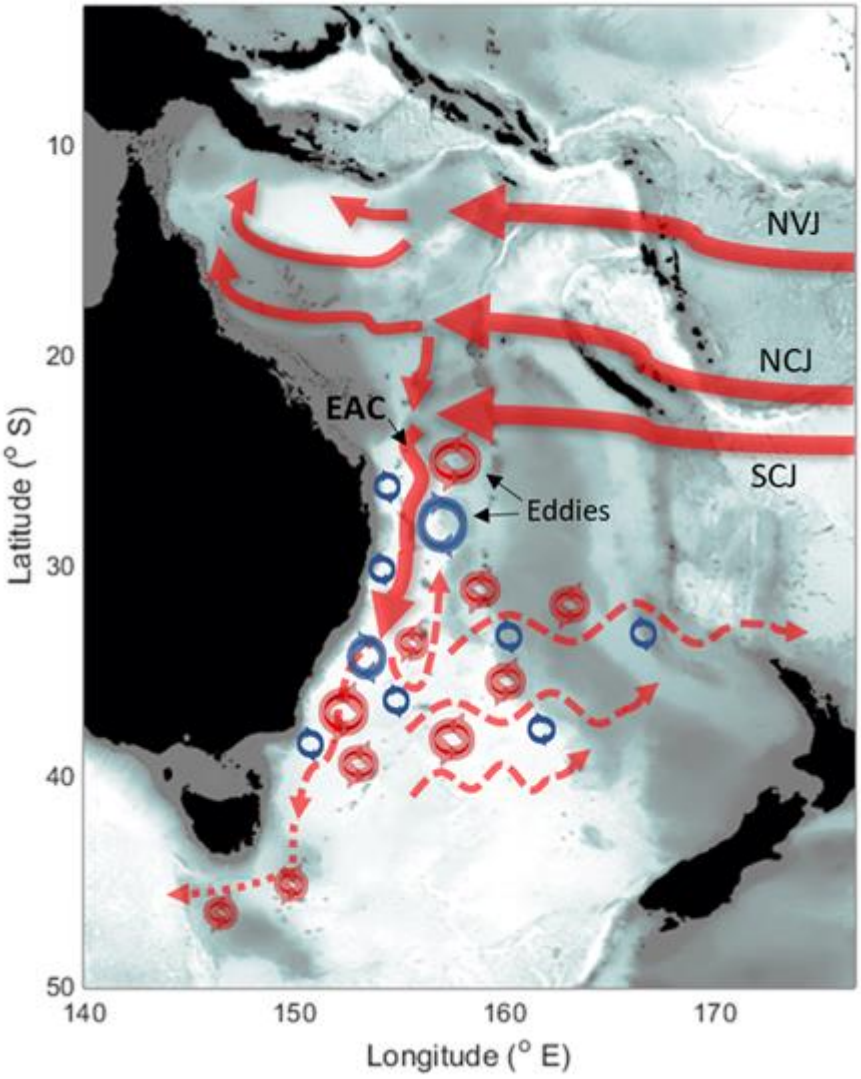

Figure 3: Schematic representation illustrating the circulation of the East Australian Current (EAC) and the eddy field (red, anticyclonic, and blue, cyclonic circles). North Vanuatu (NVT), North Caledonia Jet (NCJ) and South Caledonia Jet (SCJ) are the branches of the South Equatorial Current that compose the South Pacific Gyre (modified from Oke et al. 2019).

The jet of the EAC is most coherent at 27°S (Sloyan et al. 2016). The mean currents and the variance ellipses for the mooring deployment are shown in Figure 3 of Sloyan et al. 2016). However, there are periods where the EAC jet is deflected from the coast by cyclonic eddies (Ribbe and Brieva 2016; Ismail et al. 2017; Roughan et al. 2017). They can occur through the growth of frontal eddies that form, grow and propagate south on the inside edge of the EAC (Schaeffer et al. 2017). Frontal cyclonic eddies are frequent south (downstream) of the study area (at 30°S) where about 40 cyclonic eddies were observed between September 2012 and September 2013 on the inside edge of the EAC (Schaeffer et al. 2017). These frontal eddies are generated by instabilities of the mean flow and have poleward advection. They are short-lived (1–4 weeks) and range from 10 to 60 km in diameter.

The eastern ocean of Australia is complex in terms of ocean dynamics, including an energetic western boundary current, meandering between the continental shelf and offshore (Archer et al. 2017; Archer et al. 2018), and anticyclonic eddies are shed at a frequency of 60-110 days (Bowen et al. 2005; Oke et al. 2019). In addition, westward propagating cyclonic eddies interact with the mean flow of the EAC jet causing deflections and modulation of the flow. The influence of these eddy dynamics on the generation, propagation and dissipation of internal tides is still not well known. The EAC is the ideal natural laboratory with which to examine these dynamic interactions in a WBC region due to the comprehensive in situ data available.

2.2 In-situ Data Sets

2.2.1 The EAC Mooring Array

We use the data from a state-of-the-art mooring array funded by NCRIS and deployed by CSIRO. This time series is the first deployment from what is now an extremely valuable, nearly a decade of observations obtained at the site. A full depth, transport resolving mooring array was deployed off the coast of eastern Australia from April 2012 to August 2013 (Figure 4, Table 1) as part of the Integrated Marine Observing System (IMOS, www.imos.org.au, Sloyan et al. 2016). The array was deployed at ~27°S extending from the continental shelf/slope (moorings SEQ200, SEQ400, EAC1 and EAC2) to more than 190 km offshore in ~ 4800 m of water (moorings EAC3, EAC4 and EAC5). Full details of the deployment locations are provided in Table 1.

The instrumentation on the array consisted of 12 acoustic Doppler current profilers (Teledyne-RD Instruments Longranger 75 kHz, Workhorse Quartermaster 150 kHz and Workhorse Sentinel 300 kHz), 28 point-source velocity meters (Nortek Aquadopp DW), 30 point-source temperature sensors from Star Oddi (Starmon Mini instruments), and 25 point-source temperature salinity, pressure sensors (Seabird SBE37-SMP MicroCAT) distributed across the 7 moorings (Figure 5).

More information on the mooring array can be found in Sloyan et al. (2016). Information on the mooring deployment and recovery voyages (ss2012_v01 and ss2013_v05) can be accessed from the CSIRO Marine and Atmospheric Data Centre (http://www.marine.csiro.au/marlin). For this study, we analyse the time series of temperature, salinity, pressure, and velocities (horizontal and vertical) from all 7 moorings to characterise the internal tides in the region. The temporal resolution of the temperature data is very high, where the sampling intervals are 2 minutes for SEQ200 and SEQ400 and 5 minutes for EAC1-5. Each temperature sensor has an associated pressure sensor. The sampling interval of the velocity data is every 30 minutes at all moorings.

The processing and quality control (QC) of the data is described by Cowley (2015). However, in short, all Seabird CTDs, except new instruments, were calibrated at the CSIRO Marine and Atmospheric Research Calibration Facility before deployment. Seabird, Star Oddi, and some Nortek Aquadop DW instruments were placed in a post-deployment calibration bath to identify temperature offsets. Spikes, pressure drifts and data offsets were examined visually and manually QC'd. The data were processed using Matlab and attributed QC flags including in and out of water times at the start and end of the deployment and timing adjustments. The velocity data QC was conducted based on the output from the RDI ADCP instruments (echo amplitude, correlation magnitude, per cent good, error velocity and velocities) and the quality issues of each instrument were described by Cowley (2015). Here we use the QC'd flagged data provided by Cowley (2015).

Details of the mooring locations (latitude and longitude), the deployment and retrieval dates, bottom depth of each mooring and distance from the coast are shown in Table 1. The moorings are aligned from the shelf, across the continental slope, 32 km from the coast (209 m depth), to the deep abyssal basin 190 km from the coast (4797 m depth). Table 2 shows the brand and the model of each instrument used on the mooring array detailed in Table 1 and summarizes details of the measurements such as accuracy, precision, and resolution of each sensor. The bathymetry is sourced from the Naval Research Laboratory Digital Bathymetry

Data Base 2-minute resolution (NRL DBDB2). The product is a global topography data set on a 2-min by 2-min uniform grid developed for the ocean model (https://www7320.nrlssc.navy.mil/DBDB2_WWW/).

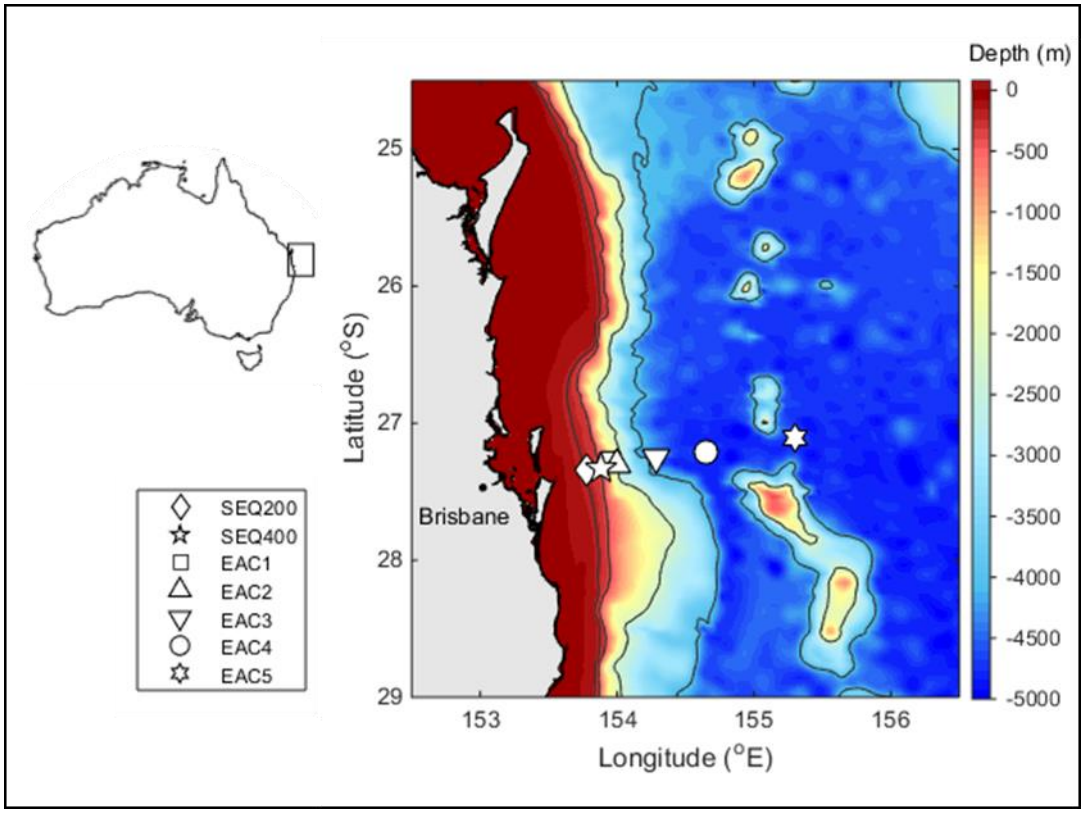

Figure 4: Map showing the location of the study area on the east coast of Australia and the locations of moorings SEQ200, SEQ400, EAC1, EAC2, EAC3, EAC4 and EAC5 off Brisbane (denoted by symbols), eastern Australia. Colour shading shows the bathymetry, and the contours are 200, 400, 2000 and 4000 m isobath.

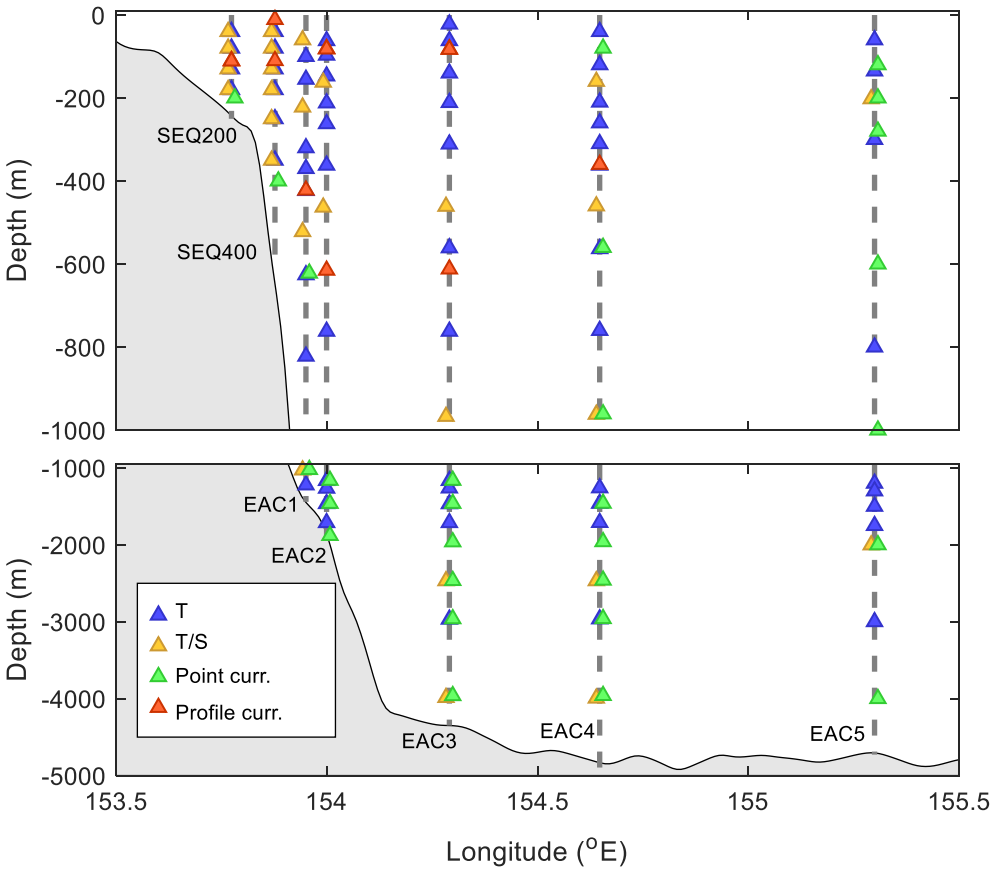

Figure 5: Cross-section across the mooring array showing the nominal depth of the instruments used from each mooring. The data include point-source temperature (T), temperature and salinity (T/S), point-source current, current profiles. Each sensor has a pressure sensor that is used to calculate the depth. For full details on the mooring array, see Sloyan et al. (2016) and Tables 1 and 2.

Table 1: Details of the mooring name (platform code) deployment and retrieval dates, location (latitude and longitude), distance from the coast and water depth of the mooring array (after Sloyan et al. 2016).

Platform code	Start Time	End Time	Latitude S	Longitude E	Distance (km)	Bottom depth (m)
SEQ 200	01/Apr/2012	06/Jun/2013	27°20.4’	153°46.4’	32	209
SEQ 400	01/Apr/2012	06/Jun/2013	27°19.9’	153°52.59’	40	405
EAC M1	21/Apr/2012	23/Aug/2013	27°18.75’	153°58.14’	52	1525
EAC M2	22/Apr/2012	24/Aug/2013	27°18.38’	153°59.52’	55	1940
EAC M3	23/Apr/2012	24/Aug/2013	27°15.1’	154°17.42’	85	4220
EAC M4	25/Apr/2012	25/Aug/2013	27°12.51’	154°38.82’	120	4745
EAC M5	26/Apr/2012	26/Aug/2013	27°6.12’	155°17.95’	190	4797

Table 2: Summary of instrument types, measurements, accuracy, precision, and resolution used to compose the mooring array.

Instrument Brand	Instrument model	Measurement (accuracy, precision or resolution)
Seabird	SBE37 SMP (pumped unit)	Pressure (±0.1% max depth rating), temperature (±0.002°C), conductivity (±0.0003S/m).
Star Oddi	Starmon Mini	Temperature (±0.05°C).
RDI	Long Ranger 75kHz	Pressure (±0.25% full scale), temperature (accuracy not stated, precision ±0.4°C), currents (accuracy ±1% ±5mm/s, resolution 1mm/s).
RDI	RDI Workhorse Quartermaster 150kHz	Pressure (±0.25% full scale), temperature (accuracy not stated, precision ±0.4°C), currents (accuracy ±1% ±5mm/s, resolution 1mm/s).
RDI	RDI Workhorse Sentinal 300kHz	Pressure (±0.25% full scale), temperature (accuracy not stated, precision ±0.4°C), currents (accuracy ±0.5% ±5mm/s, resolution 1mm/s).
Nortek	Aquadop DW	Pressure (0.25%), temperature (±0.1°C), currents (accuracy ±0.5% ±5mm/s).

The time series (QC data) of temperature (T_{qc}), velocity, zonal (u_{qc}) and meridional (v_{qc}), from the array, are presented in Figures 6, 7 and 8 respectively for each depth, calculated from pressure. The vertical spacing of temperature sensors through the water column varies across the mooring array (Figure 5). Each temperature sensor has a pressure sensor that is used to calculate the depth. The moorings near the continental shelf, SEQ200 and SEQ400, have the highest resolution (~ 50 m vertical resolution) due to the shallower water depth; 209 m and 405 m depth respectively (Table 1, Figure 5). The mooring EAC5 is the most offshore and deepest mooring (4797 m depth) and has the lowest vertical resolution with some sensors up to 500 m apart.

Velocity profiles measured by the ADCPs and point source cover a range of depths, as shown in Table 3. The highest resolutions are in the moorings SEQ200 and SEQ400 while the mooring EAC5 has the lowest resolution with no profile source velocities.

The QC data of the velocity measurements (u_{qc} and v_{qc}) are shown in Figures 7 and 8. The velocity has true north orientation. The velocity is presented in cardinal coordinates (N-S and E-W) because it is close to the orientation of the bathymetry and the current at 400 m depth has N-S orientation (Sloyan et al. 2016). There are variations in bathymetry and variation in the flux is important, then we use vectors as a component. Figures 7 and 8 show details of the vertical resolution (over depth) and a good resolution in time with few gaps. The reduction in vertical resolution in velocity below a certain depth, 400m for EAC1, 600m for EAC2 and EAC 3 (Figures 7 and 8) is due to the different vertical resolution in velocity observations from the velocity profiles above that depth and point source measurements below (Table 3). The results of the vertical velocity analysis are corroborated by the temperature data, due to the limitations of the vertical velocity data. The results observed to conclude this thesis are based near the bottom of the water column, where mooring tilt is less of an issue.

Table 3: Details of the vertical resolution and sampling interval of the velocity (profile and point source) measured in each mooring (SEQ200, SEQ400, EAC1, EAC2, EAC3, EAC4 and EAC5).

Mooring	Profile depth range (m)	Sampling interval (minutes)	Point source depth (m)	Sampling interval (minutes)
SEQ200	30 - 190	30	195	30
SEQ400	40 - 290	30	405	30
EAC1	90 - 400	60	625 and 1025	30
EAC2	11 - 680	60	1195, 1476, and 1882	30
EAC3	14 - 960	60	1220, 1492, 1991, 2477, 2962 and 3963	30
EAC4	45 - 450	60	560, 960, 1457, 1957, 2457, 2958 and 3960	30
EAC5	-	60	130, 244, 594, 993, 1993, 2796 and 4009	30

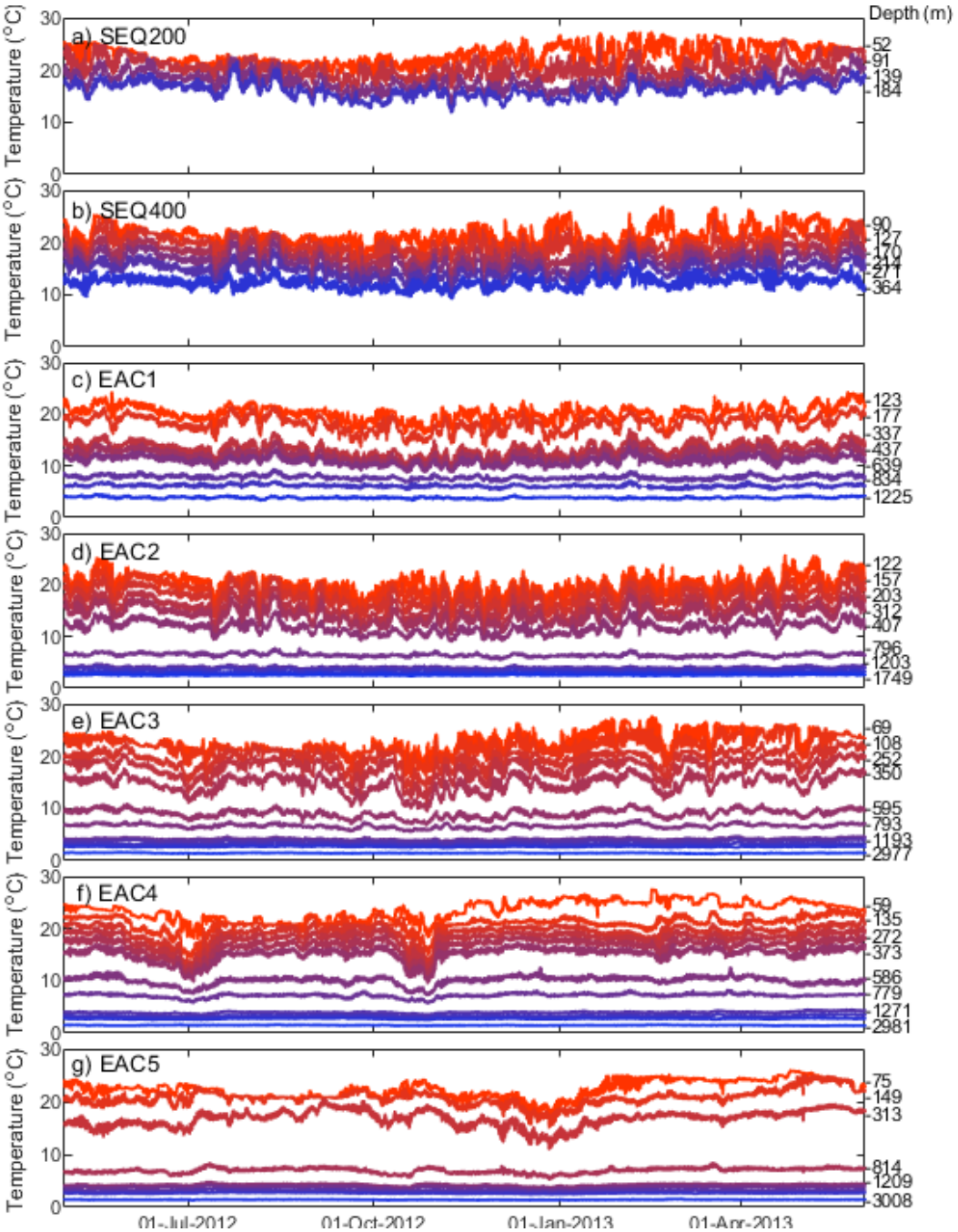

Figure 6: Time series of the temperature data (T_{qc}) at each depth (shown by colour, right axis) measured in the moorings SEQ200, SEQ400, EAC1, EAC2, EAC3, EAC4 and EAC5 (**a**-**g**). The mean depth, calculated for each pressure sensor, is presented in the right y-axis.

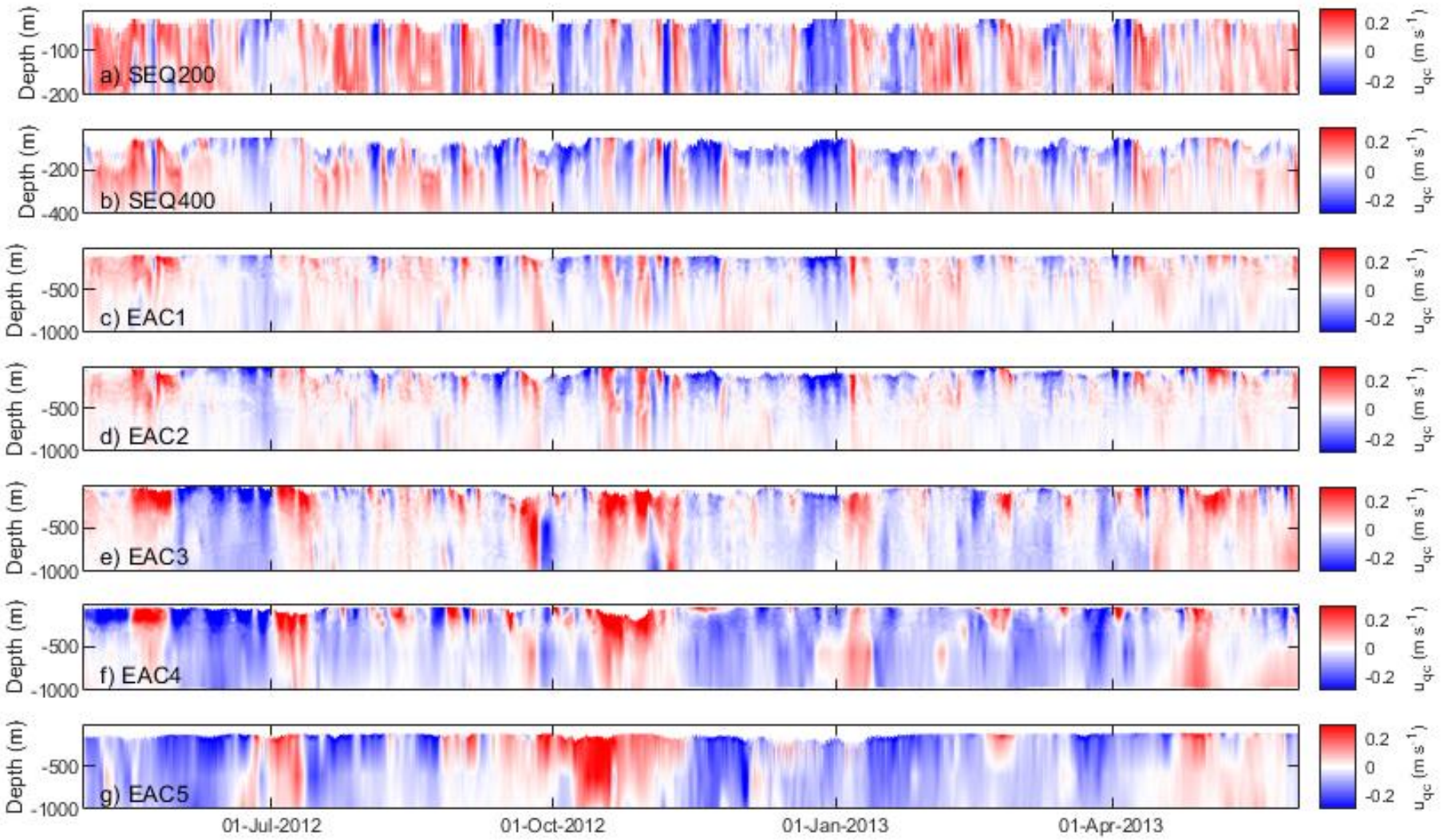

Figure 7: Time series of the quality controlled (QC'd) zonal velocity (u_{qc}) in m s^{-1} (over 1000 m depth) as measured at the moorings SEQ200, SEQ400, EAC1, EAC2, EAC3, EAC4 and EAC5 (**a**-**g**) for 1st May 2012 – 1st June 2013. Note the change in vertical resolution on the depth axis.

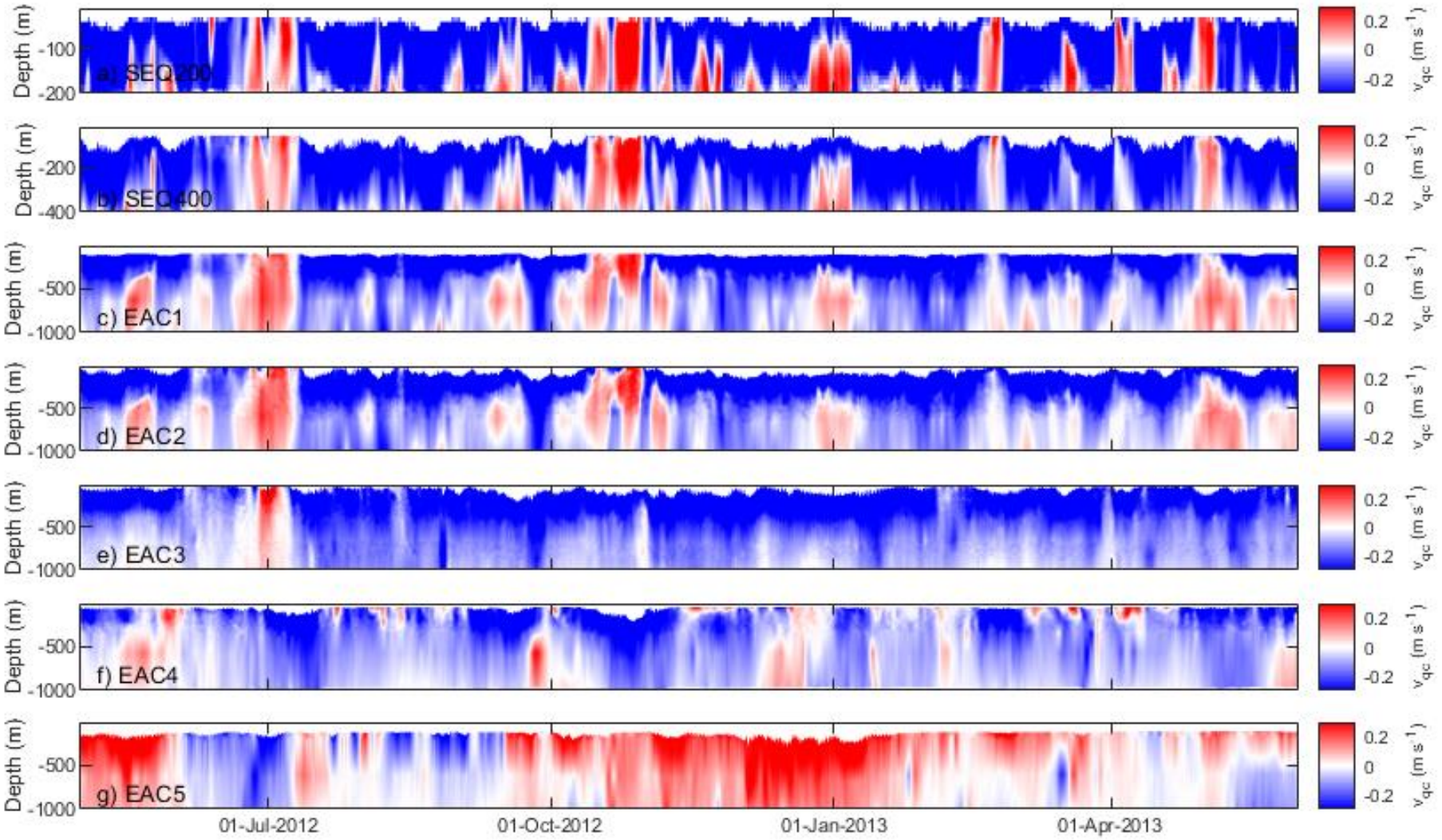

Figure 8: Time series of the quality controlled (QC'd) meridional velocity (v_{qc}) in ms^{-1} (over 1000 m depth) as measured at the moorings SEQ200, SEQ400, EAC1, EAC2, EAC3, EAC4 and EAC5 (**a**-**g**) for 1st May 2012 – 1st June 2013. Note the change in vertical resolution on the depth axis.

2.2.2 Data Averaging and Filtering

The time series of temperature and velocity, zonal (u_{qc}), meridional (v_{qc}) and vertical (w_{qc}), were hourly averaged. To separate the internal tides, the data were band-pass filtered Butterworth filter design using MATLAB version R2018b. To separate the diurnal and semidiurnal tides, bands of 18-30 hours and 9-15 hours were used, respectively.

At the latitude of the study site (27°S), the inertial wave generated by the Coriolis effect is close to the diurnal frequency. The technique used to filter the time series cannot separate the diurnal tide and near-inertial waves because our time series are not long enough to allow adequate frequency resolution.

Table 4 shows the symbols of different processing of the velocity and temperature time series used to analyse the internal tide and the ocean current. The processing methods are quality control, hourly averaging, and filtering.

Table 4: Description of the datasets used, and the filtering applied. Velocities (zonal, u, meridional, v, and vertical, w) and temperature (T) symbols for each processing step: quality controlled, hourly averaged and filtered (tide and detided).

Symbol	Variable	Sampling interval	Filter
u_{qc}, v_{qc}, w_{qc}	Velocity	30 minutes	none
u_{dt}, v_{dt}, w_{dt}	Detided velocity	Hourly	Low passed < 30 hours
U_d, V_d, W_d	Diurnal velocity component	Hourly	Band passed 18-30 hours
U_{sd}, V_{sd}, W_{sd}	Semi diurnal velocity component	Hourly	Band passed 9-15 hours
T_{qc}	Temperature	5 minutes	none
T_d	Diurnal temperature component	Hourly	Band passed 18-30 hours
T_{sd}	Semi diurnal temperature component	Hourly	Band passed 9-15 hours

2.3 Barotropic Tide Data from a Suite of Global Tidal Models

Solutions for the barotropic tide are obtained from the global tidal model TPXO 8.0 (https://www.tpxo.net/global) described by Egbert and Erofeeva (2002). TPXO is a global model of the barotropic tide, which best fit Laplace Tidal Equations (in a least-squares sense) and altimetry data. TPXO 8.0 solutions are obtained at 1/6 degree resolution with higher resolution (up to 1/30 degree) in coastal regions. The TPXO models include complex amplitudes of sea-surface elevations for eight primaries (M_2, S_2, N_2, K_2, K_1, O_1, P_1, Q_1) harmonic constituents.

The barotropic tide height and velocity of the diurnal harmonics (K_1 and O_1) and semidiurnal harmonics (M_2 and S_2) computed from TPXO are used to compare with the internal tide strength. The data of the diurnal and semidiurnal barotropic tide height are shown in figures 9 and 10, respectively.

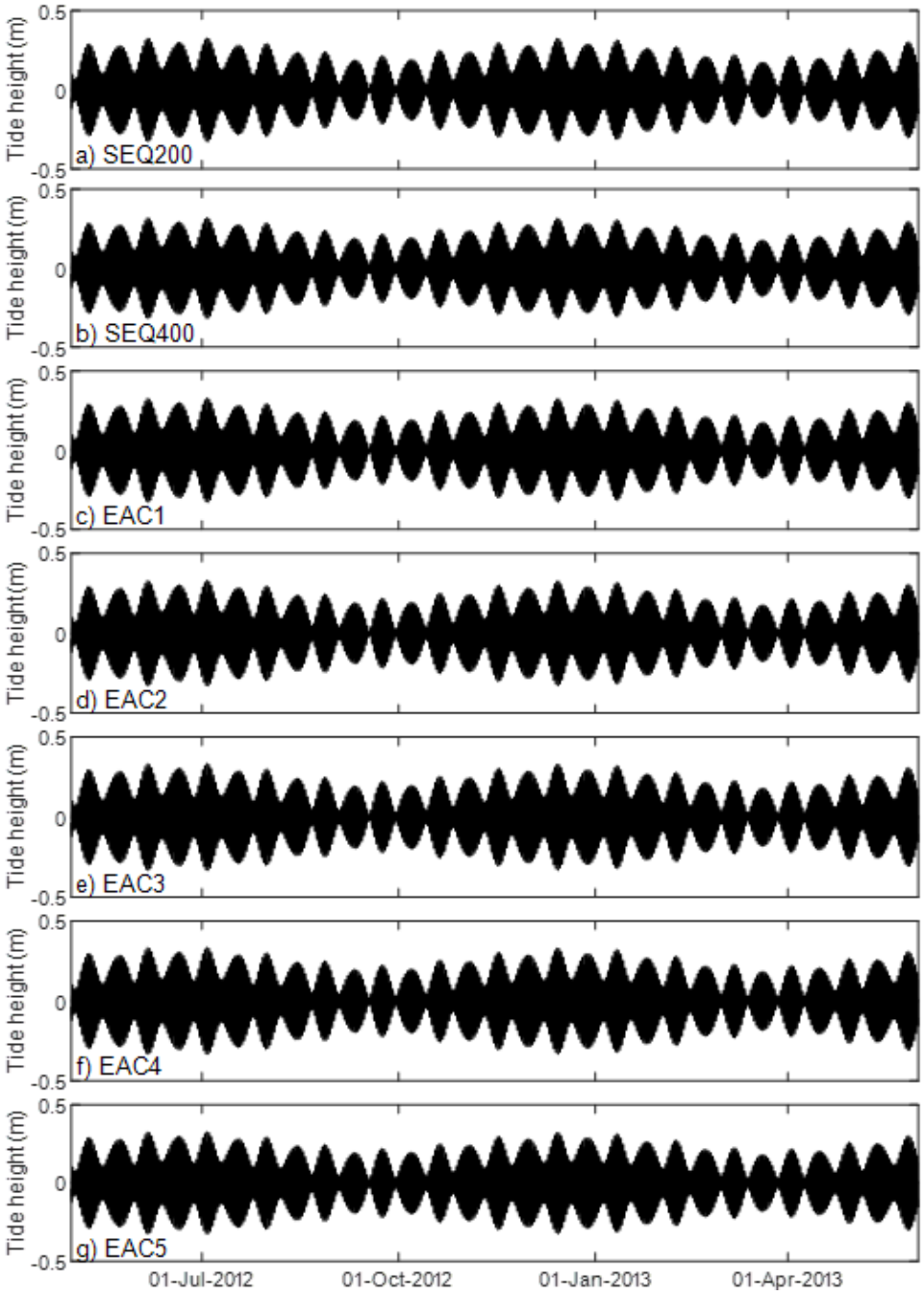

Figure 9: Diurnal tide height, constituents (K_1 and O_1), estimated using the global model (TPXO) for the moorings' locations SEQ200, SEQ400, EAC1, EAC2, EAC3, EAC4 and EAC5 (**a**-**g**) for 1st May 2012 – 1st June 2013.

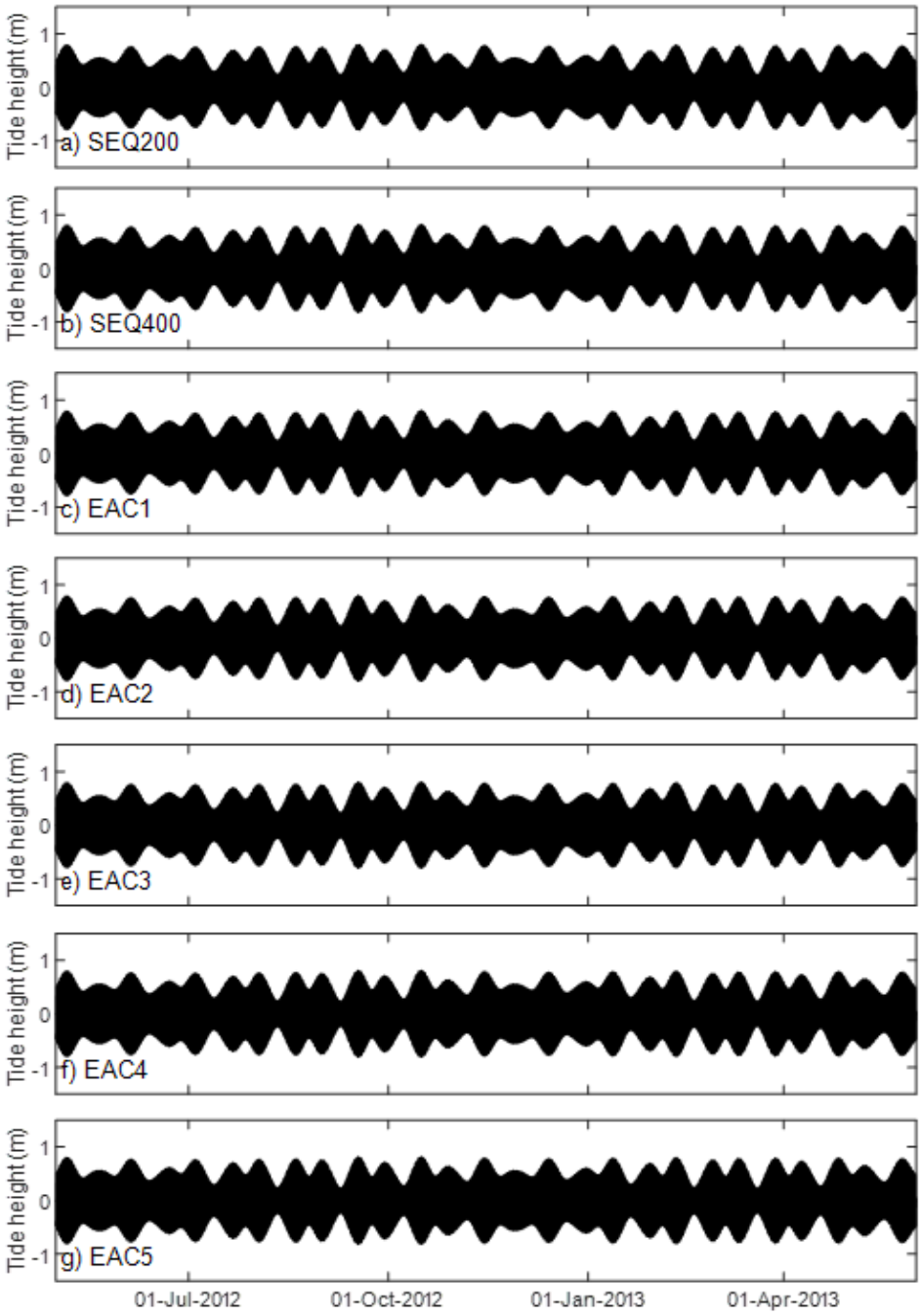

Figure 10: Semidiurnal tide height, constituents (M_2 and S_2), estimated using the global model (TPXO) for the moorings' locations SEQ200, SEQ400, EAC1, EAC2, EAC3, EAC4 and EAC5 (**a**-**g**) for 1st May 2012 – 1st June 2013.

2.4 Remote Sensed Data

Sea Surface Temperature (SST) and Sea Surface Height anomaly (SSHa) data from satellite were sourced from the Integrated Marine Observing System (IMOS). The data was obtained from the website https://portal.aodn.org.au/. The resolution is 0.2° x 0.2° which is about 2km at 27°S over the region 70°E to 170°W, 20°N to 70°S.

The SST data is a multispectral dataset from the NOAA satellite series obtained using Advanced Very High-Resolution Radiometer (AVHRR). The product used in this research is the multi-sensor LS3, 1 day, 3 days and 6 days average of all high-quality data of temperature available. The SST data were calibrated by the Australian Bureau of Meteorology as a contribution to IMOS using drifting buoy depths (20-30 cm) under surface.

Daily data of the geostrophic velocities (zonal and meridional) for the Australian region are estimated by the CSIRO Marine and Atmospheric Research using optimal interpolation of detided, de-meaned inverse-barometer-adjusted altimeter and tide gauge estimates of sea level from the geoid, derived from the Sea Surface Height data (over 18 years of model time) of Ocean Forecasting Australia Model version 3 (OFAM3).

2.5 Numerical Model Output

A high-resolution (2.5-6km) ocean state estimate (reanalysis) was developed for the EAC region for 2 years, between January 2012 and December 2013, using a hydrodynamic numerical model (Kerry et al. 2016; Kerry et al. 2020). The model is configured using the Regional Ocean Modelling System (ROMS 3.4). ROMS is a free-surface and hydrostatic ocean model (Shchepetkin and McWilliams 2005). The boundary forcing is taken from the BlueLink ReANalysis (BRAN3p5). 4-Dimensional Variational data assimilation (Zavala-Garay et al. 2012) is used to assimilate a variety of observational datasets. It uses the dynamics calculated by the numerical model to generate the initial conditions including atmospheric forcing and boundary conditions and better estimates the subsurface conditions. Significantly the model assimilates the data from the EAC and SEQ moorings used here (Section 2.2.1), hence gives the best representation of the ocean state at the location of the moorings, for the time that they were deployed (2012-2013). In this thesis, we will refer to the model output as 'EAC-ROMS'.

In addition to the EAC Transport array data, the model also assimilates hydrographic data from autonomous ocean gliders, surface velocities from High-Frequency coastal radar, temperature data from

expendable bathythermograph (XBT), and Argo floats and satellite-derived observations of sea surface temperature, sea surface height and sea surface salinity obtained through IMOS.

The model has a 2.5 –6km cross-shore resolution and a 5 km alongshore resolution, with 30 vertical s-levels distributed with a higher resolution in the upper 500 m to resolve the wind-driven mesoscale circulation and near the bottom to resolve the bottom boundary layer (Kerry et al. 2020). The model has a mean spatially averaged root mean squared (rms) residuals with the observations of 7.6 cm for sea surface height (SSH) and 0.4 ◦C for sea surface temperature (SST) over the assimilation period. The time-mean rms residual for subsurface temperature measured by Argo floats is a maximum of 0.9 ◦C between water depths of 100 and 300m and smaller throughout the rest of the water column. Velocities at several offshore and continental shelf moorings are well represented in the reanalysis with complex correlations between 0.8 and 1 for all observations in the upper 500 m. Kerry et al. (2016) provided a comparison with independent (non-assimilated) shipboard conductivity temperature depth (CTD) cast observations that shows a marked improvement in the representation of the subsurface ocean in the reanalysis, with the rms residual in potential density reduced to about half of the residual with the free-running model in the upper eddy-influenced part of the water column. This shows that information is successfully propagated from observed variables to unobserved regions as the assimilation system uses the model dynamics to adjust the model state estimate (Kerry et al. (2016).

The efficiency of the model in estimating the transport and eddy kinetic energy in the EAC was quantified (Kerry et al. 2018). The model has been shown to give a good representation of the ocean state and simulation of the mesoscale variability (Kerry et al. 2018; Kerry et al. 2020). The data was obtained from Kerry et al. (2020): https://doi.org/10.1016/j.jmarsys.2019.103286. We use daily output from the model to complement the analysis of the dynamics in the study area (Figure 11). We use modelled estimates of velocity (true north orientation), temperature, salinity and we calculate stratification.

In addition to the model validation presented in Kerry et al. (2016) and Kerry et al. (2018), Figure 12 shows a comparison of the modelled and observed temperature and salinity time series (respectively) at the SEQ400 mooring (assimilated by the model). Figure 13 compares the modelled cross-section of the mean meridional component of the velocity, between May 2012 and June 2013, with the observed in mooring array. It also provides a comparison to Figure 5a from Sloyan et al. (2016). The figures show that the model does a good job of representing the temperature and salinity used to analyse the ocean circulation characteristics and the stratification of the study area. Hence, we are confident that it can be used for the analysis provided in this thesis.

Note that tidal forcing is not included in the EAC-ROMS model and therefore the output is only used to describe the ocean dynamics at the study time, and not in the tidal analysis. Specifically, the model output was used to understand the mechanisms driving the variability of the internal tide such as EAC and its eddies.

2.6 Wind Data

Wind data is collected at 10 m above the sea surface near the study site, about 49 km of distance, at Latitude 27.53°S and Longitude 153.33°E, using Automatic Weather Station at Banana Bank North Beacon (station 040925). The sampling interval is 30 minutes; the data is available from the Bureau of Meteorology at www.bom.gov.au/climate/data/stations.

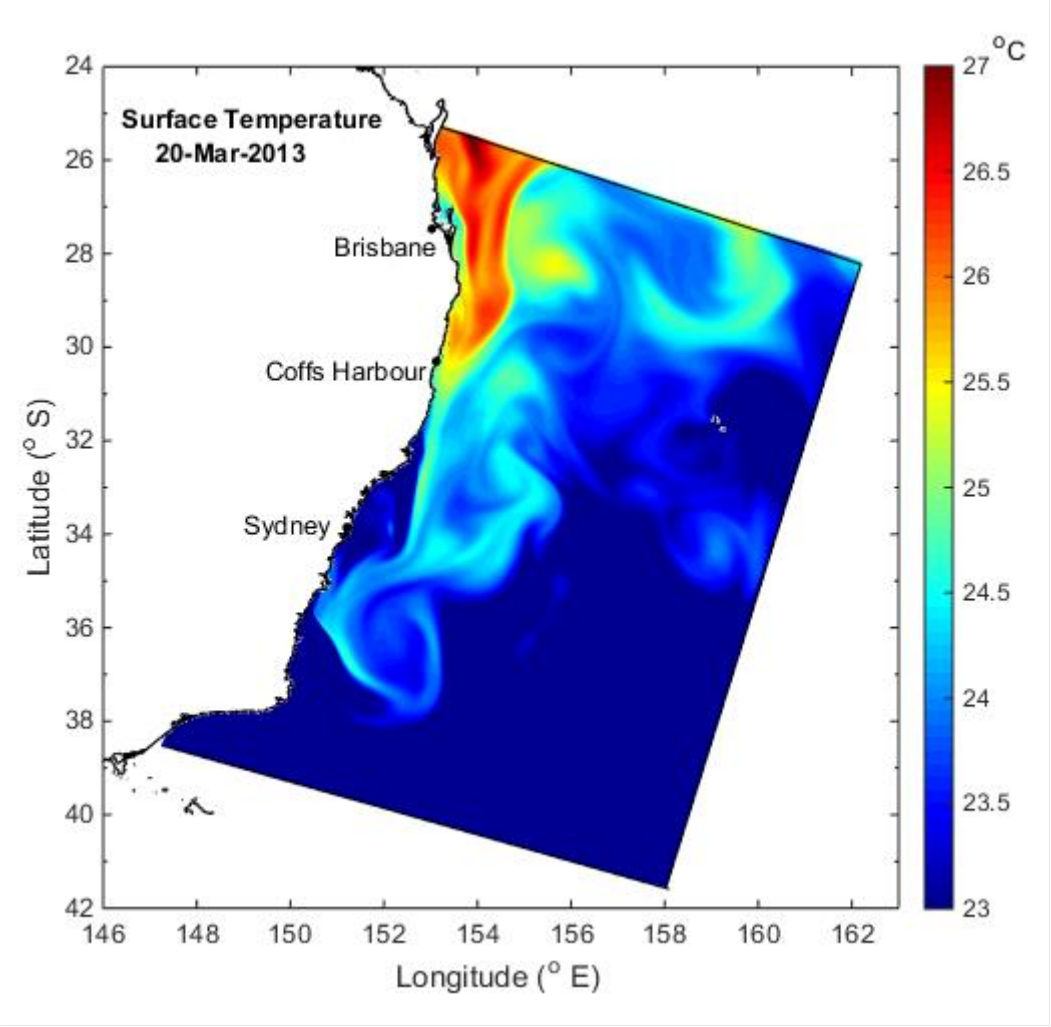

Figure 11: Sea surface temperature (20th March 2013) showing the EAC-ROMS model domain.

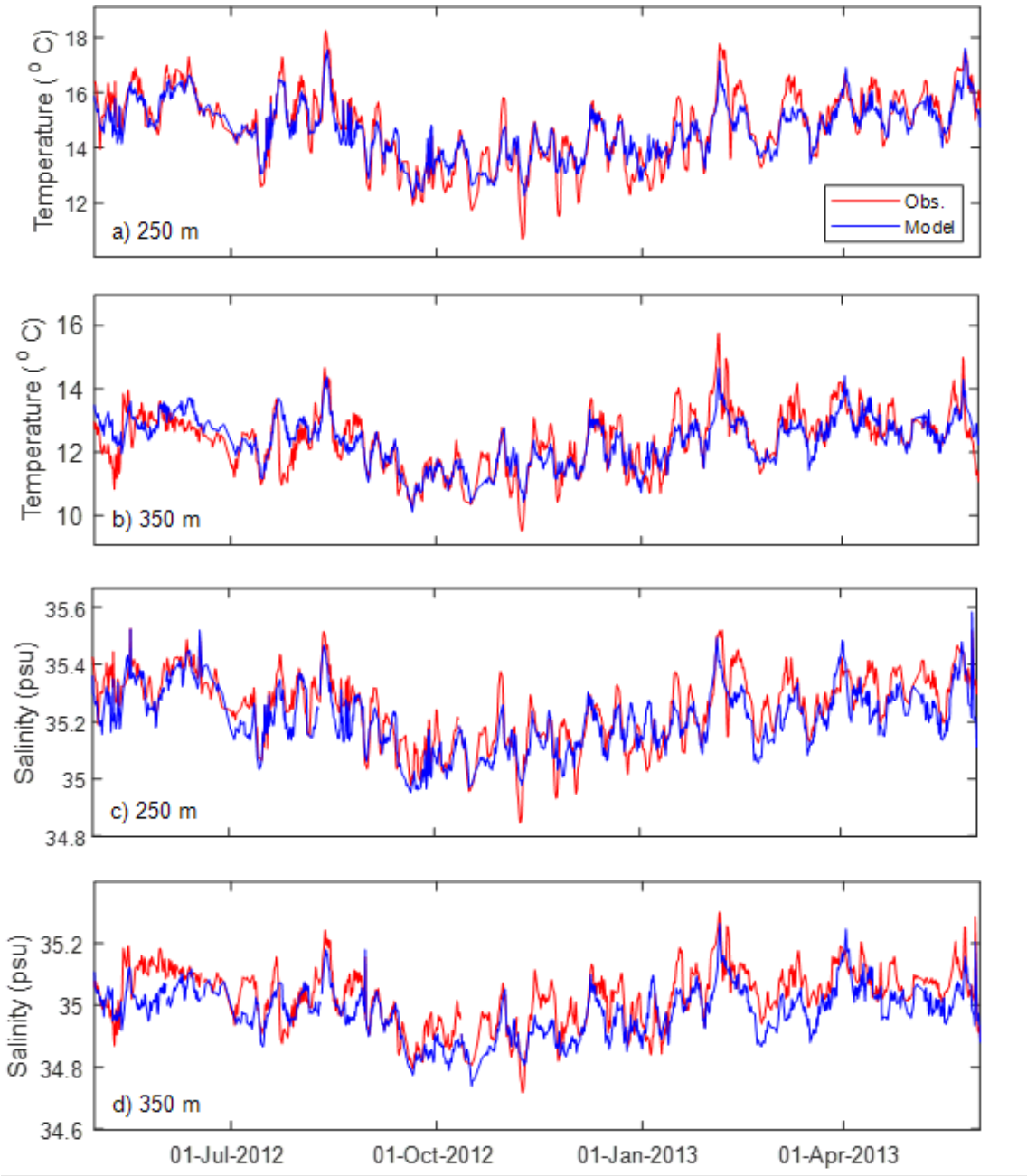

Figure 12: Model validation time series of observed (red) and modelled (blue) temperature at **a)** 250m and **b)** 350m depth, and salinity (in observation space) at **c)** 250m and **d)** 350m depth at the location of the SEQ400 mooring.

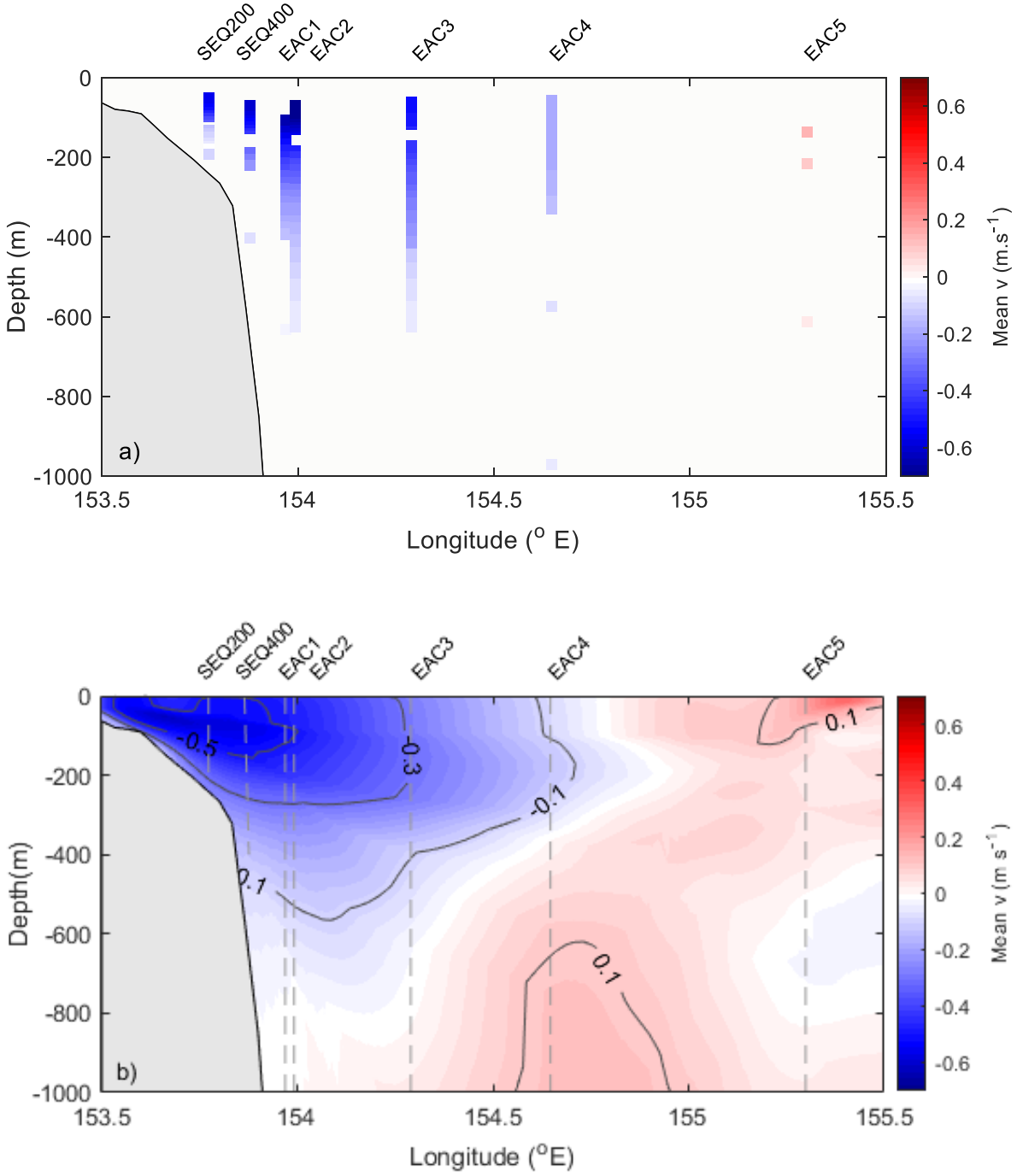

Figure 13: Cross-section of mean meridional velocity, over the period between May 2012 and June 2013, using **a)** observed data from the mooring array SEQ200, SEQ400, EAC1, EAC2, EAC3, EAC4 and EAC5 and **b)** the EAC-ROMS model.

Chapter 3: The Characteristics and Origin of the Internal Tides (Semidiurnal and Diurnal) off Eastern Australia

3.1 Introduction

In this chapter, we characterise the internal tide using data from the mooring array described in Chapter 2 (Section 2.2). We describe the most common characteristics of the internal tide (harmonic components, spectral density, amplitude, and phase of the internal tide) over the period between May 2012 and June 2013. The mean of the current velocity and vertical structure (temperature salinity and buoyancy frequency squared) are analysed for the same time. We compare the characteristics of the internal tides with the barotropic tide and analyse the origin (local or remote) of the internal tides.

In section 3.2 we describe the methods used in this research. In Section 3.3, we analyse the main characteristics of the barotropic tide (amplitude, period, and phase). We calculate the spectral density of the temperature to detect the most significant harmonic constituents of the internal tide in the study area. We analyse the time series of the filtered data at diurnal and semidiurnal frequencies. We analyse the spatial distribution, in a cross-section at 27^{o}S, of the spectral density of the temperature anomaly (deviation from the mean temperature) and mean velocities separated in diurnal and semidiurnal frequencies. Here we use the 13-month mean to calculate the temperature anomaly. The mean baroclinic energy flux is quantified for the diurnal and semidiurnal frequencies.

In Section 3.4 we analyse the origin of the internal tide (local or remote). We compare the phase and amplitude of the main harmonic components of the internal tide to the barotropic tide. We calculate the coherent portion of the internal tide to quantify the stationarity. The criticality, that relates the slope at which the internal tides propagate and the topographic slope, is also calculated to infer where is likely to generate internal tides in the study area. We use the model output to calculate the critical slope and generate a map of the criticality of the study area. We also compare the spectral density of the temperature anomaly (diurnal frequency) to the wind stress to infer about near-inertial waves generation.

3.2 Methods

3.2.1 Characterising the Internal Tides

We use data of temperature, and velocity from the mooring array filtered in diurnal and semidiurnal frequencies to characterise the internal tide. The data set used to characterise the internal tide are described in Chapter 2. The spectral density (SD) describes how the energy of a signal or a time series is distributed with frequency.

The discrete Fourier transform (DFT) is one of the basic methods to analyse the spectral density (Rigozo et al. 2005). The DFT relates a signal sampled in time or space to the same signal sampled in frequency. The Fourier transform is defined for a vector x with n uniformly sampled points by

$$y_{k+1} = \sum_{j=0}^{n-1} x_{j+1} e^{-2\pi i/n} \quad (1)$$

where *n* is the number of samples, *i* is the imaginary unit, *x* and *y*, the variables *j* and *k* range from 0 to n−1.

The SD of the temperature anomaly time series ($T_{d,sd}$ data) was calculated to analyse the dominant periodic signal in the study area. The spatial distribution, in a cross-section at 27°S, of the spectral density of the temperature anomaly for the entire time series (between May 2012 and June 2013) is analysed in diurnal and semidiurnal frequencies separated. The depth-integrated baroclinic flux is calculated using the horizontal velocities anomaly and pressure anomaly. The root mean squared (RMS) is defined as the square root of the mean square and is spatially analysed. Root Mean Square variance (RMSE) is the standard deviation of the residuals and measures how far from the regression line the data points are. It is also spatially analysed to measure how variable is the RMS.

3.2.2 Harmonic Analysis

The classical harmonic analysis uses a modelled tidal signal calculated by the sum of a finite set of sinusoids at specific frequencies (spectral lines) related to astronomical parameters. A least-squares fit can be used to determine the relative phase and amplitude of each frequency. These frequencies are specified by various combinations of sums and differences of integer multiples of 6 fundamental frequencies arising from planetary motions (Godin, 1972). These fundamental parameters represent effects of the rotation of the earth (lunar day of 24:8 h), the orbit of the moon around the earth (lunar

month of 27 days) and the earth around the sun (tropical year), and periodicities in the location of lunar perigee (8.85 years), lunar orbital tilt (18.6 years), and the location of perihelion (E21 000 years). The phase and amplitude data provides a compression of the data in the complete time series and can be used to synthesize time series of tidal effects at other times for predictive purposes.

T-Tide (Pawlowicz et al 2002) is a commonly used software package that calculates the amplitude and frequency) of the harmonic constituents needed to reproduce the tide. In this case, the tidal components are extracted from the 13-month observed temperature time series at each mooring and at each depth. The tidal harmonics are performed from the observed (hourly) temperature and velocity time series. We computed through time windows of 3 or 6 days, overlapping by 2 or 5 days, for the semidiurnal and diurnal constituents, respectively. We choose these time window lengths as they are long enough to extract the harmonics to perform the analysis described in Chapter 3 (Section 3.2.2) and we assume the subtidal circulation (that is influencing the stratification) to vary little over these periods since the cyclonic eddies can live for 1-4 weeks (Schaeffer et al. 2017). We use the T-tide MATLAB package written by Pawlowicz et al. (2002) to perform classical harmonic analysis and predictions using the analysed constituents.

3.2.3 Coherence of the Internal Tides

The coherent portion of the internal tide is the signal that can be estimated using the sum of the best harmonic fit from the time series filtered at tidal frequencies (diurnal and semidiurnal). The incoherent portion of the internal tide refers to the portion that is not predictable via harmonic analysis. It is a way to quantify the stationarity of the internal tide, e.g., the amplitude of the tide that oscillates in time but not in space. The coherent portion can provide information about the origin of the internal tide since the incoherent portion (non-stationary) can indicate shoaling of remote internal tides or interference of near-inertial waves that have the same frequencies as the internal tides.

The time series reconstructed from the harmonic constituents describes the coherent (stationary) internal tides and the residuals between the band-pass filtered time series, which is composed of coherent and incoherent, represent the incoherent (non-stationary) internal tides. Note that in the case of the diurnal internal tides, this incoherent portion will also include the near-inertial waves, which cannot be separated when filtering.

The coherent portion (CP) of the internal tide is then defined as:

$$CP = \left[1 - \left(\frac{(Filtered - Coherent)^2}{Filtered^2}\right)\right] \times 100 \quad (2)$$

The coherent portion of the internal tide is calculated using observed temperature data filtered at diurnal and semidiurnal frequencies as described in Chapter 2. The tidal harmonics constituents K_1 and O_1 (diurnal) and M_2 and S_2 (semidiurnal) are computed using the T-tide package (Pawlowicz et al. 2002) to perform classical harmonic analysis and predictions of the tidal signal. We computed over time windows of 3/6 days, overlapping by 2/5 days, for the semidiurnal and diurnal constituents respectively and the mean coherent portion is calculated for the entire period analysed (May 2012 to June 2013).

3.2.4 Phase of the Internal Tides

The phase of the internal tide relative to Greenwich is computed for each harmonic constituent. Temperature time series filtered in the tidal band (diurnal and semidiurnal) are used to calculate the phase. The phase is also computed using T-tide, over the time window of 3/6 days, overlapping by 2/5 days for the semidiurnal and diurnal constituents, respectively.

3.2.5 Barotropic Tide

The barotropic tide height and velocity is estimated using the global tidal model (TPXO 8.0) described in Chapter 2 (Section 2.3). Time series of the barotropic tide height is used to compare with the internal tide and analyse the cyclicity (spring-neap) of the internal tide. We also investigate if the internal tides are in phase with the barotropic tide.

3.2.6 Internal Tide Energy Flux

The velocity and pressure data, filtered at the diurnal and semidiurnal frequencies, were interpolated (linear interpolation) to a 10 m depth grid from the minimum to the maximum depth observed at each mooring. We calculate the barotropic and baroclinic energy flux and the conversion from barotropic to baroclinic energy at the diurnal and semidiurnal frequencies. Full details of the method are described in Nash et al. (2005) and Kerry et al. (2013) and are summarised here.

Barotropic tidal energy can be converted to baroclinic tides and the baroclinic processes can be calculated as an energy budget. The barotropic energy flux is calculated by

$$\mathrm{F_{bt}} = \frac{1}{T_\theta}\int_0^{T_\theta}\int_{-H}^{\eta} \mathrm{u}_{bt\theta}(t)\rho_o g[\eta_\theta(t) - z]dz\, dt, \quad (3)$$

where *T* is period, *H* is the depth of the water column, η is the surface elevation, u_{bt} is the barotropic velocity, ρ_0 is the density at the surface, *g* is gravity, *t* is time, *z* is depth and θ is the tidal period.

A portion of the local barotropic tidal energy is converted to baroclinic tidal energy over steep topography (Nash et al. 2005). The depth-integrated baroclinic energy flux is calculated from velocity (u'_θ) and pressure (p'_θ) perturbations (where the prime represents the perturbations).

$$\mathrm{u'}_\theta(z,t) = \mathrm{u}_\theta(z,t) - \bar{\mathrm{u}}_\theta(z) - \bar{\mathrm{u}}_0(t) \quad (4)$$

and

$$p'_\theta(z,t) = p(z,t) - \bar{p}_\theta(z) - \bar{p}_0(t), \quad (5)$$

where $\bar{\mathrm{u}}_\theta(z)$ and $\bar{p}_\theta(z)$ are time mean quantities (represented by the overbar).

In order to satisfy the baroclinic condition, the depth-averaged velocity and pressure perturbations have to be subtracted and are calculated by

$$\bar{\mathrm{u}}_0(t) = \frac{1}{H+\eta_\theta}\int_{-H}^{\eta_\theta}[\mathrm{u}_\theta(z,t) - \bar{\mathrm{u}}_\theta(z)]dz, \quad (6)$$

and

$$\bar{p}_0(t) = \frac{1}{H+\eta_\theta}\int_{-H}^{\eta_\theta}[p_\theta(z,t) - \bar{p}_\theta(z)]dz. \quad (7)$$

The depth-integrated baroclinic flux is calculated by

$$\mathrm{F_{bc}} = \frac{1}{T_\theta}\int_0^{T_\theta}\int_{-H}^{\eta} \mathrm{u'}_\theta(z,t)p'_\theta(z,t)\, dz\, dt. \quad (8)$$

The conversion of the barotropic energy into baroclinic energy is calculated by

$$C = \frac{1}{T_\theta}\int_0^{T_\theta}[p'_\theta(-H,t)w_{bt\theta}(-H,t)]\, dt, \quad (9)$$

using the pressure perturbation at the bottom and the vertical component of barotropic flow ($w_{bt\theta}$) and assuming incompressibility, $w_{bt\theta} = u_{bt\theta\,\Delta(-H)}$.

We compute the energy fluxes and conversion using spectral components. The barotropic to baroclinic conversion (C) can be calculated in terms of amplitudes and phases of pressure perturbation and vertical component of the barotropic flow defined by

$$C = 0.5{p'}_{\theta A}(-H)w_{bt\theta A}(-H)\cos(\emptyset_{p'} - \emptyset_{w_{bt}}), \quad (10)$$

where *A* refers to the amplitudes and Ø is the phase.

3.2.7 Criticality

The criticality (Ɛ) relates the slope at which the internal tides propagate and the topographic slope of the potential generation site. It is calculated as the ratio between the topographic slope (h) and the internal wave slope (s).

$$\text{Ɛ} = \frac{h}{s} \quad (11)$$

The internal wave slope, the ratio of horizontal and vertical wavenumbers, is given by Equation 12 where ω is the frequency of the internal wave, f is the inertial frequency and N is the buoyancy frequency.

$$s = \pm\sqrt{\frac{\omega^2 - f^2}{N^2 - \omega^2}} \quad (12)$$

Using the model output allows us to compute the criticality time-mean map. The Brunt-Vaisala (buoyancy) frequency squared (N^2), is given by the equation below, where *g* is gravity, *ρ* is density and *z* is depth.

$$\mathrm{N}^2 = \frac{-g}{\rho}\frac{d\rho}{dz} \quad (13)$$

The daily model output (Kerry et al. 2016) described in Section 2.5 was used to calculate the criticality in the study site. A map of where the internal tide is likely to be generated in the study area was analysed for the diurnal and semidiurnal tidal frequencies (Figure 29). Where criticality above a ratio of 1 suggests possibly internal tide generation.

3.2.8 Wind Stress

The wind stress is analysed to observe if there is evidence of near-inertial waves generation by the action of the wind force in the study site. The method used to calculate the wind stress is proposed by Large and Pond (1981) and is calculated by

$$\tau = C_D \rho_{air} U_{10}^2, \quad (14)$$

where U_{10} is the wind speed at 10 m above the surface, ρ_{air} is the air density (1.22 kg m^{-3}) and C_D is the dimensionless drag coefficient (0.0012 for $4 < U_{10} < 11$ m s^{-1}).

3.2.9 Rotary Spectra

The near-inertial waves have counter-clockwise motion in the southern hemisphere and the rotary spectra are analysed to observe if the current has a clockwise or counter-clockwise motion. Rotary spectra decompose vector time series of current velocity into clockwise and counter-clockwise components. Rotary frequency spectra (Mooers, 1973) are computed by Fourier transforming the complex velocity vector u+ iv to identify rotational direction such that positive/negative frequencies correspond to counterclockwise/clockwise motions, respectively.

The current velocity components (u and v) are calculated by:

$$u(t) = A\cos(\omega t) + B\sin(\omega t), \quad (15)$$

$$v(t) = C\cos(\omega t) + D\sin(\omega t). \quad (16)$$

Where t is time and ω is the angular frequency, A, B, C and D are the Fourier cosine and sine amplitude spectra, which are real-valued random variables.

The equations 15 and 16 can be calculated in complex form as:

$$R = u + iv, \quad (17)$$

$$R = A\cos(\omega t) + B\sin(\omega t) + i[C\cos(\omega t) + D\sin(\omega t)], \quad (18)$$

$$R = (A + iC)\cos(\omega t) + (B + iD)\sin(\omega t). \quad (19)$$

The sum of clockwise and counter-clockwise rotating components is calculated by

$$R = R^+ e^{i\omega t} + R^- e^{-i\omega t}, \quad (20)$$

$$R = R^{+}(cos(\omega t) + i\sin(\omega t)) + R^{-}(cos(\omega t) - i\sin(\omega t)), \quad (21)$$

$$R = (R^{+} + R^{-})cos(\omega t) + i\sin(\omega t)) + (R^{+} - R^{-})i\sin(\omega t)), \quad (22)$$

Note that $e^{i\omega t} = cos(\omega t) + i\sin(\omega t)$ is counter-clockwise in the complex plane, and $e^{-i\omega t} = cos(\omega t) - i\sin(\omega t)$ is clockwise.

Comparing equations 19 and 22,

$$R = (A + iC)cos(\omega t) + (B + iD)\sin(\omega t)), \quad (23)$$

The rotation, counter-clockwise and clockwise, can be separated as:

$$R^{+} = \frac{1}{2}[A + D + i(C - B)], \quad (24)$$

$$R^{-} = \frac{1}{2}[A - D + i(C - B)]. \quad (25)$$

The magnitudes of the rotary components are calculated by

$$|R^{+}| = \frac{1}{2}|(A + D)^2 + (C - B)^2|^{1/2}, \quad (26)$$

$$|R^{-}| = \frac{1}{2}|(A - D)^2 + (C + B)^2|^{1/2}. \quad (27)$$

3.3 Results

3.3.1 Internal Tides Characteristics

The data from the moorings located above the continental slope (SEQ400 and EAC1) are used to characterize the internal tides. The spectral density of the raw temperature data from a mooring located above the continental slope (SEQ400) shows the four dominant periodic signals of the internal tide (Figure 14): diurnal tidal components K_1 and O_1 and semidiurnal tidal components M_2 and S_2. The components K_1 and O_1 are the principal diurnal lunar, M_2 is the principal semidiurnal lunar and S_2 is the principal semi-diurnal solar. Near the ocean bottom, at 364 m, the K_1 component of the diurnal tide has the highest spectral density (1.63° C^2/(1/day)), followed by semidiurnal M_2 (1.57° C^2/(1/day)), diurnal tide O_1 (1.44° C^2/(1/day)) and semidiurnal S_2 (0.4° C^2/(1/day)). Note that near-inertial waves have a frequency close to the diurnal frequency, and it is very close to the frequency of the harmonic O_1 (the inertial period is 26 hrs at 27°S).

The time series of temperature were filtered in the diurnal and semidiurnal range for the period between May 2012 and June 2013 described in Chapter 2. The time series of the temperature anomaly at the diurnal frequency, (mooring SEQ400), show that the peaks of temperature are higher close to the surface reaching 2.07° C at 90 m depth (Figure 15a). The root mean squared (RMS) of the temperature anomaly time series is also higher (0.35° C) close to the surface (~ 90 m). The minimum RMS (0.21° C) is observed in the middle of the water column, at 214 m depth (Figure 15b). The RMS close to the bottom is 0.28° C at 364 m depth, higher than the water column below 170 m depth (Figure 15b). The root mean squared variance (RMSE) of the temperature anomaly is also high (> 0.4° C) close to the surface above 127 m and close to the bottom (364 m). The minimum RMSE occurs at 214 m depth (0.30° C).

The peaks of the temperature of the semidiurnal internal tide have a maximum of 1.34° C at 127 m depth and 1.27° C close to the bottom at 364 m depth (Figure 15c). The RMS of the temperature near the bottom is higher than the water column above (170 m, 214 m, and 271 m), reaching 0.26° C at 364 m depth in the mooring SEQ400 (Figure 15d). The RMSE is high (> 0.3° C) near the bottom and close to the surface, and the minimum (0.16° C) occurs at 214 m depth.

The time series of the velocities, zonal ($U_{d,sd}$) and meridional ($V_{d,sd}$), filtered at diurnal and semidiurnal frequencies, shows the variability of the horizontal displacement of the internal tide in the study area. Figure 16 shows an example of the velocities of the internal tides reaching the bottom of the continental slope (mooring EAC1). The velocities show a peak of the internal tide on 18th October 2012 and reach more than 0.1 m s^{-1} for diurnal and semidiurnal frequencies. The meridional velocity reaches ±0.1m s^{-1} near the bottom of the continental slope (1020 m depth) on 22nd October 2012 and the internal tide velocities decrease substantially after 23rd October 2012.

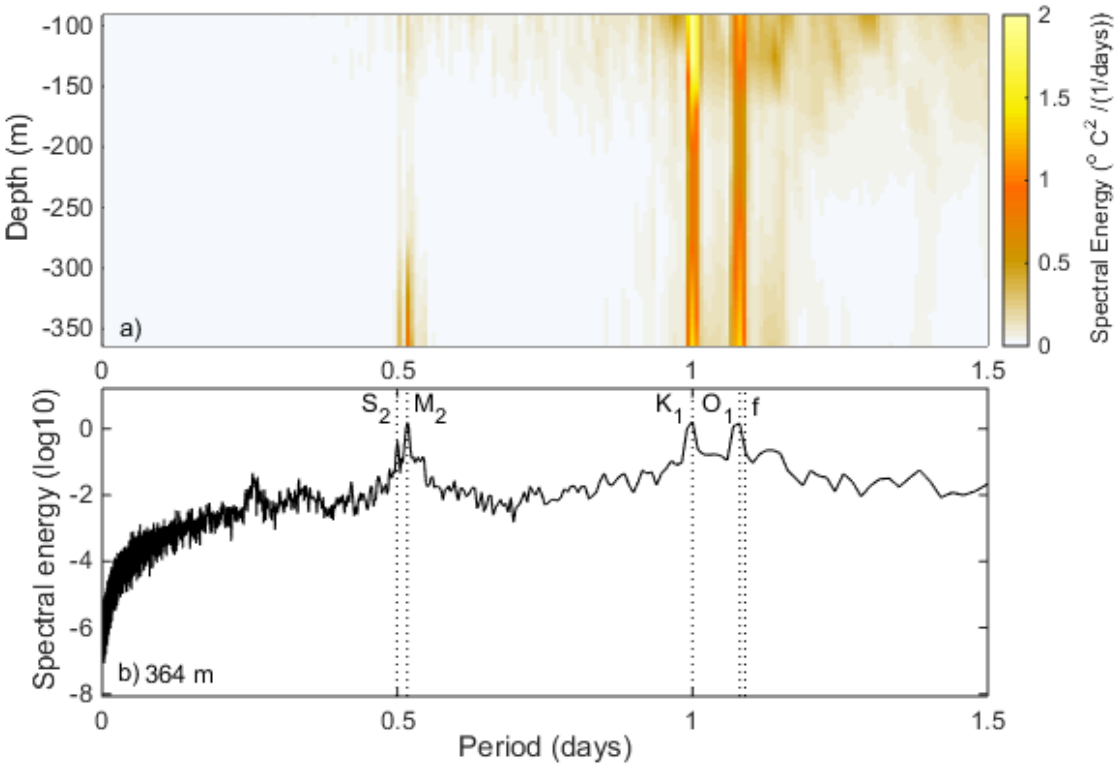

Figure 14: a) Spectral density of the non-filtered temperature time series at the SEQ400 mooring between depths of 90 and 364 meters, deployed from 01/05/2012 to 06/06/2013. **b)** Spectral density at 364 m depth showing the peaks of energy (dotted line) at diurnal tide (K_1 and O_1), semidiurnal tide (S_2 and M_2) and inertial frequency (f).

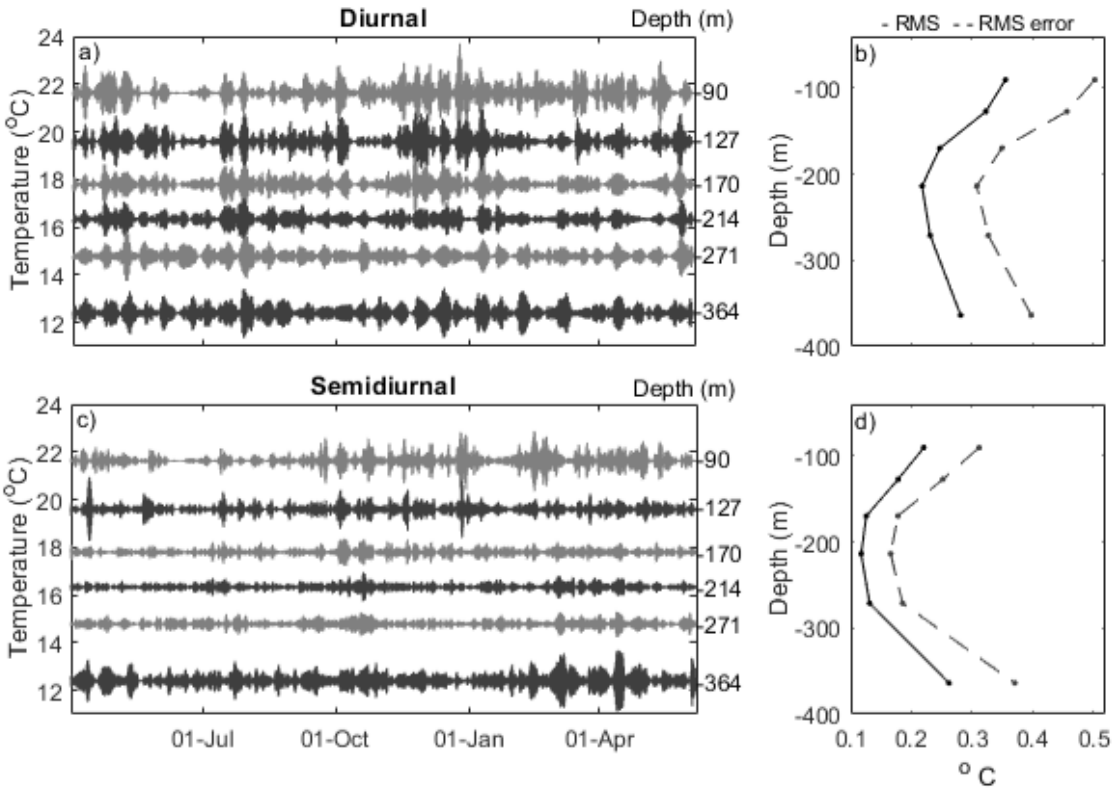

Figure 15: Time series of the temperature of the mooring SEQ400, filtered at **a)** diurnal and **c)** semidiurnal tidal band between May 2012 and June 2013. Profiles of the root mean squared (RMS) and root mean squared variance (dashed line) of the **b)** diurnal and **d)** semidiurnal frequencies.

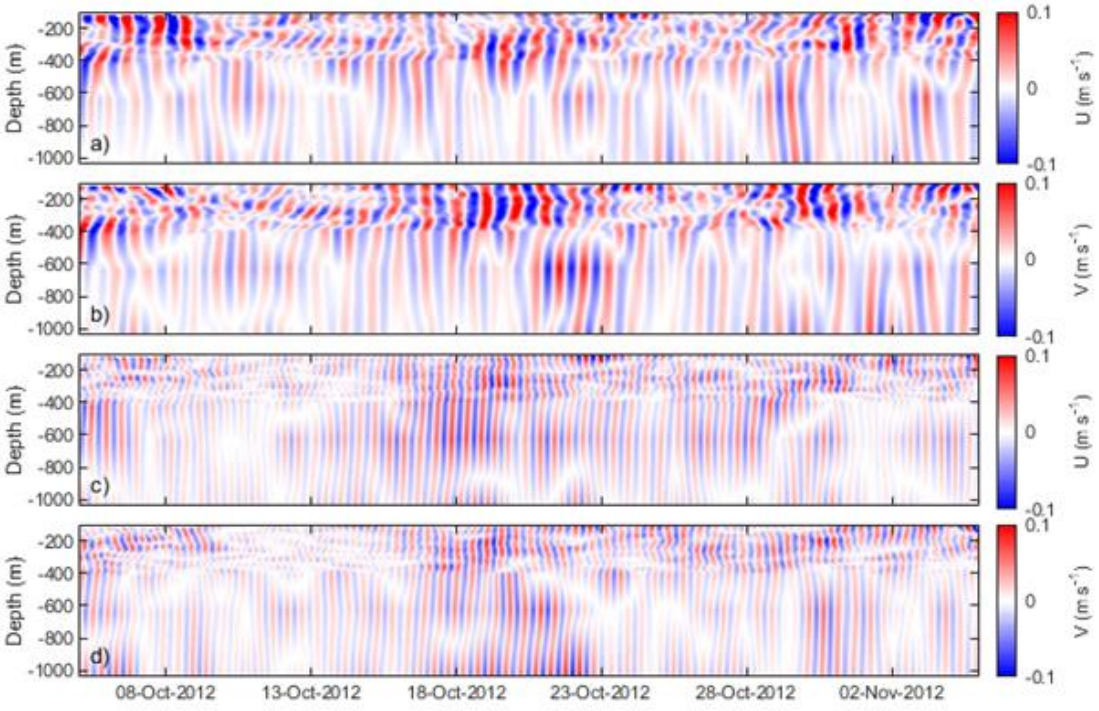

Figure 16: Horizontal components of the diurnal velocity, **a)** zonal and **b)** meridional (U_d and V_d), and semidiurnal velocity, **c)** zonal and **d)** meridional (U_{sd} and V_{sd}), between the period of 5th October and 5th November 2012 in the mooring EAC1.

The maximum spectral density was calculated from the temperature time series filtered at diurnal and semidiurnal bands observed in each mooring between May 2012 and June 2013. The spectral density is highest (higher than 1° C^2/(1/day)) in the top 500 m of the water column (Figure 17). It is also highest above the continental slope (SEQ200, SEQ400, EAC1, EAC2 and EAC3). It decreases with distance from the slope to the further offshore moorings (EAC4 and EAC5). The spectral density of the diurnal frequency reaches 2.5° C^2/(1/day) at 127 m depth and 1.6° C^2/(1/day) near the bottom (~ 364 m), observed from the mooring SEQ400 while the water column (169 – 271m) is lower than 1° C^2/(1/day) (Figure 17a). The highest spectral density in the semidiurnal frequency occurs near the bottom over the slope (SEQ400) and reaches 1.6° C^2/(1/day) (Figure 17b).

The root mean squared (RMS) of the velocity anomaly, in the diurnal band, was calculated for the period between May 2012 and June 2013 for each mooring. The root mean squared (RMS) of the diurnal internal tides velocities, zonal ($U_{d,sd}$), meridional ($V_{d,sd}$) and vertical ($W_{d,sd}$) components, are higher above 500 m depth (Figure 18). The highest RMS were observed at the water column above the continental slope. The maximum RMS of the horizontal velocities occurs in the mooring SEQ200 where the zonal velocity is 0.06 m s^{-1} near the bottom at 191 m depth and the meridional velocity is 0.07 at 50 m depth (Figure 18a,b). The RMS of the vertical velocity is higher in the mooring EAC2 at 66 m depth and the highest near bottom velocity is observed in the mooring SEQ400 reaching 0.013 m s^{-1} at 344 m depth (Figure 18c).

The velocity of the diurnal internal tide varies more (high RMSE) at the water column above 250 m (Figure 19). The root mean squared variance (RMSE) is higher in the moorings above the continental slope compared to the moorings offshore and the RMSE near the bottom of the continental slope (moorings SEQ200, SEQ400, EAC1 and EAC2) is higher compared to the water column above. The highest RMSE of the horizontal velocities occurs in the mooring SEQ200, where zonal velocity is 0.09 m s^{-1} at the near bottom (191 m) and meridional velocity is 0.11 m s^{-1} at 50 m depth. The maximum RMSE of the diurnal vertical velocity is 0.025 m s^{-1} at 66 m depth in the mooring EAC2.

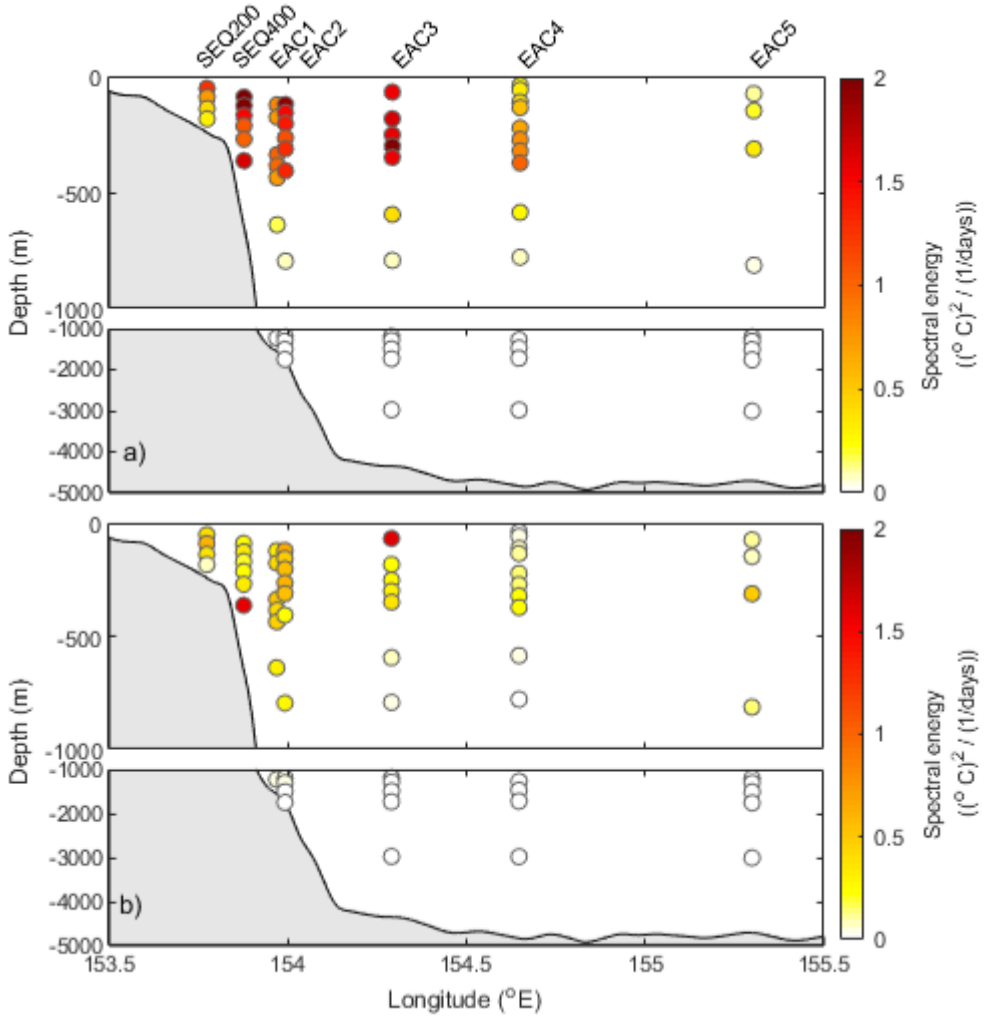

Figure 17: Maximum spectral density of time series of temperature filtered at **a)** diurnal and **b)** semidiurnal tidal band between May 2012 and Jun 2013 at each of the observation points on the mooring array (SEQ200, SEQ400, EAC1, EAC2, EAC3, EAC4 and EAC5).

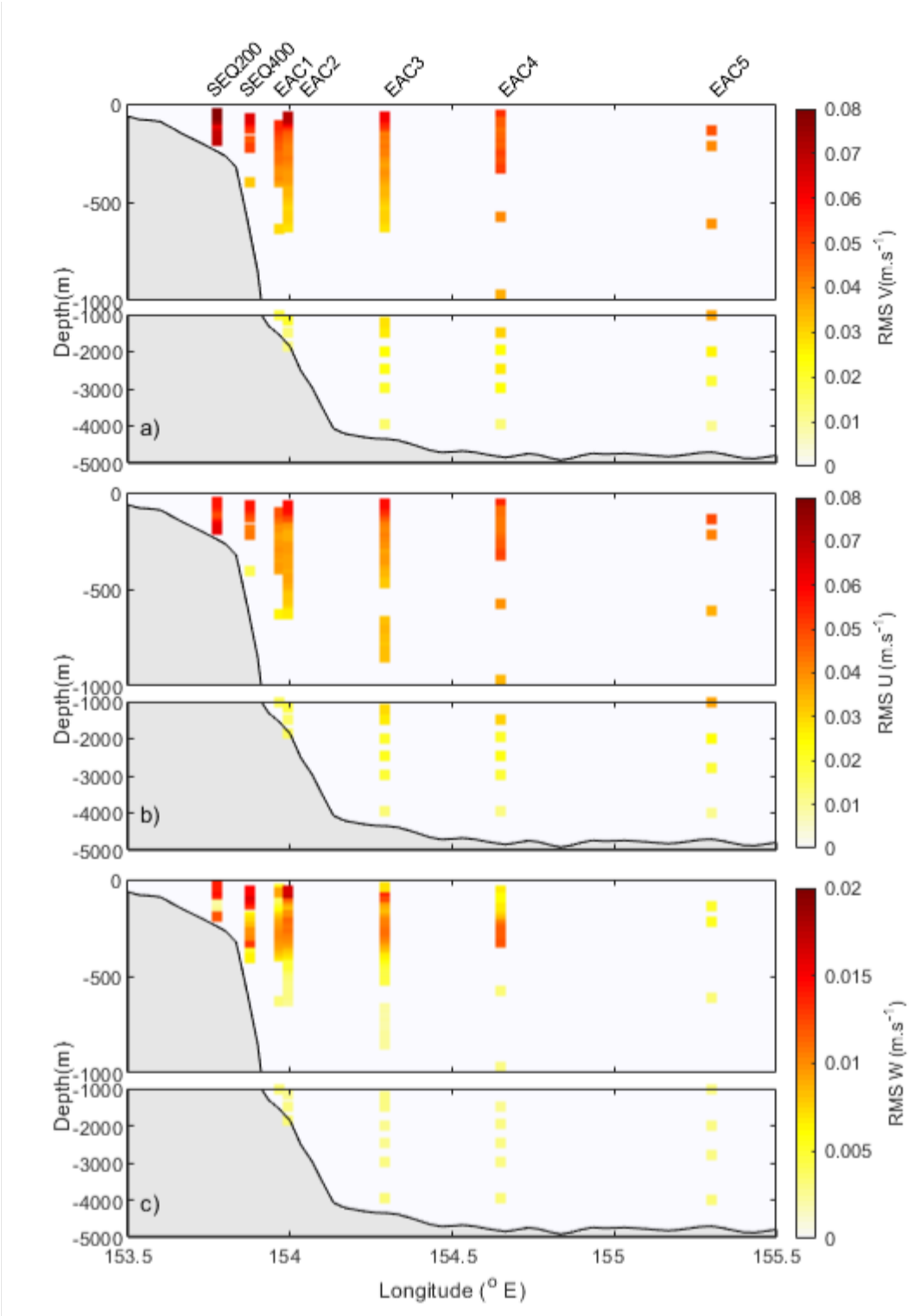

Figure 18: Cross-section of the root mean squared of the diurnal internal tides velocities anomaly, **a)** meridional, **b)** zonal and **c)** vertical, from the mooring array (SEQ200, SEQ400, EAC1, EAC2, EAC3, EAC4 and EAC5) over the period between May 2012 and June 2013.

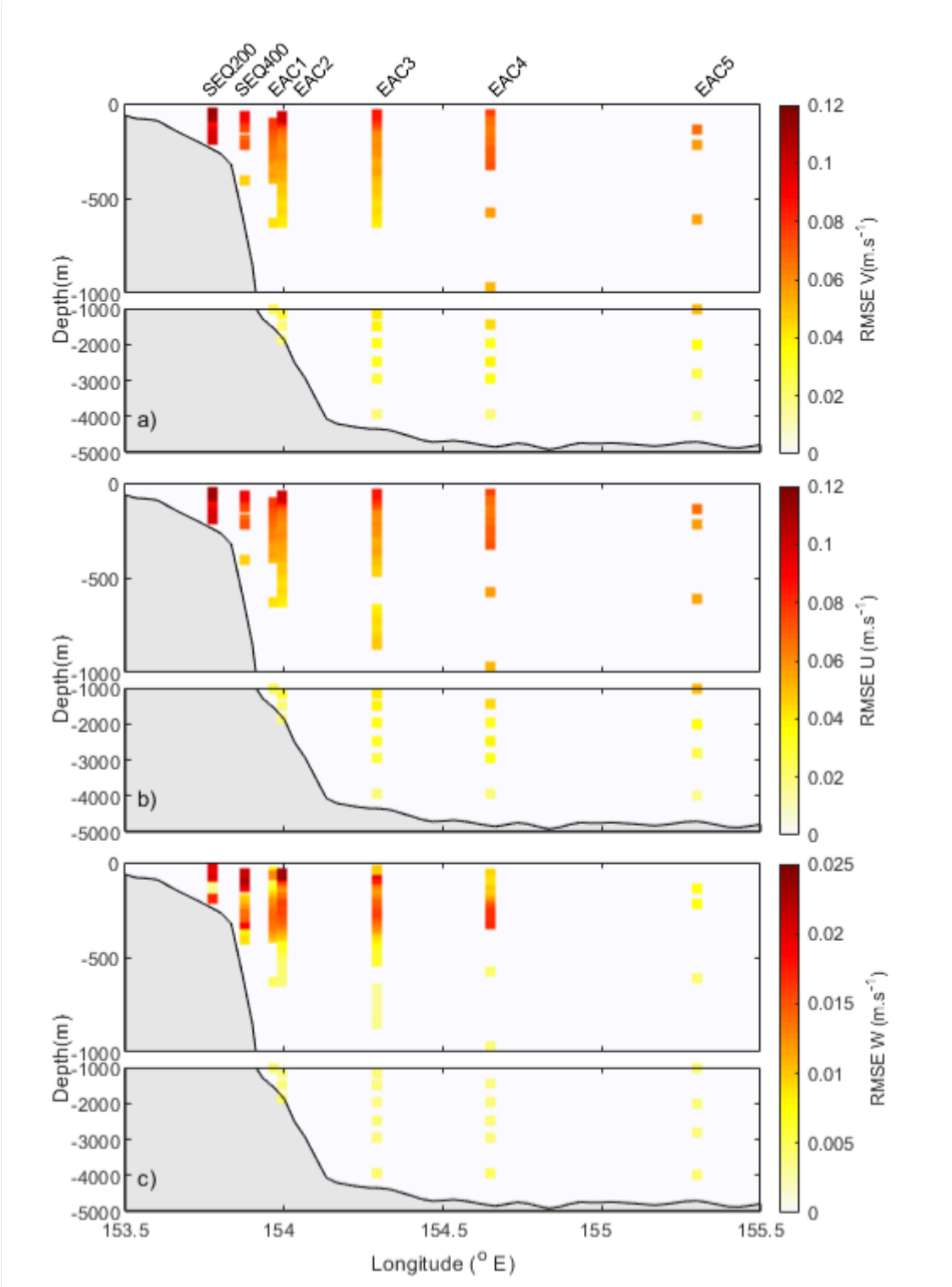

Figure 19: Cross-section of root mean squared variance of the diurnal velocities anomaly, **a)** meridional, **b)** zonal and **c)** vertical, from the mooring array SEQ200, SEQ400, EAC1, EAC2, EAC3, EAC4 and EAC5, over the period between May 2012 and June 2013.

The RMS of the semidiurnal velocities were quantified for the period between May 2012 and June 2013. The highest RMS (> 0.04 m s^{-1}) of the horizontal velocity (zonal and meridional) occurs close to the surface (above 80 m depth) in the moorings SEQ200, EAC2 and EAC3 (Figure 20a,b). The horizontal velocities of the semidiurnal internal tide are higher than 0.03 m s^{-1} over the entire water column observed in the mooring SEQ200. The RMS of the near-bottom velocity is higher than the water column above, in the moorings above the continental slope (SEQ200, SEQ400, EAC1 and EAC2) reaching 0.03 m s^{-1} (meridional) and 0.034 m s^{-1} (zonal) at 1881 m depth in the mooring EAC2. The maximum RMS velocity of the vertical displacement occurs at 113 m depth in the mooring EAC3 and reaches 0.01 m s^{-1} (Figure 20c). The RMS of the vertical velocity of the semidiurnal internal tide is close to 0.01 m s^{-1} near the bottom of the continental slope (moorings SEQ200 and SEQ400), also higher than the water column above until 200 m depth.

The root mean squared variance (RMSE) of the semidiurnal internal tide velocity is higher above 153 m approximately (Figure 21). The maximum RMSE of the horizontal velocity (zonal and meridional) occurs at 61 m depth, and the maximum RMSE of the vertical velocity occurs at 113 m depth, both in the mooring EAC3 (Figure 21a,b). The moorings located above the continental slope (moorings SEQ200, SEQ400, EAC1 And EAC2) varies more from the root mean squared (> 0.05 m s^{-1}) compared to the moorings offshore (EAC4 and EAC5). Also, the velocity RMSE near the bottom is higher compared to the water column above for the moorings located above the continental slope. The maximum near-bottom RMSE of the velocity occurs in the mooring SEQ400 at 364 m. The mooring EAC2 also has a high variability of the internal tide velocities near the bottom at 1881 m depth, where the RMSE of the zonal velocity is 0.045 m s^{-1}, meridional velocity is 0.03 m s^{-1} and vertical velocity is 0.006 m s^{-1}.

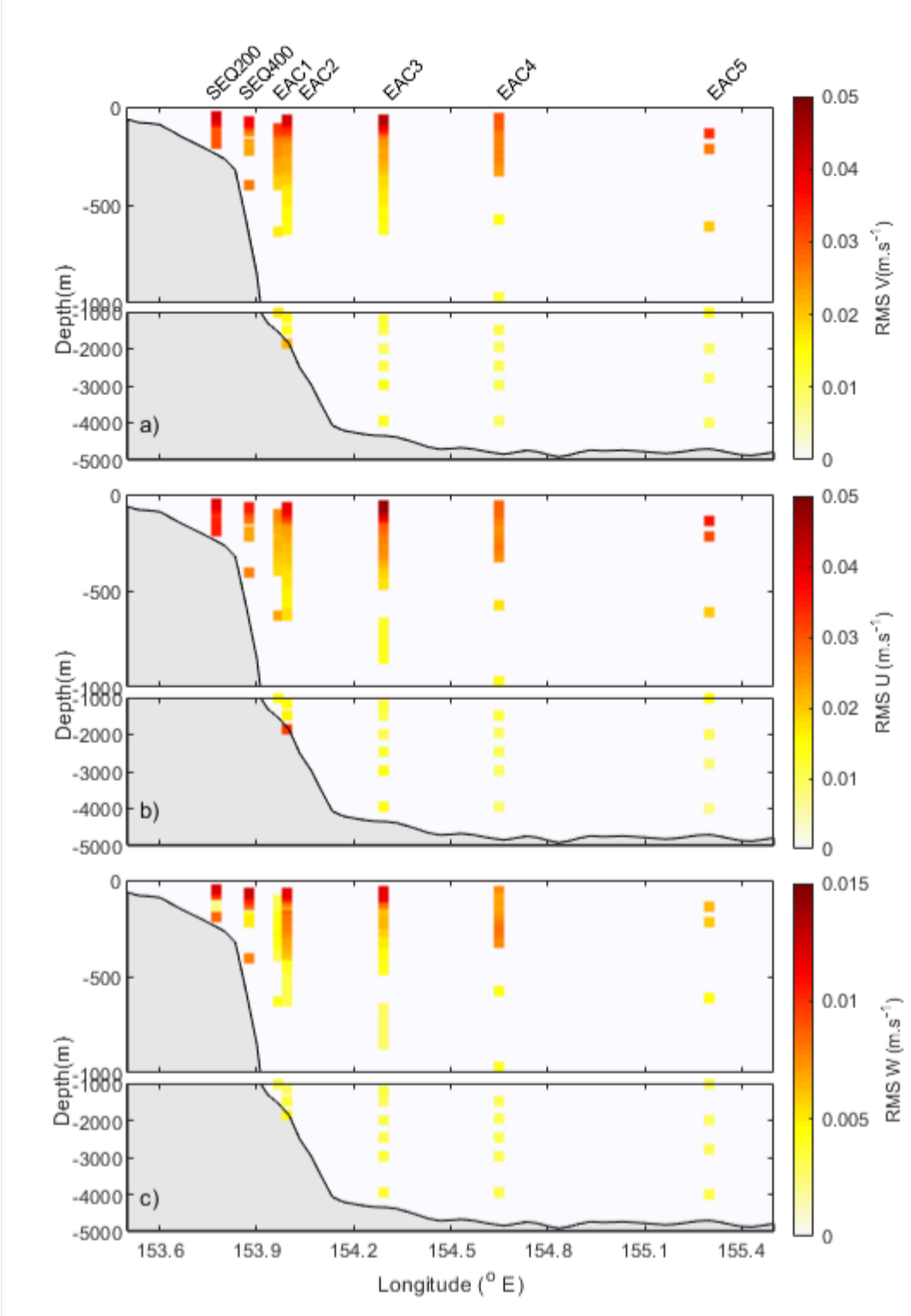

Figure 20: Cross-section of the mean root squared of the semidiurnal internal tides velocities anomaly, **a)** meridional, **b)** zonal and **c)** vertical, from the mooring array (SEQ200, SEQ400, EAC1, EAC2, EAC3, EAC4 and EAC5) over the period between May 2012 and June 2013.

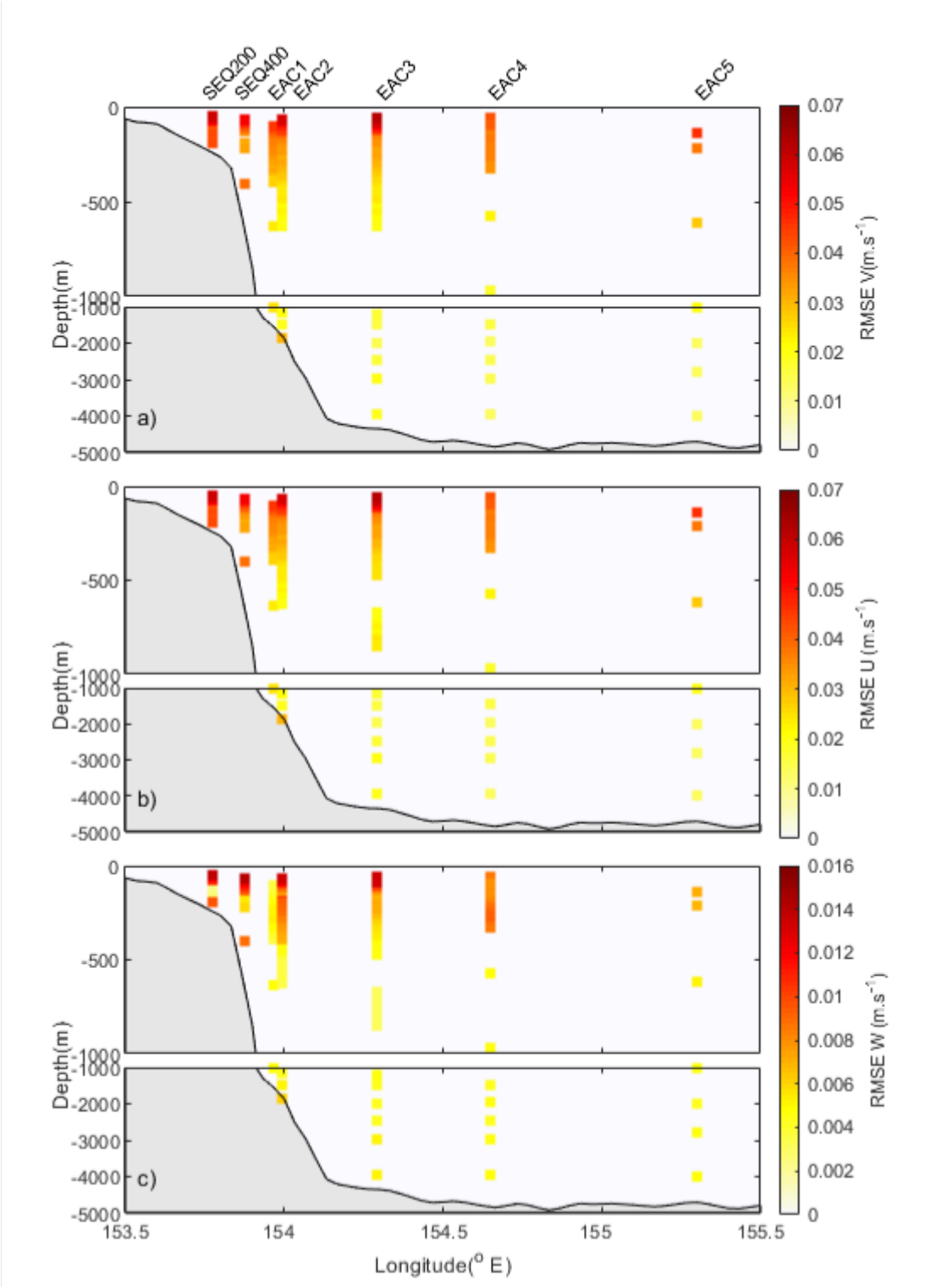

Figure 21: Cross-section of the root mean squared variance of the semidiurnal internal tides velocities anomaly, **a)** zonal, **b)** meridional and **c)** vertical, from the mooring array SEQ200, SEQ400, EAC1, EAC2, EAC3, EAC4 and EAC5, over the period between May 2012 and June 2013.

Energy flux is important for understanding internal wave generation to identify energy sources. The depth-integrated baroclinic energy flux is calculated from velocity and pressure perturbations for the diurnal and semidiurnal frequencies (Equations 4 to 8). The diurnal baroclinic energy fluxes vary considerably over the 13 months (Table 5). Over the 400m isobath (at SEQ400) the standard deviation (0.39 kW m^{-1}) of the baroclinic flux is higher than the mean (0.35 kW m^{-1}) and reaches a maximum of 4.3 kW m^{-1}. The mean diurnal baroclinic energy flux is directed to the south at all mooring sites except the offshore mooring EAC5, which has a northeast direction (Figure22a). The highest mean flux occurs in the mooring EAC3, located at the base of the continental slope, (2.73 kW m^{-1}) followed by 1.85 kW m^{-1} in the mooring EAC5. High variability of the energy flux is also observed at sites (EAC3 and EAC5) illustrated by the ellipses in Figure 22. The maximum baroclinic flux occurs at 95 m (3.5 kW m^{-1}, 3.1 kW m^{-1}, 0.8 kW m^{-1} and 2 kW m^{-1}) in the moorings EAC3 EAC2, EAC1 and SEQ400 respectively (Figure 22c). The maximum baroclinic flux is at 60 m in mooring SEQ200 (1 kW m^{-1}), at 240 m in the mooring EAC5 (1.6 kW m^{-1}) and at 160 m in the mooring EAC4 (1.2 kW m^{-1}).

The semidiurnal baroclinic flux is lower in magnitude compared to the diurnal flux (note the difference in scale between Figure22a and 22b) but also displays considerable variability in both magnitude and direction (Figure 22b). The highest mean and standard deviation of the semidiurnal energy flux (both 0.46 kW m^{-1}) occurs in the mooring EAC3 with a southwest direction. The semidiurnal energy flux in the mooring EAC5 has a northwest direction with a mean of 0.39 kW m^{-1}. The energy flux above the continental slope at the mooring SEQ400 has a southeast direction reaching a maximum of 4.3 kW m^{-1} with a mean and standard deviation of 0.35 kW m^{-1} and 0.37 kW m^{-1}, respectively. The direction of the baroclinic flux at EAC2 and EAC5 is highly variable evidenced by the circular shape of the variance ellipses (Figure 22b). The highest mean baroclinic flux (1.68 kW m^{-1}) is in the mooring EAC3 at 55 m (Figure 22d), followed by the mooring EAC2 at 70 m (1.3 kW m^{-1}), EAC5 at 170 m (0.9 kW m^{-1}), SEQ400 at 90 m (0.43 kW m^{-1}), EAC4 at 150 m (0.38 kW m^{-1}), SEQ200 at 60 m (0.29 kW m^{-1}) and EAC1 at 130 m (0.25 kW m^{-1}).

Table 5: Mean and standard deviation of the depth-integrated baroclinic flux (kW m^{-1}), in the diurnal and semidiurnal band, at the location of the moorings SEQ200, SEQ400, EAC1, EAC2, EAC3, EAC4 and EAC5.

Diurnal	Mean	STD	Max	Min
SEQ200	0.11	0.13	1.21	0.001
SEQ400	0.35	0.39	4.30	0.003
EAC1	0.34	0.37	3.16	0.002
EAC2	1.24	1.14	11.70	0.026
EAC3	2.73	2.34	13.39	0.044
EAC4	1.27	1.27	15.38	0.015
EAC5	1.85	2.43	22.64	0.012
Semidiurnal				
SEQ200	0.01	0.01	0.22	0.0001
SEQ400	0.04	0.04	0.51	0.0003
EAC1	0.06	0.06	0.58	0
EAC2	0.23	0.25	1.77	0.0019
EAC3	0.46	0.46	4.20	0.0014
EAC4	0.20	0.22	2.24	0.0015
EAC5	0.39	0.45	3.84	0.0007

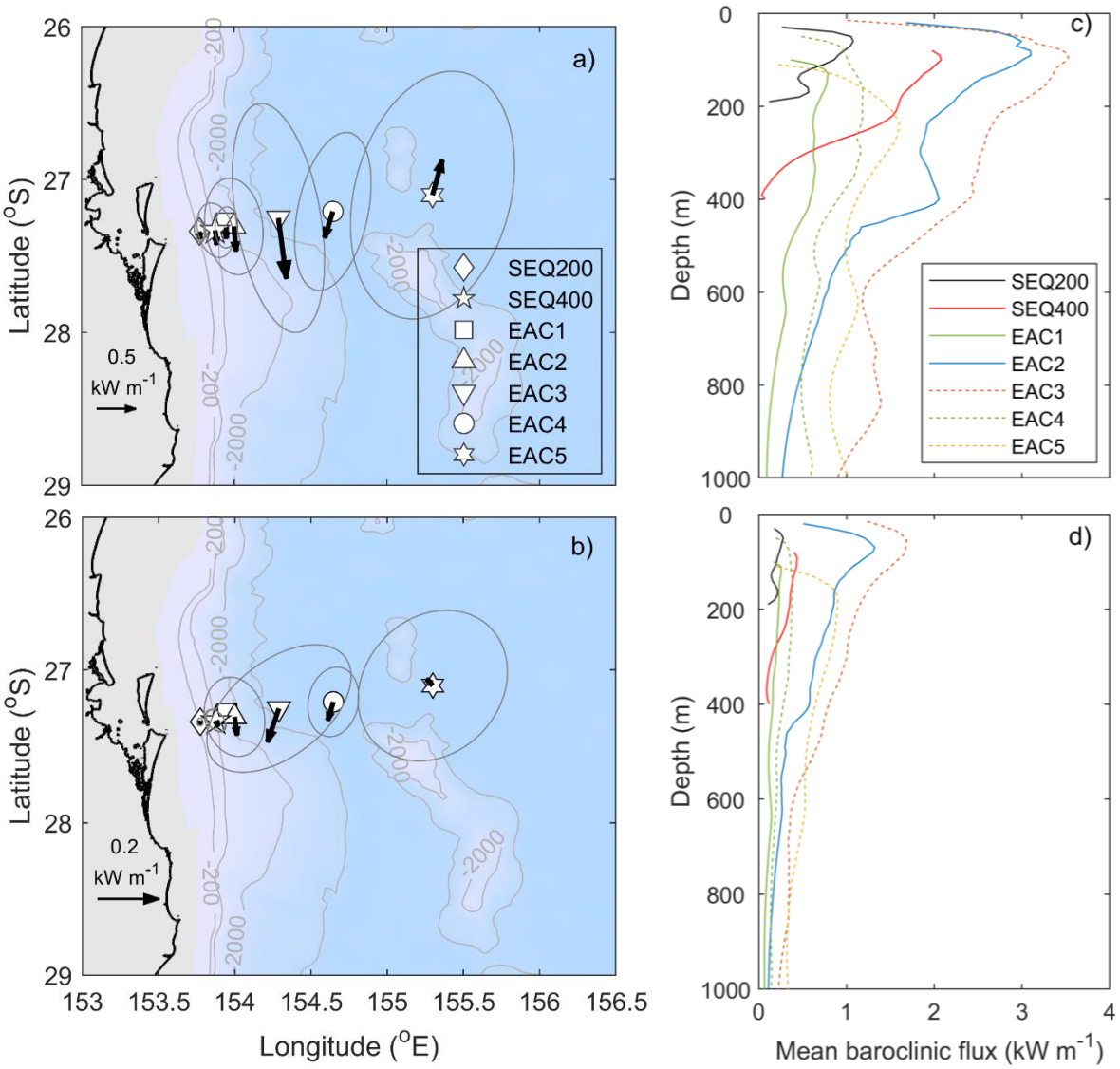

Figure 22: Mean baroclinic energy flux (arrows) and variance (ellipses) of the **a)** diurnal and **b)** semidiurnal frequencies calculated at the mooring locations between the period of May 2012 and June 2013. c) Time-mean diurnal and d) semidiurnal baroclinic flux profile.

3.3.2 Barotropic Tide

The semidiurnal harmonic component M_2 of the barotropic tide, in the mooring SEQ400, has the highest amplitude (0.5 m) with a period of 12.4 hrs. It is followed by the diurnal component K_1, with an amplitude of 0.3 m and a period of 23.9 hrs (Table 6). The phase related to Greenwich is 299° and 355° for the components M_2 and K_1, respectively. The harmonic components O_1 and S_2 have amplitudes of 0.2 m and phase of 322° and 309°, respectively.

Table 6: Tide surface amplitudes, periods and phases of the dominant periodic signals located at the mooring SEQ400 and calculated from the global tidal model (TPXO).

Harmonics	Amplitude (m)	Period (hr)	Phase (°)
K1	0.3	23.9	355.11
O1	0.2	25.8	322.29
M2	0.5	12.4	299.69
S2	0.2	12.0	309.90

3.3.3 Ocean Current and Vertical Structure

The current and vertical structure (stratification) of the ocean can modulate the generation of the internal tide. We use the model output data, described in Section 2.5, to analyse the velocity of the current and the vertical structure at the moorings' location. The buoyancy frequency squared (N^2) is used to infer the stratification. The data simulated by the model do not include tide forces, and it is used to describe the dynamics of the ocean. The mean current velocities between May 2012 and June 2013 are calculated using the model output, and the analysis is focused above 1000 m depth where there is more influence of the mesoscale features and where higher internal tide energy is observed, presented in Section 3.3.1.

The results show a strong offshore current (> 0.3 m s^{-1}) above the continental slope (~300 m) m depth (Figure 23a). The mean is weaker (< 0.2 m) offshore of the mooring EAC4 and close to zero (< 0.1 m s^{-1}) below 500 m depth offshore the mooring EAC3. The East Australian Current (EAC) is observed with a strong (0.5 m s^{-1}) mean current (Figure 23b) between the surface and 78 m depth flowing southward above the continental slope. The southward velocity extends from the continental slope until ~88 km offshore (mooring EAC4). Higher mean northward flow (> 0.1 m s^{-1}) is observed offshore in the mooring EAC5 near the surface (>100 m depth) and below 600 m depth in the mooring EAC4.

The mean buoyancy frequency squared (N^2) is calculated for the cross-section at latitude 27°S between May 2012 and June 2013. Higher N^2 (> $2x10^{-4}$ s^{-2}) occurs above the continental slope close to the continental shelf at 59 m depth (Figure 24a). Comparing the stratification between the moorings' locations, the highest N^2 (> $1x10^{-4}$ S^{-2}) occurs in the moorings above the continental slope (SEQ200, SEQ400, EAC1 and EAC2) and the mooring EAC3. Below 80 m depth, the stratification decreases substantially and N^2 is lower than $5x10^{-5}$ s^{-2} below 300 m depth.

Above the continental slope, the temperature is high (> 22° C) close to the surface above 102 m depth and decrease linearly over depth until 600 m reaching 8° C (Figure 24b). The salinity is high (> 35.6) in the subsurface between 95 and 200 m depth and decreases substantially (< 34.7) below 456 m depth (Figure 24c).

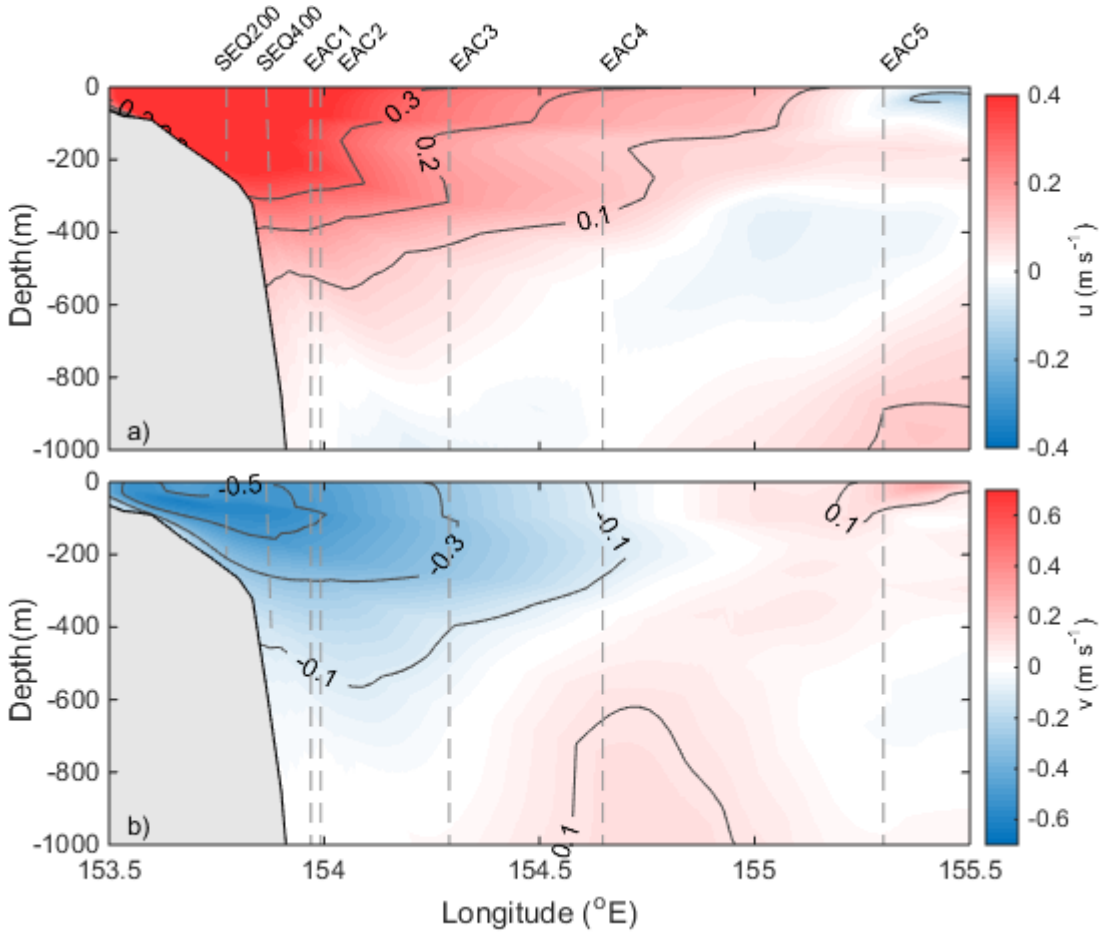

Figure 23: Cross-sections of the mean components of the velocity, **a)** zonal and **b)** meridional, calculated for the period between May 2012 and June 2013, at Latitude 27°, using the EAC-ROMS model output.

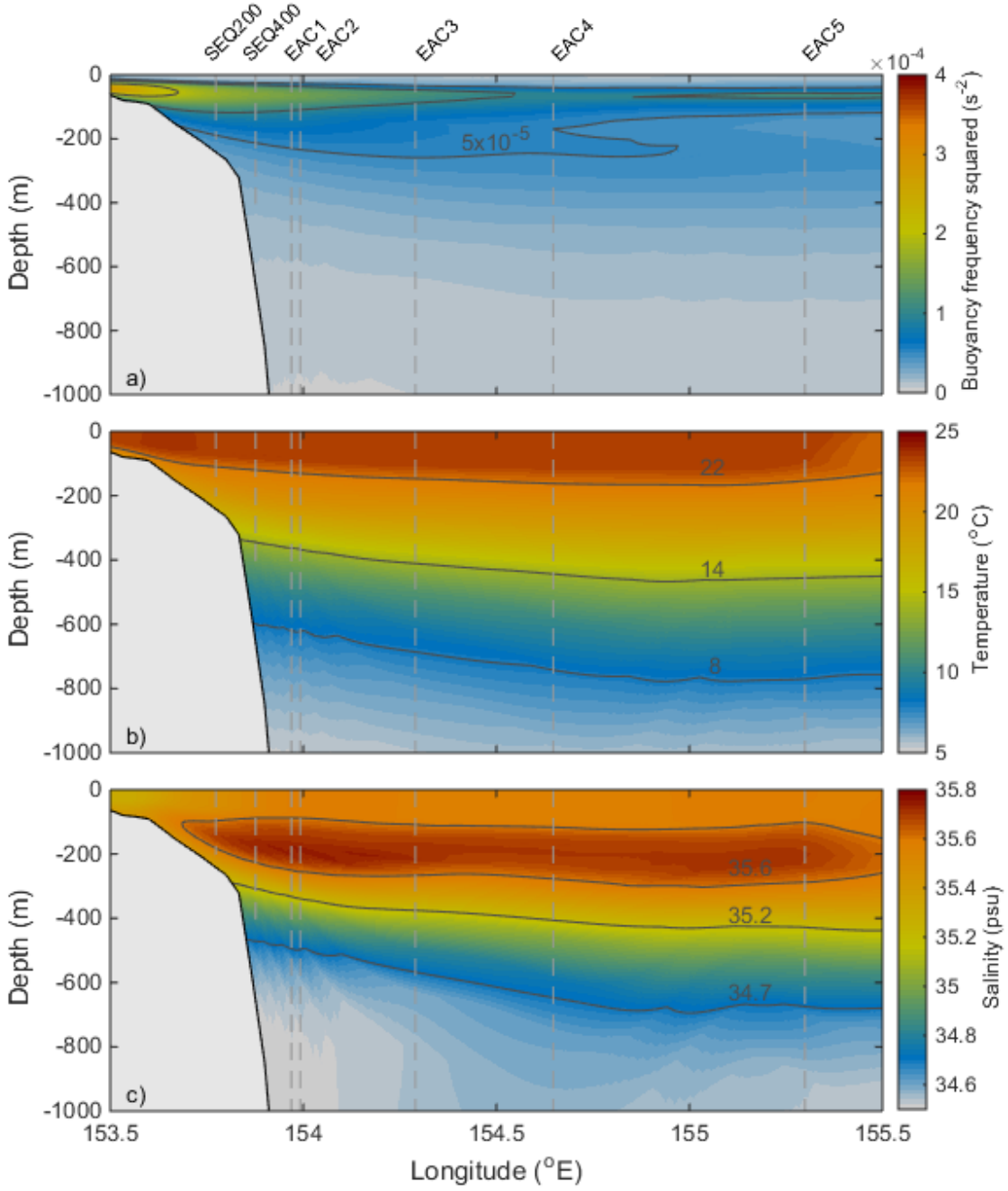

Figure 24: Cross-section of the mean **a)** buoyancy frequency squared (N^2), **b)** temperature and **c)** salinity analysed between May 2012 and June 2013, at Latitude 27°S, using data from the model output.

3.3.4 Origin of the Internal Tide

3.3.4.1 Coherent portion

The coherent portion of the diurnal and semidiurnal internal tide is an estimate of the stationarity of the internal tide. The coherent portion is calculated using different fitting windows to analyse the sensitivity of the coherent portion over different time windows (Figure 25). The circle is the coherent portion calculated for the entire period of data (mooring SEQ400) with about 20% of coherence. The black line is calculated using 3 days windows, the same used in Figure 29b, and it shows that the coherent portion of the semidiurnal internal tide is mostly higher than 60% and temporally variable.

The highest coherent portions (76% and 78%), calculated for the diurnal frequency, occur near the bottom (364 m and 271 m respectively) of the continental slope (mooring SEQ400). The mean coherent portions calculated for the moorings EAC4 and EAC5 have less than 50% of coherence, and the smallest (27%) portion occurs about 3000 m depth of both moorings (Figure 26a).

The semidiurnal coherent portion is higher than the diurnal and higher than 50% in all moorings except the mooring EAC4 near the surface (40 m - 135m) where the coherent portion is about 33% - 46%. The mean of the coherent portion reaches 90% near the bottom (364m) above the continental slope (mooring SEQ400) and is higher than 70% in the entire water column (Figure 26b).

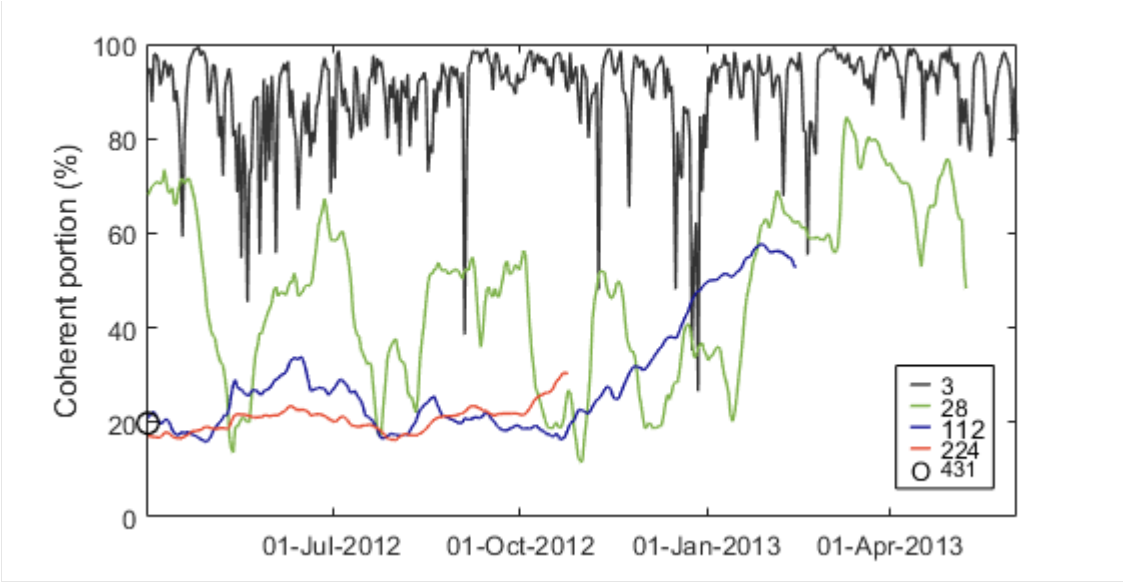

Figure 25: Coherent portion sensitivity of semidiurnal tide (M2 and S2) using different fitting windows (3, 28, 112, 224 and 431 days) of temperature data near-bottom (364 m, mooring SEQ400) of the continental slope.

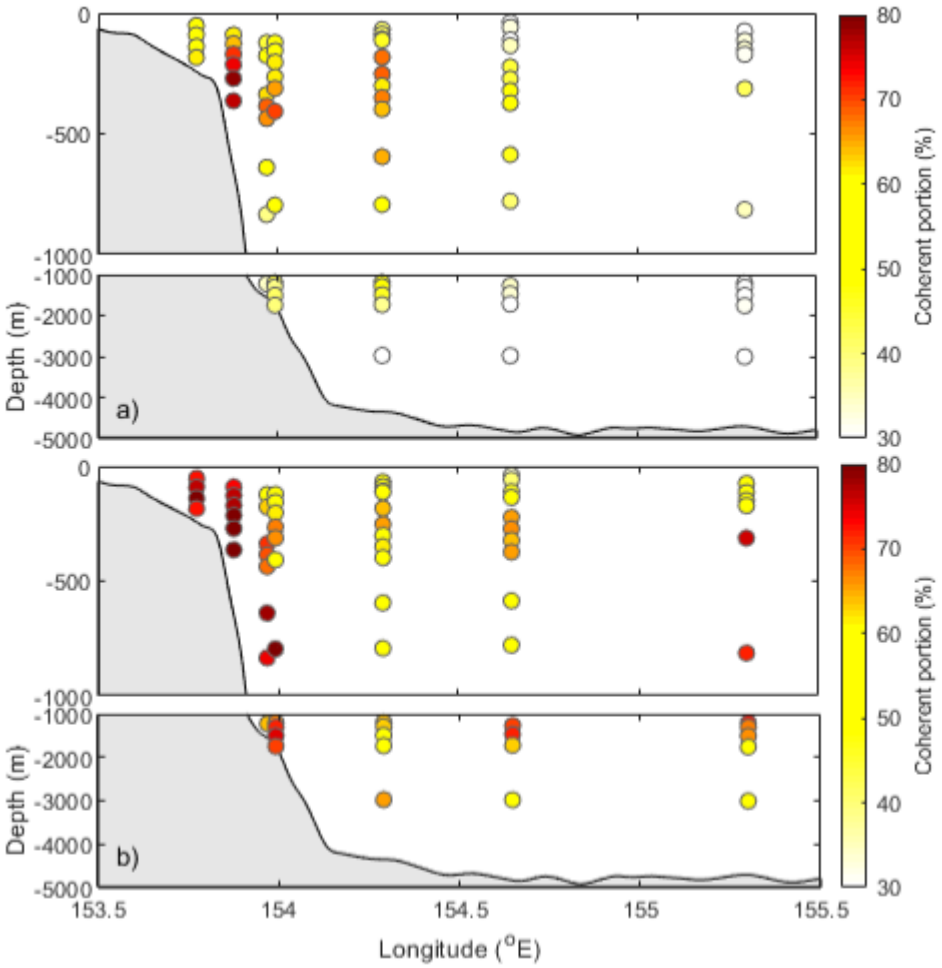

Figure 26: Cross-sections of the mean coherent portion using temperature anomaly filtered at **a)** diurnal and **b)** semidiurnal tidal band (May 2012 and Jun 2013 at SEQ200, SEQ400, EAC1, EAC2, EAC3, EAC4 and EAC5).

The coherent portion of the diurnal and semidiurnal frequencies is temporally variable above the continental slope (mooring SEQ400) near the surface (~ 90 m depth) and near the bottom (~ 364 m depth) (Figures 27a,c). The surface is less coherent, and more variable compared to the bottom of the continental slope in both frequencies (diurnal and semidiurnal).

The mean coherence of the diurnal frequency near the surface is 60%, and the standard deviation is 21% while the mean coherence near-bottom is 77% and the standard deviation is 13%. The correlation coefficient between the coherent portion and the spectral density above the continental slope is moderate (> 0.3 and < 0.7) and positive (Figures 27b,d). That means that when there is an increase in spectral density in diurnal frequency, there is an increase of the coherent portion of the internal tide. The correlation near-bottom of the continental slope (0.53) is higher than near the surface (0.42). The

highest spectral density (> 0.2° C^2/(1/day)) near the bottom of the continental slope occurs when the coherent portion is higher than 80% while the highest spectral energy densities near the surface occur when the coherent portion is less than 80%.

The coherent portion of the semidiurnal frequency above the continental slope is higher and less variable compared to the diurnal frequency (Figure 28a,c). The mean coherence near the surface (~90 m depth) is 73%, and the standard deviation is 19%. The time series of the coherent portion of the internal tide have a poor correlation with the spectral density of the internal tide. The mean coherence near-bottom (~364 m depth) is 90%, and the standard deviation is 10%. Most of the internal tides near the bottom of the continental slope are coherent (> 80%), and incoherencies occur when the spectral density is close to zero (Figure 28b,d) resulting in a lower correlation coefficient (0.34).

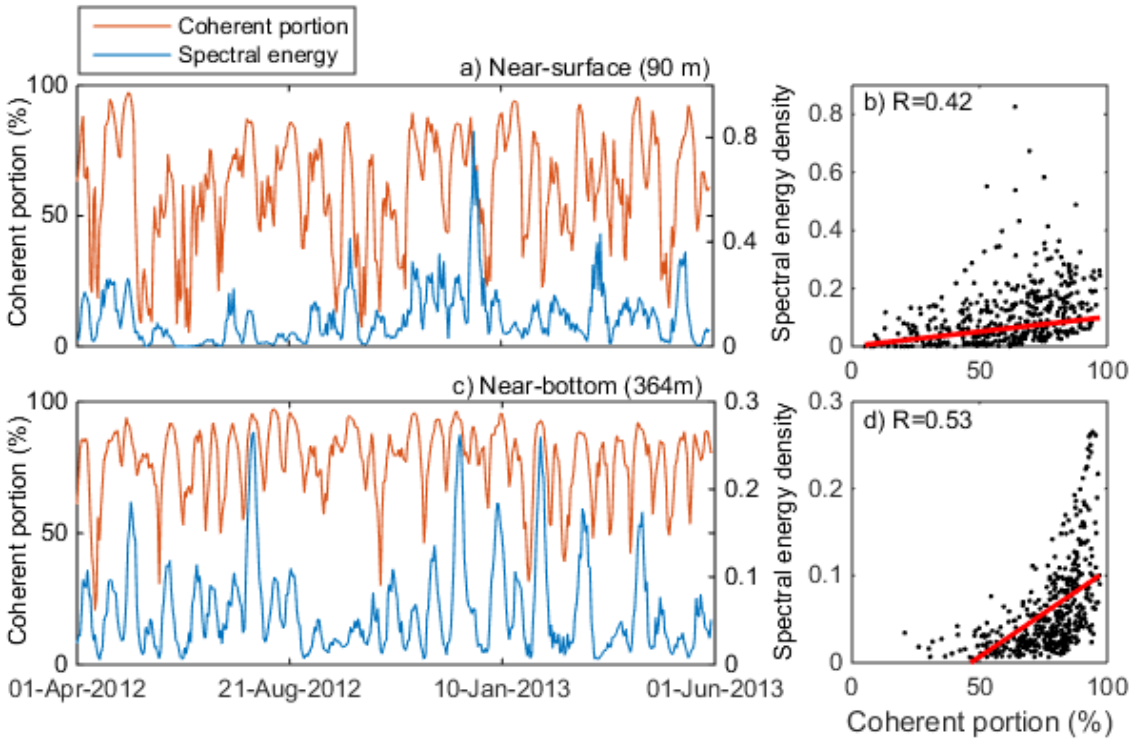

Figure 27: Time series of the coherent portion and the spectral density (° C^2/(1/day)) of the diurnal frequency using temperature anomaly **a)** near the surface (90 m) and **c)** near-bottom (364 m) above the continental slope (mooring SEQ400). Correlation coefficients between the coherent portion and the spectral density of the diurnal frequency and trend lines **b)** near the surface and **d)** near-bottom.

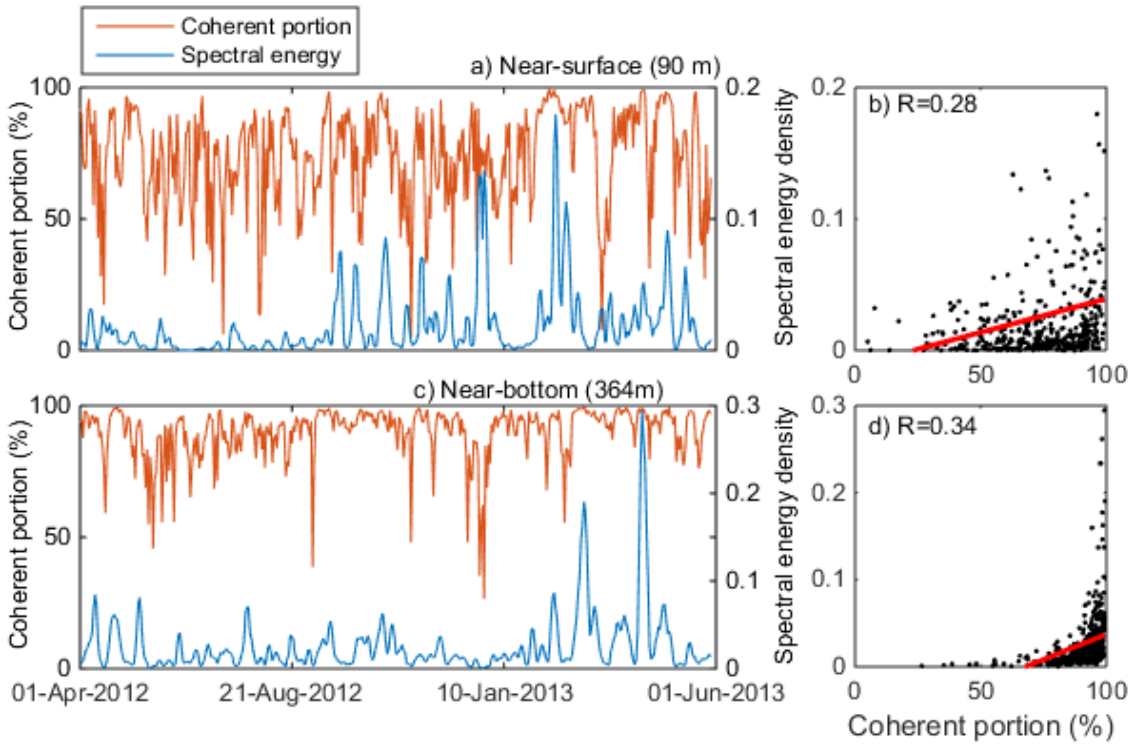

Figure 28: Time series of the coherent portion and the spectral density ($^oC^2$/(1/day)) of the semidiurnal frequency using temperature anomaly **a)** near the surface (90 m) and **c)** near-bottom (364 m) above the continental slope (mooring SEQ400). Correlation coefficients between the coherent portion and the spectral density of the diurnal frequency and trend lines **b)** near the surface and **d)** near-bottom.

3.3.4.2 Internal tide Amplitude

The time series of temperature anomaly filtered at diurnal and semidiurnal frequencies, near the bottom above the continental slope (364 m depth mooring SEQ400), were investigated to understand the origin of the internal tides that reach the bottom of the continental slope. While moored ADCP data is sometimes prone to contamination by mooring tilt, in this case, we investigate the velocities near the bottom (where tilt has no impact), using a near bottom, point source current meter which is not susceptible to mooring tilt.

The temperature anomaly of the diurnal frequency is in phase with the spring-neap cycle of the surface tide height (grey and black lines in Figure 29a). The temperature amplitude, however, is temporally variable compared to the tide height. The amplitude of the temperature anomaly at the diurnal period at the bottom (mooring SEQ400, 364 m) can reach higher than 1° C above the continental slope at some spring tides (Figure 29a).

The time series of the diurnal coherent portion (near-bottom, 364 m) varies between 30-97% over the analysed time (May 2012 to June 2013) with an average value of 77%. High coherence of up to 70% occurs when the amplitudes of temperature anomaly are high principally at the spring tide (Figure 29a). Greater incoherence (coherence lower than 50%) are observed in the time series. Some of them occur between spring and neap tides when the amplitude of the temperature anomaly due to the internal tide is low.

The semidiurnal variation of temperature at 364 m depth does not follow the spring-neap tide cycle of the barotropic tide (Figure 29b, compare the grey and black lines). Two periods of high semidiurnal energy stand out with amplitudes of temperature above 1°C, between the 3rd and the 10th of March 2013 and between the 12th and the 18th of April 2013 (Figure 29c). Both events occurred at the neap tide and the coherent portion is over 80%.

The phase of the barotropic tide, diurnal and semidiurnal, of all moorings (dashed line in Figure 30) is very close to the mooring SEQ400 described in section 2.2.1 (Table 6). The phase of the diurnal internal tide (K_1 and O_1) is similar (< 45^o) to the barotropic tide except for the mooring offshore EAC5. The phase of the semidiurnal internal tide, however, is different from the barotropic tide (> 45^o). Except for the mooring offshore EAC5 (constituent M_2) and mooring SEQ200 (constituent S_2).

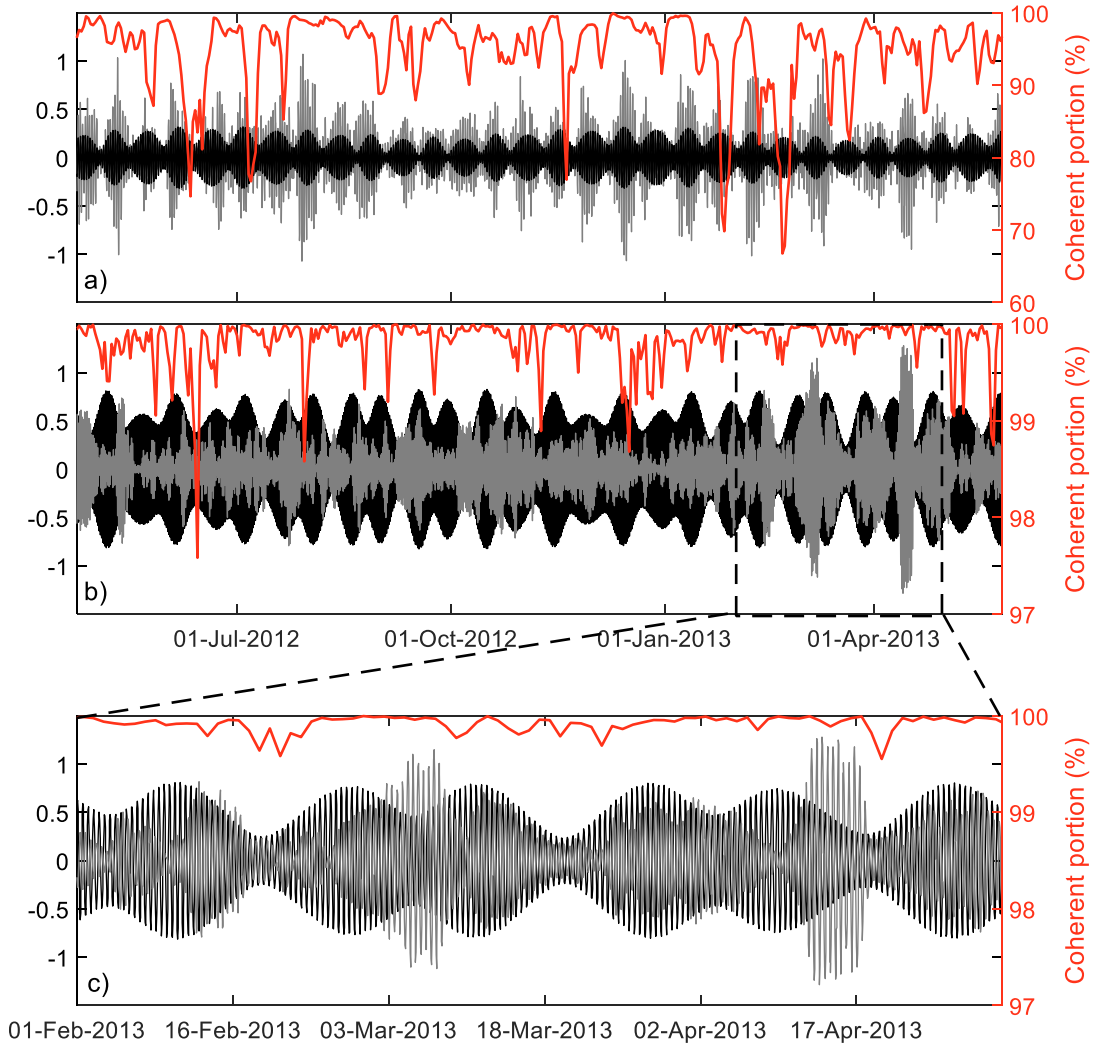

Figure 29: Barotropic tide height (in m, black), at SEQ400 location, estimated using TPXO at the diurnal and semidiurnal frequencies. Time series of temperature anomaly at 364 m depth (at SEQ400, grey) and the coherent portion (as a percentage) calculated using harmonics **a)** K_1 and O_1; **b)** M_2 and S_2 of the temperature anomaly time series (364 m). **c)** Zoom between 01 February 2013 and 01 May 2013 using harmonics M_2 and S_2.

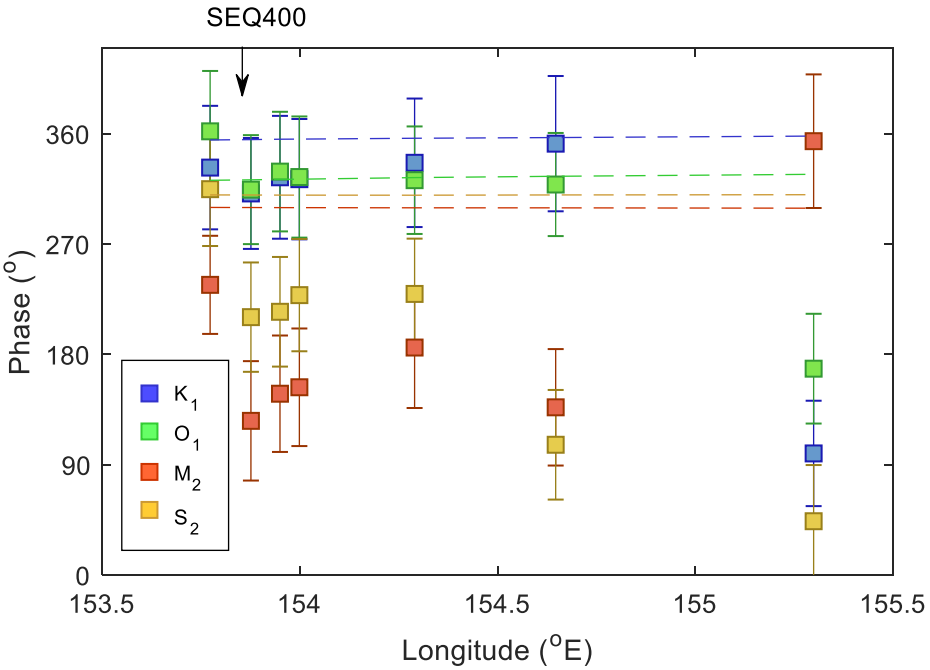

Figure 30: Barotropic (dashed line) and mean and standard deviation baroclinic (squares) phases of the tide constituents K_1 (blue), O_1 (green), M_2 (red) and S_2 (yellow) at SEQ200 (184 m), SEQ400 (364 m), EAC1 (337 m), EAC2 (407 m), EAC3 (399 m), EAC4 (373 m) and EAC5 (312 m) respectively.

3.3.4.2 Internal Tide Sea Surface Amplitude

To further identify the origin of the internal tides, the amplitude of the internal tide estimated in the surface of the ocean for the harmonics (K_1, O_1, M_2 and S_2) using altimetry data is shown in Figure 31. High amplitude (> 0.5 cm) of the diurnal harmonics K_1 and O_1 is observed between Latitude 23°S and 27°S (Figure 31a,b). The highest amplitude (~4 cm) is observed in the semidiurnal internal tide (harmonic M_2) close to New Caledonia and a track (in-phase, not shown) of the high amplitude internal tide is observed towards the study area (Figure 31c). The amplitude of the internal tide, harmonic S_2, is lower (<1 cm) compared to the harmonic M_2 and has a high amplitude pathway propagating towards the study area (Figure 31d).

3.3.4.3 Criticality

The time-mean criticality (between May 2012 and June 2013) is calculated for the diurnal and semidiurnal internal tide using the model output described in Section 2.5. The criticality is highest above the continental slope (reaching a factor of 15) at the study area, between 400 and 2000 m depth, and at

the seamounts offshore (higher than a factor of 15) that are more than 4000 m high (Figure 32a), i.e., where the water is less than 1000 m depth.

The criticality calculated for the semidiurnal internal tide is lower than for the diurnal (Figure 32b). It reaches a factor of 7 above the continental slope at the study area (near the mooring SEQ400). The criticality is high also north and south of the study area (latitudes 26.5^{o}S and 28.5^{o}S). Where the continental slope is even steeper, and high criticality is observed in the seamounts offshore. The results suggest that the internal tide is likely to be generated locally at the study area above the continental slope.

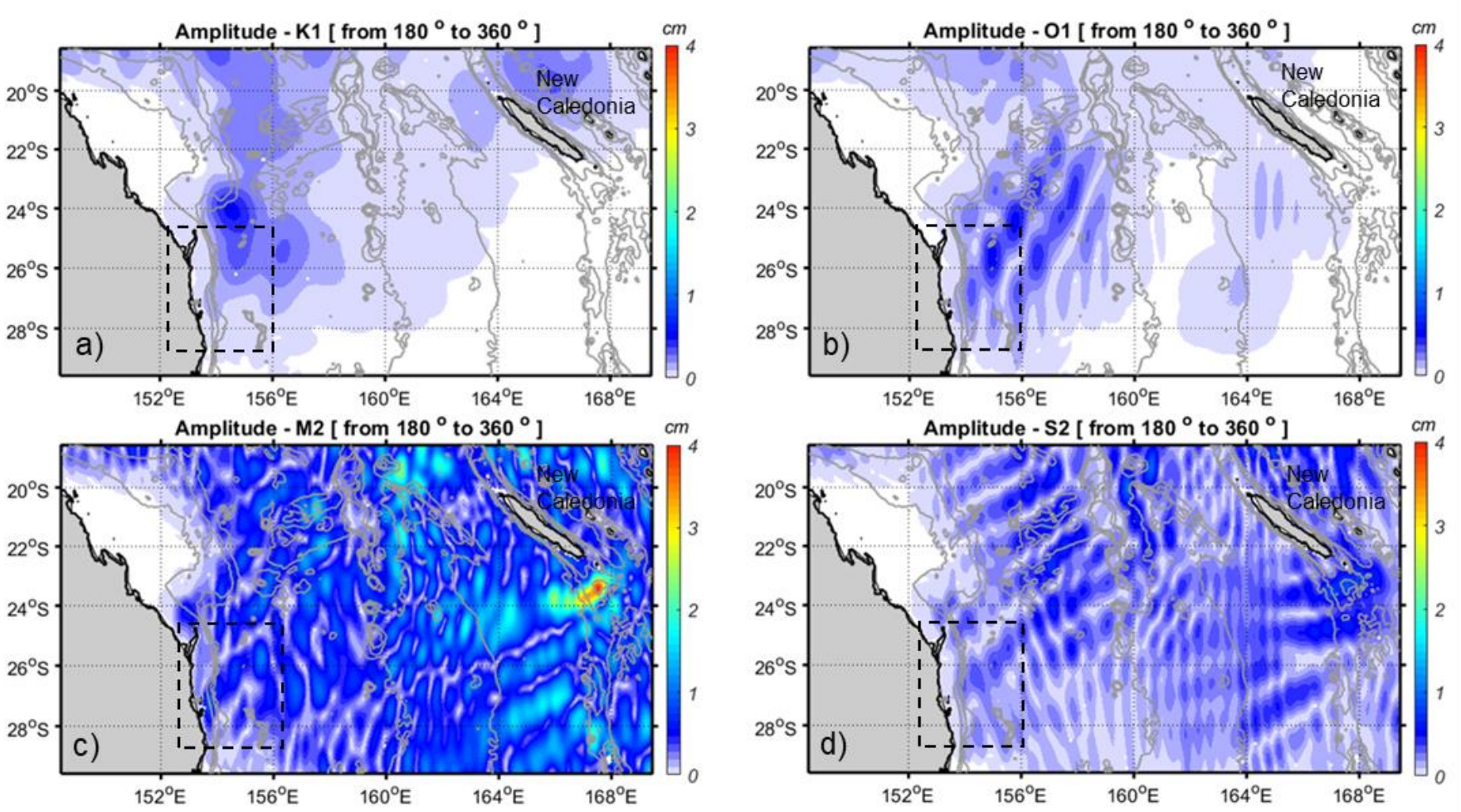

Figure 31: Baroclinic sea surface amplitude induced by internal tides. Four harmonics are analysed **a)** K_1, **b)** O_1, **c)** M_2 and **d)** S_2. The dashed line delineates the study area. The data is from an altimetry product (HRET) provided by Zaron (2019).

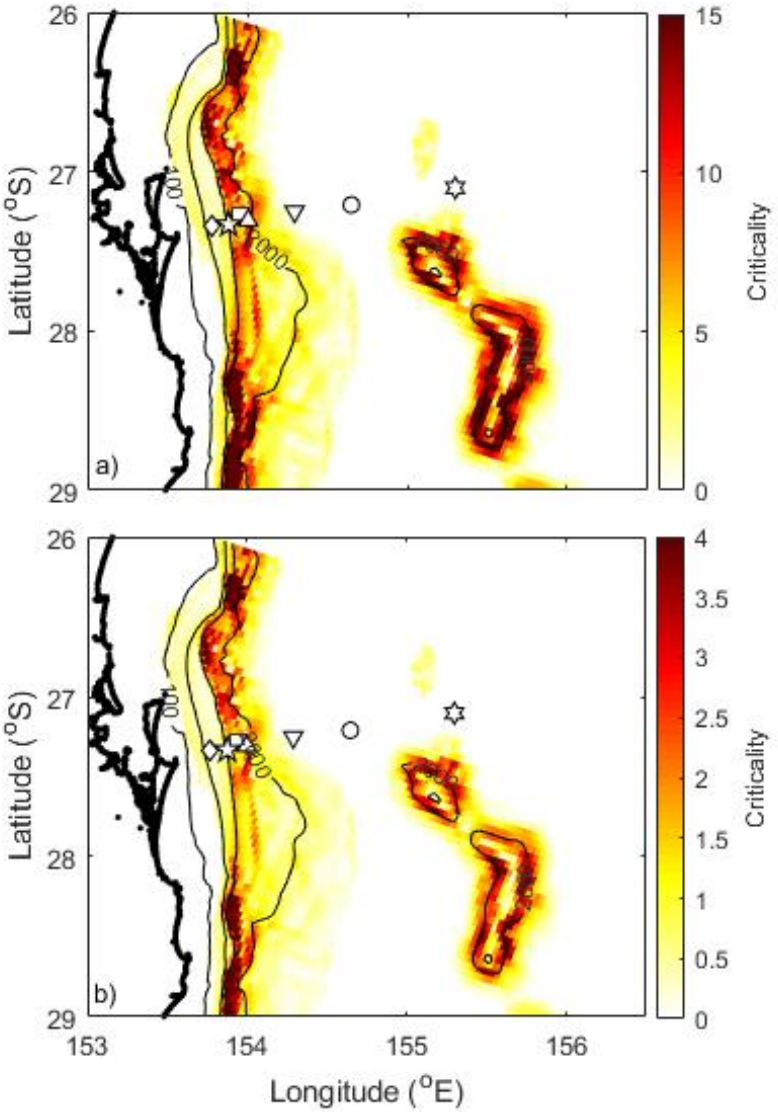

Figure 32: Spatial map showing the time-mean criticality in the region for the **a)** diurnal and **b)** semidiurnal tidal band. The contour lines show the 100, 200, 400, 2000 m isobaths. This was calculated using model output, for the same period of the observed data, from EAC-ROMS model output of the region (Kerry et al. 2016).

3.3.4.4 Drivers of the Near-Inertial Waves

The study area is in the diurnal critical latitude (27°S) which the frequency of the inertial wave is close to the diurnal internal tides. The near-inertial waves have several generation mechanisms, the wind blowing on the ocean surface, nonlinear wave-wave interactions, lee-wave formation by geostrophic flow over seafloor topography, and spontaneous emission through loss of balance. Wind stress is analysed to infer about the near-inertial wave generation in the study site.

The mean of the wind stress between May 2012 and Jun 2013 is 0.003 N m^{-2}, the standard deviation is 0.006 and the maximum is 0.08 N m^{-2} as observed on 2nd Nov 2012. Stronger wind stress (> 0.15 N m^{-2}) are observed between 5th Sep 2012 and 17th Nov (dashed line in Figure 33). The wind stress is correlated to the spectral density (SD) of temperature anomaly at diurnal frequency. The water column near-surface (90 m) and near-bottom (364 m) above the continental slope (isobath of 400 m) is used for the comparison. Most of the peaks observed in the time series of wind stress are not related to the peaks of SD in diurnal frequency (Figure 33a,c). The correlation between the wind stress and SD (April 2012 and June 2013) is close to zero in both, the water column near the surface (90 m) and near the bottom (364 m) above the continental slope (Figure 33b,d).

Two peaks of stronger wind stress (> 0.15 N m^{-2}) occurs at the same time as peaks on SD (diurnal frequency) near the surface (90 m), at 6th Sep 2012 and 14th Nov 2012 (Arrows Figure 33a) and, can contribute for the SD at diurnal frequency. However, peaks of the SD near the bottom (364 m), above the continental slope (isobath of 400 m), are lower (< 0.1 $^{o}C^{2}$/(1/day)) during the stronger wind stress, between 5th Sep 2012 and 17th Nov (dashed line), compared to the other time analysed between 1st Apr 2012 and 1st June 2013 (Figure 33c).

A typical frequency spectrum of velocity at the near-inertial frequency has an elevated counter-clockwise kinetic energy. The rotatory spectrum density is analysed monthly using the near-bottom velocity in the mooring SEQ400. The counter-clockwise kinetic energy in the near-inertial frequency (26 hrs) is elevated and higher than clockwise kinetic energy in the months (September to January 2012). This elevation of the counter-clockwise spectrum is observed in the periods of strong winds stress, between September and November 2012 (Figure 34). However, the counter-clockwise energy spectrum is close to the clockwise during the months May, June, July and August 2012 and February, March, April, and May 2013, suggesting that the near-inertial wave has less influence on the diurnal frequency during these months.

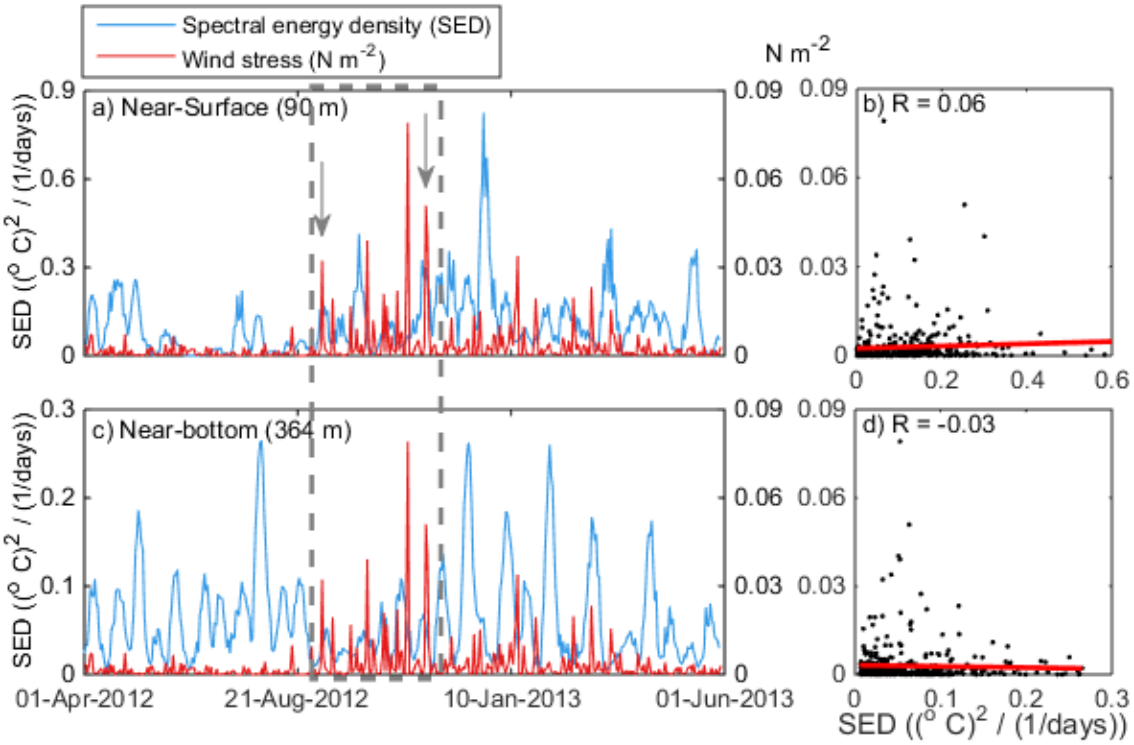

Figure 33: Time series of the wind stress (N m^{-2}) and the spectral density ($°C^2$/(1/day)) of the diurnal frequency using temperature anomaly **a)** near the surface (90 m) and **c)** near-bottom (364 m) of the continental slope (mooring SEQ400). Correlation coefficients between the wind stress and the spectral density of the diurnal frequency (between 1st April 2012 and 1st June 2013) and trend lines **b)** near the surface and **d)** near-bottom.

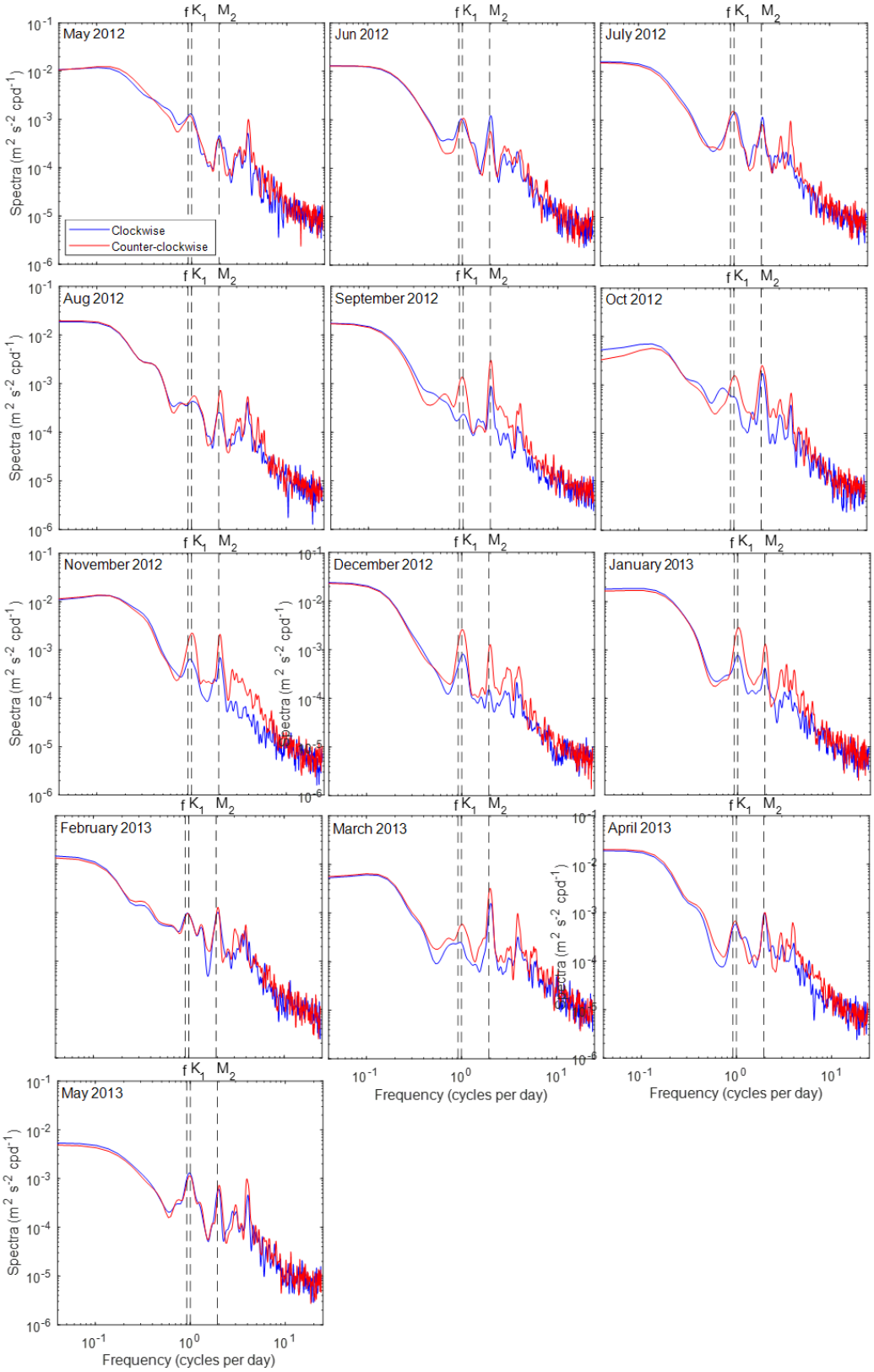

Figure 34: Monthly rotary velocity spectrum at mooring SEQ400 (364 m). Blue and red represent clockwise and counter-clockwise motions, respectively. The harmonic constituents, K_1 and M_2, and near-inertial frequency (f) are plotted with a grey dashed line.

3.4 Discussion

We use 13 months of temperature, salinity, and velocity data from the EAC mooring array to characterise the internal tides. The mean, variability and spatial distribution of the internal tide energy were analysed. We also explore the origin (local or remote) of the diurnal and semidiurnal internal tides in our study region. We compare the internal tide with the barotropic tide to observe cyclicity in the internal tide (neap-spring tide) and phase. We calculate the coherent (stationary) portion of the internal tide. We have access to model output to analyse the mean vertical structure of the ocean in the study area and the criticality to have an insight on where the internal tides would likely to be generated.

3.4.1 Characterising the Internal Tide

The results show that the main harmonic components of the internal tide above the continental slope in the study area are the diurnal frequencies K_1 and O_1, and semidiurnal frequencies M_2 and S_2 (Figure 14). The time series of the temperature and velocities, filtered at diurnal and semidiurnal frequencies, show that the internal tides are temporally variable (Figures 15 and 16). The variability of the internal tide is also observed in the cross-sections of the root mean squared variance of the velocities (Figures 19 and 21) and is higher (> 0.05 m s^{-1}) above the continental slope. The spectral density of the internal tide is energetic throughout the water column above 500 m depth and is higher above the continental slope (Figure 25). A similar pattern is observed with the root mean squared of the diurnal and semidiurnal velocities (Figures 18 and 20).

The mean baroclinic energy flux is 0.34 kW m^{-1} for diurnal and 0.06 kW m^{-1} for semidiurnal in the mooring EAC1 (Table 1). These mean values are lower than the widely studied, energetic internal tide regions. For example, at the Luzon Strait and the Hawaiian Ridge there is an energetic baroclinic flux (mean >25 kW m^{-1}) generated by strong barotropic tides flowing above steep topography (Kerry et al. 2014; Rudnick et al. 2003). However, in the EAC, the depth-integrated baroclinic flux is highly variable and can reach more than 10 kW m^{-1} above the continental slope. The first mode carries the bulk of the energy flux, about 80–85% of the total over modes 1–3 (Alford et al. 2017).

3.4.2 Origin of the Diurnal Internal Tide

Internal tide generation is possible at the continental slope because of steep topography (Gayen and Sarkar 2011; Martini et al. 2011). The internal tide in the surface is less coherent compared to the bottom (Figures 26 and 27) and is more susceptible to the influence of the near-inertial wave. The near-

bottom variation of the temperature anomaly (diurnal band) above the continental slope is outstanding in the study area (>1^{o} C). Higher peaks of temperature and velocities near the bottom are observed compared to the water column above. This is important because the internal tides play an important role in mixing the deep ocean (Alford 2010; Wang et al. 2016).

Our results suggest that the peaks of the diurnal internal tides are locally generated internal tides reaching the bottom of the continental slope because 1: They exhibit a high coherent portion near the bottom, with means greater than 70%, (Figures 26 and 28a); 2: The diurnal signals that reach near the bottom of the continental slope have a pronounced tidal cycle (Figure 28a), with the phase of the diurnal internal tides (K_1 and O_1) close to the phase of the local barotropic tide (Figure 29) and 3: The high criticality above the continental slope, as observed in the study area (Figure 30a), suggest that diurnal internal tides can be locally generated (Duda et al. 2004; Lim et al. 2010; Rayson et al. 2011)

Due to the fact that the study area is at the critical latitude, the incoherent (non-stationary) portion of the diurnal frequency can be the influence of the near-inertial wave. The coherent portion of the internal tide is lower offshore suggesting higher influence of the near-inertial waves or shoaling internal tides. The coherent portion above the continental slope is variable and can be due to the influence of the near-inertial wave reaching the bottom of the continental slope.

Global modelling studies do not resolve the study area well due to the proximity to the coast and strong hydrodynamic energy that affects the local stratification. Hot spots of diurnal internal tide generation are not observed offshore of eastern Australia, near the study area, and the amplitude of the internal tide is lower than 0.25 cm (Shriver et al. 2012). Alford et al. (2017) analysed the internal tide in the study area using velocity data from the mooring array. They attributed most of the diurnal baroclinic flux to the near-inertial waves. However, this study shows that the internal tides are variable and can have a high coherent portion at the diurnal frequency principally near the bottom above the continental slope (suggesting local generation). Moreover, the correlation of the diurnal spectral density with the wind stress is close to zero (Figure 33b) and the period of strong wind stress does not correspond with an increase in energy (Figure 33a). A typical frequency spectrum of velocity at the near-inertial frequency has an elevated counter-clockwise kinetic energy in the southern hemisphere (Alford et al. 2017) however the clockwise kinetic energy is close to the counter-clockwise (Figure 34) in months May to August 2012 and February to May 2013 indicating less influence of the near-inertial waves during these periods.

Hence, we are confident that our results support the idea that the diurnal internal tide above the continental slope is, most of the time, locally generated. We explore the mechanism of generation and variability of the diurnal internal tide more fully in Chapters 4 and 5.

3.4.3 Origin of the Semidiurnal Internal Tide

High coherent portion of the semidiurnal tide is observed in the moorings above the continental slope (Figure 27c) but does not correspond to the local spring-neap cycle (Figure 28b). The mean phase of the semidiurnal constituents (125^o and 210^o for M_2 and S_2 respectively) are quite different from the barotropic tidal phases, 309^o and 299^o for M_2 and S_2 respectively (Figure 29). While the semidiurnal internal tide exhibits a high coherent portion most of the time, the internal tides are not in phase with the local barotropic tide suggesting remote generation. High coherence indicates that, over the 3-day windows, most of the semidiurnal variability can be explained by the harmonics suggesting that the remotely generated internal tides are not significantly modulated on time scales of less than 3 days. High incoherence of the semidiurnal internal tide, close to the bottom, tends to occur when the amplitude of the temperature of the internal tide is small. This is expected as internal tides become less coherent as they are scattered and lose energy when they travel for remote sources. The semidiurnal internal tides constitute a significant percentage of the total velocity variance in the study area. We show that the semidiurnal internal tide in this region is remote. Alford et al. (2017) suggest that it is originating from New Caledonia and the Solomon Islands. Global models and satellites observations show hot spots of semidiurnal generation in the southwest Pacific including New Caledonia and Solomon Islands (Arbic et al. 2010; Shriver et al. 2012; Zhao et al. 2016). Tracks of the internal tide are observed propagating toward to eastern Australia coast from Papua New Guinea (Arbic et al. 2010; Shriver et al. 2012).

We showed that there were two peaks of the temperature amplitude of the semidiurnal internal tide, between March 3rd and 10th, and between April 12th and 18th, that was outstanding in the study area above the continental slope (Figure 28b). The high peaks occur at neap tide when the internal tide generation is expected to be lower. This is characteristic of the remotely generated internal tide that overwhelms local internal tide during neap tides as seen in Nash et al. (2012) and Martini et al. (2011). The spectral density of the near-bottom internal tides is four times higher when compared to the mean for the entire period analysed (May 2012 and June 2013), suggesting that the internal tides, at these periods, were remotely generated.

The large difference between the coherent portion estimated at the present study and the coherent portion estimated by Alford et al. (2017) is related to the fact that computing the coherent portion of the internal tide using the entire time series (431 days) will result in a lower coherent portion (20 %) even if the internal tides are locally generated, (i.e., phase invariant). It occurs due to variability in the

amplitude of the local internal tide due to changing stratification (Figure 25) and is comparable to the Alford et al. (2017) results (14 % of coherence).

Despite the high coherent portion of the semidiurnal internal tide, the study area must be dominated by two regimes, locally and remotely generated. Comparing the time series of the barotropic tide with the internal tide is possible to observe peaks of the internal tide at neap tide, characteristics of remote internal tides (Figure 28b). The great variance in the baroclinic flux direction reinforces the idea of different sources of the semidiurnal internal tide (Figure 22). The origin of the remote internal tide is principally from New Caledonia (Figure 31). Due to the high peaks of the semidiurnal internal tide energy near-bottom of the continental slope and the relevance of the internal tides on mixing the bottom of the ocean, more details of the remote internal tides are suggested for further research.

3.5 Conclusion

In conclusion, off eastern Australia (27ºS) the diurnal internal tides are more energetic than the semidiurnal. The mean diurnal depth-integrated energy fluxes reach 4.3 kW m^{-1} compared to 0.51 kW m^{-1} for the semidiurnal (mooring SEQ400).

The spectral density calculated from the temperature time series shows that the energy of the internal tides is variable at the study area and is higher above the continental slope compared to offshore with the peak of the spectral density reaching 1.6° C^2/(1/day) in the mooring SEQ400.

Observations show that the diurnal internal tides have a pronounced spring-neap tide cycle and a high coherent portion (> 70%) near the bottom of the continental slope indicating generation above the continental slope. The criticality reinforces the idea of the local generation of the internal tides above the continental slope at the study area.

The semidiurnal internal tides also have a high coherent portion and are both remotely and locally generated. The peaks of the internal tide at neap tide (suggesting remote source) seems to be more sporadic and energetic (baroclinic flux reaching 0.51 kW m^{-1}, mooring SEQ400) compared to the mean of the entire period analysed (0.04 kW m^{-1}).

The sensitivity analysis of the coherent portion of the semidiurnal internal tide shows that the coherent portion is temporally variable and lower coherence can be related to the time window used to compute the analysis. The best window to use in this case Is the 3/6 day window for diurnal/semidiurnal.

Chapter 4: Modulation of the Diurnal Internal Tide Above the Continental Slope off Eastern Australia

4.1 Introduction

The generation of internal tides above the continental slope is driven by barotropic tide forcing and background stratification (Townsend 1965; Baines 1982; Craig 1987; Holloway and Merrifield 1999; Kelly and Nash 2010). In the continental shelf and slope regions, many features can change the background stratification such as boundary currents and eddies (mesoscale and sub-mesoscale). Frontal cyclonic eddies are one such eddy that can form a strong density gradient at the interface with the western boundary current (WBC). Originating from instabilities of the mean current, these eddies are generated on the inshore edge of WBCs and propagate poleward independently of the wind, (Lee, 1975). However, wind stress can influence their growth, resulting in large cold-core eddies through intense shear (Schaeffer et al. 2017).

Cyclonic frontal eddies are observed in the study area between Fraser (25^{o}S) and Moreton (27^{o}S) islands, moving to the south (Ribbe and Brieva 2016; Ismail et al. 2017; Roughan et al. 2017). They are very frequent at 30^{o}S, with 40 frontal eddies observed in a 12-month period between 2012 and 2013, and their diameter of about 30 km (Schaeffer et al. 2017).

In this chapter, we analyse the variability of the diurnal internal tides above the continental slope and the influence of these small frontal cyclonic eddies on the local stratification. We compare the time series of the diurnal temperature anomalies with the time series of the buoyancy frequency (N^2), to infer the stratification, and Eddy Kinetic Energy (EKE), to quantify the presence of the eddies. We also compare the time series of the diurnal temperature anomaly near the bottom of the continental slope with the time series of the sea surface height from the barotropic tide to analyse the variability due to the spring-neap cycle.

4.2 Methods

During the 13 months of observational data analysed (the mooring deployment), we identify 12 times where the internal tides appear to be intensified (as shown by the peaks in buoyancy frequency). For all 12 time periods, a cyclonic eddy is observed in the study area simultaneously with the internal tide intensification near the bottom of the continental slope. In this chapter, we choose one scenario of intense internal tides coincident with the passage of a frontal eddy to analyse spatially using sea surface temperature and salinity, sea surface height anomaly and vertical cross-sections of buoyancy frequency to elucidate the main mechanisms that modulate the internal tide in the study area.

4.2.1 Internal Tide Intensification

We use in situ data obtained from the mooring array described in Section 2.2 to analyse the internal tide intensity. The time series of the spectral density (SD) calculated using the temperature time series filtered at the diurnal frequency (T_d) is used to identify the peaks in the intensity of the diurnal internal tide (Figure 35). The time series of the SD of temperature at diurnal frequency is calculated for overlapping time windows over the 13-month period (1st May 2012 to 1st June 2013) for which data is available. The time windows are 6 days long, overlapping by 5 days. We choose these time window lengths as they are long enough to extract the harmonics to perform the analysis described in Chapter 3 (Section 3.2.2) and we assume the subtidal circulation (that is influencing the stratification) to vary little over these periods since the cyclonic eddies can live for 1-4 weeks (Schaeffer et al. 2017).

Spectral density higher than 0.15^o C^2/(1/days) near the bottom of the continental slope was used as a metric to identify 'intensification' of the diurnal internal tide. We focus on the internal tide examples near the bottom (364 m depth) at the mooring SEQ400, which is located over the continental slope (Figures 4, 5, Chapter 2) in ~ 400m of water.

4.2.2 Stratification

We calculate the buoyancy frequency squared (N^2) to infer the stratification and analyse the correlations between the spectral density of the internal tide and the background stratification. We use time series of temperature and salinity measured at two depths (270 m and 364 m) over the 400 m isobath towards the bottom of the continental slope at SEQ400 to calculate N^2. Firstly, we detide the time series using a

low-pass (cut off 30 h) Butterworth filter to exclude the influence of the tidal frequencies (as per Chapter 3). We use the detided temperature and salinity data to calculate the density (ρ). N^2 is given by equation 13 (Chapter 3).

4.2.3 Cyclonic Eddy Activity

To investigate the cyclonic eddy activity in the region the eddy kinetic energy (EKE) is calculated from the measured velocity data obtained at the mooring (SEQ400 400 m) to quantify the influence of the eddies. We then compare EKE to the spectral density of the diurnal internal tide near the bottom of the continental slope. We detide the observed zonal and meridional velocities (mooring SEQ400) using a low-pass filter (cut off 30 h), described in Chapter 2 Section 2.2.2, to exclude the influence of the tidal frequencies. The detided horizontal velocity (u_{dt} and v_{dt}) are used to compute the EKE (Equation below).

$$\mathrm{EKE} = \frac{1}{2}(\mathrm{u'^2} + \mathrm{v'^2}), \tag{28}$$

where u' and v' are low pass filtered velocity anomalies, computed for the period between May 2012 and June 2013 (mooring SEQ400).

We access model output from the EAC reanalysis (Kerry et al. 2016; Kerry et al. 2020) described in Chapter 2 (Section 2.5) to characterise the cyclonic eddies. We analyse maps and cross-sections of temperature, salinity, density, stratification and velocity from the model. We also analyse maps of the SSHa (from the EAC-ROMS model) to infer the size of the eddies.

4.3 Results

4.3.1 Stratification Above the Continental Slope

The spectral density (SD) of temperature (Figure 35a) is temporally variable over the 13-month period, with a mean of 0.06° C^2/(1/days) and standard deviation of 0.05 ° C^2/(1/days), and peaks can reach more than 0.2° C^2/(1/days). The time series of the SD is compared to the stratification (N^2) close to the bottom (between 270 and 364 m depth) at the continental slope over the 400 m isobath (mooring SEQ400, Figure 35b). The N^2 was variable at the study area over the 13-month period ranging from 9.63 x 10^{-6} s^{-2} to 1.1 x 10^{-4} s^{-2} near the bottom of the continental slope with a mean of 3.51 x 10^{-5} s^{-2} and standard deviation of 1.5 x 10^{-5} s^{-2} (Figure 35b).

The peaks in stratification (N^2 > 6.7 x 10^{-5} s^{-2}) near the bottom of the continental slope are shown in Figure 35b (arrows labelled S1-S4). They correspond to an intensification of the SD of the diurnal internal tide (Figure 35a) of magnitude higher than 1.5° C^2/(1/days). The highest peaks of stratification that occurred at the dates 23/07/2012, 06/02/2013, 07/03/2013 and 14/04/2013 (scenarios S1, S2, S3 and S4 in Figure 35b) are analysed to understand what is increasing the stratification near the bottom of the continental slope.

Not all peaks are related to the intensification of the stratification near the bottom of the continental slope as an example on 12/12/2012 and 07/01/2013. The correlation between the stratification (N^2) and SD for the 13-months period (01/05/2012-01/06/2013) is 0.2. However, higher positive correlations are observed between N^2 and the SD for specific time periods. The 3-month period, between 01/07/2012 and 01/10/2012, that includes the first scenario (S1) with high N^2 (> 6 x 10^{-5} s^{-2}) is well correlated with SD (correlation coefficient of 0.63, Figure 35c). Peaks are also observed between 01/02/2013 and 18/05/2013, which include scenarios S2, S3 and S4 with a correlation of 0.6 (Figure35d). The strongest correlation (0.79) is observed for one month period, which includes S3, between 21/02/2013 and 21/03/2013 (Figure 35e), therefore we focus on scenario S3.

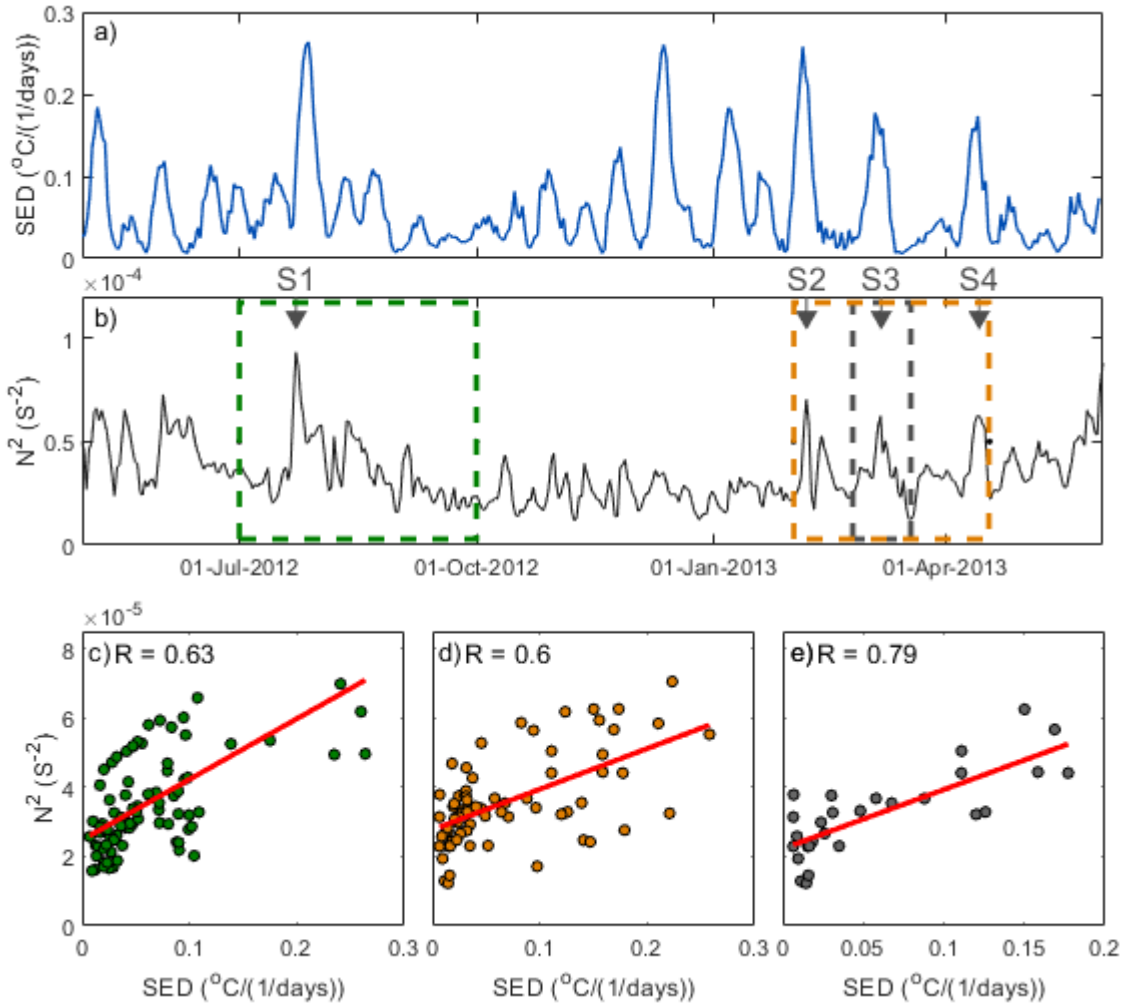

Figure 35: a) Time series of diurnal spectral density (SD) of temperature between 01 May 2012 and 01 June 2013, at the SEQ400 mooring at 364 m depth. **b)** Buoyancy frequency squared (N^2), between 270 and 364 m depth at the mooring SEQ400. The arrows (S1, S2, S3 and S4) indicate the peaks in stratification (23/07/2012, 06/02/2013, 07/03/2013 and 14/04/2013) that precede intensification of the internal tide. Correlation between the buoyancy frequency squared and SD during the period between **c)** 01/07/2012 and 01/10/2012 green dashed box in b; **d)** 01/02/2013 and 18/05/2013 orange dashed box in b, and **e)** 21/02/2013 and 21/03/2013 (black dashed box in b). The red line is the trend line.

4.3.2 Modulation of the Internal Tide

Visual inspection of sea surface (temperature, salinity, and density) shows that cyclonic eddies are a common dynamic feature that changes the stratification in the study area. During the period between May 2012 to Jun 2013, twelve cyclonic eddies passed through the study area at spring tide and could be identified using satellite data (Figure 37). The passage of the cyclonic eddies (red arrows in Figure 36) matches with greater temperature anomalies (> 0.5° C) of the diurnal internal tide.

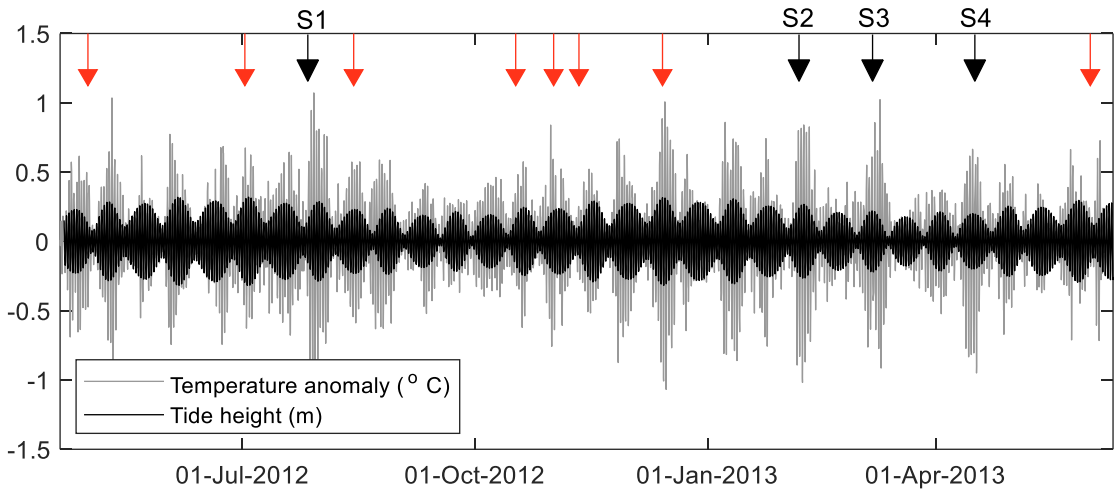

Figure 36: Diurnal barotropic tide height (in m, black) at SEQ400 estimated using TPXO and time series of temperature anomaly (diurnal frequency) at 364 m depth (at SEQ400, grey). The arrows indicate the dates of the passage of the frontal eddies identified using SSTs (Figure 37). The black arrows are the dates S1-S4 showed in Figure 35.

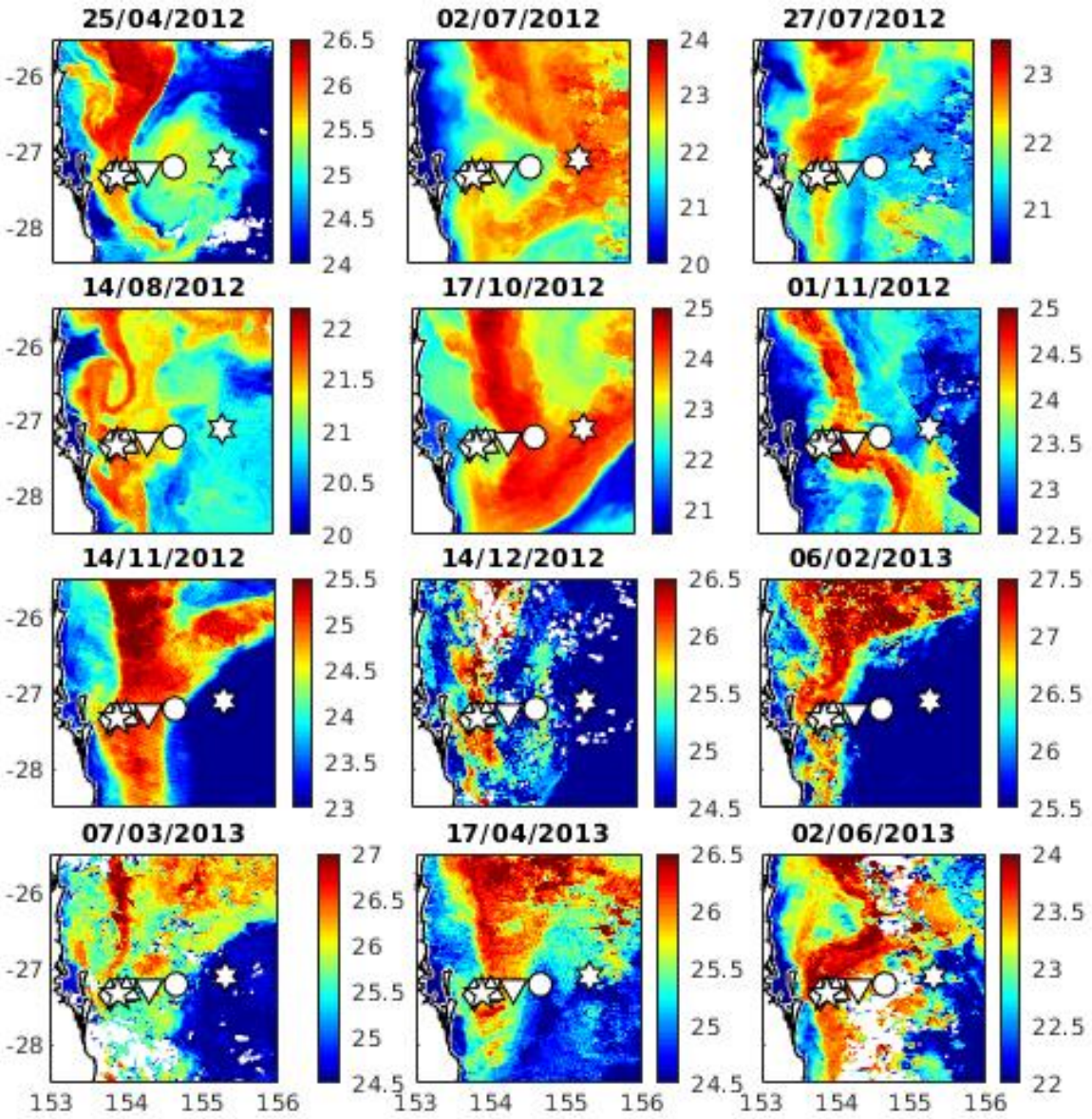

Figure 37: Sea surface temperature (°C) of the 12 frontal eddies observed using satellite data for the dates **a)** 25/04/2012, **b)** 02/07/2012 (explored in Chapter 5), **c)** 27/07/2012, **d)** 14/08/2012, **e)** 17/10,2012, **f)** 01/11/2012, **g)** 14/11,2012, **h)** 14/12/2012, **i)** 06/02/2013, **j)** 07/03/2013, **k)** 17/04/2013 and **l)** 02/06/2013.

Each peak of high stratification near the bottom (arrows in Figure 35b) was associated with the passage of a cyclonic eddy across the mooring array. The moment of the highest peak of the stratification near the bottom of the continental slope (Figure 35a, scenarios S1 to S4) can be observed in Figure 38 when the frontal eddies reach the study area. The surface height anomaly is enclosed at the latitude ~ 26.5^{o}S near the coast and there is a horizontal gradient of density at the leading edge of the eddy (Latitude ~ 27.3^{o}S).

To investigate the relationship between cyclonic eddies and intensification of the internal tide further, we present a case study of one discrete scenario characterised by the passage of a cyclonic eddy between 4th and 10th of March 2013 (Scenario S3 in Figures 35b, 38c). The peak of the stratification near the bottom of the continental slope occurs on the 7th of March 2013 during the passage of a frontal eddy where the highest horizontal gradient of temperature and salinity is observed in the data assimilating model (Figure 39). The eddy extends from the latitudes 26^{o}S to 27.2^{o}S (north / upstream of the mooring array), and from the shelf to 154^{o}E and is approximately 30 km wide (Figure 39). The surface temperature varies between 25.8° C and 26.4° C (Figure 39a) and salinity varies from 35.2 to 35.5 at the surface (Figure 39b). The eddy propagates to the south and the leading edge of the eddy (south side) is warmer and less salty compared to the water masses south of the eddy, creating a horizontal gradient of temperature and salinity observed in the mooring data.

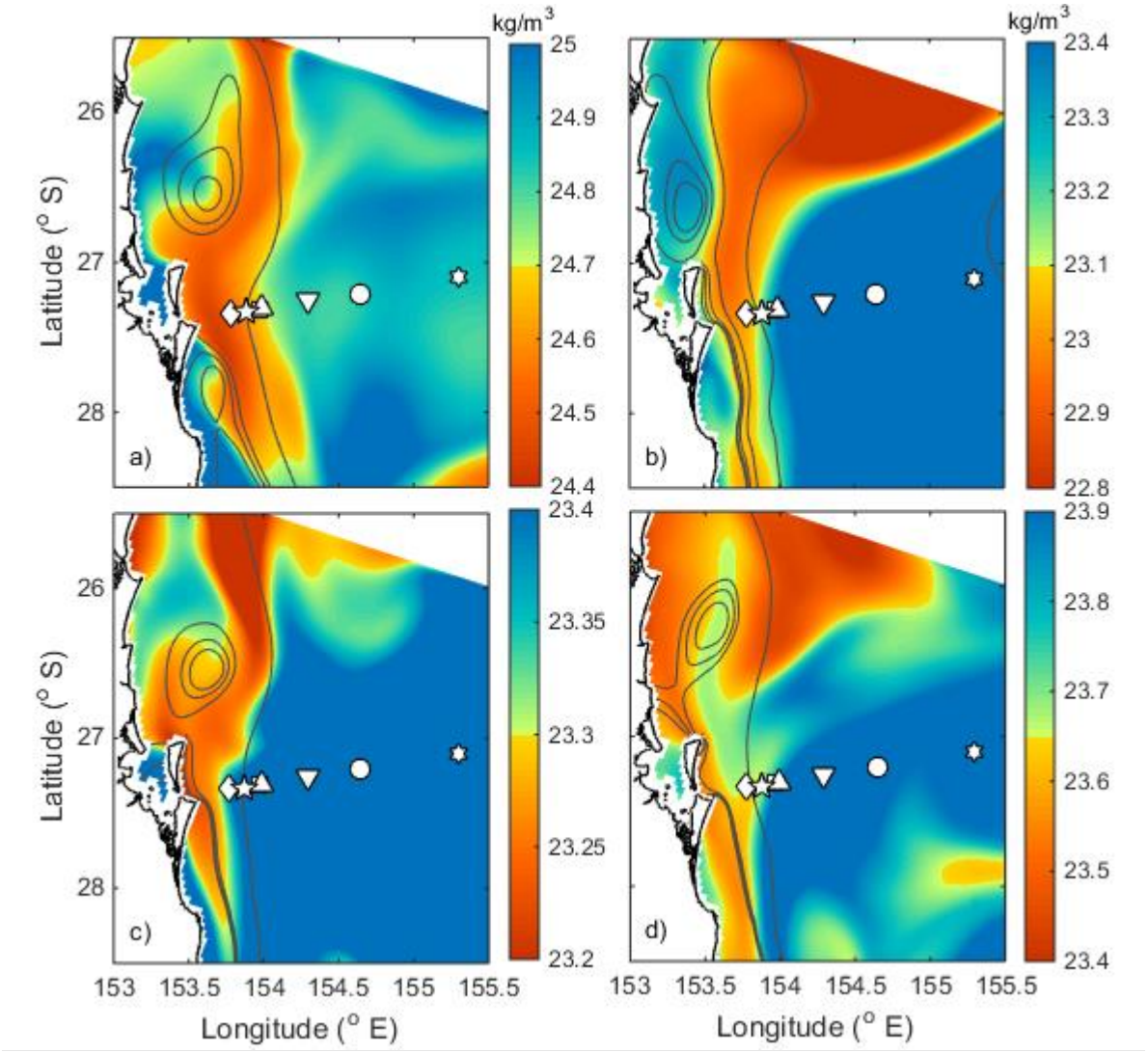

Figure 38: Sea surface density (colour, kg/m^3) and sea surface height (0.33, 0.34, 0.35 and 0.48 m contours) using the model output for **a)** scenario S1, 23/07/2012, **b)** scenario S2, 06/02/2013, **c)** scenario S3, 07/03/2013 and **d)** scenario S4, 14/04/2013 (indicated in Figure 35b). Note the colour scales are different for each event and the densities have 1000 subtracted from them for better visualisation. Mooring locations are shown by white geometric shapes, as shown in Chapter 2, Figure 4.

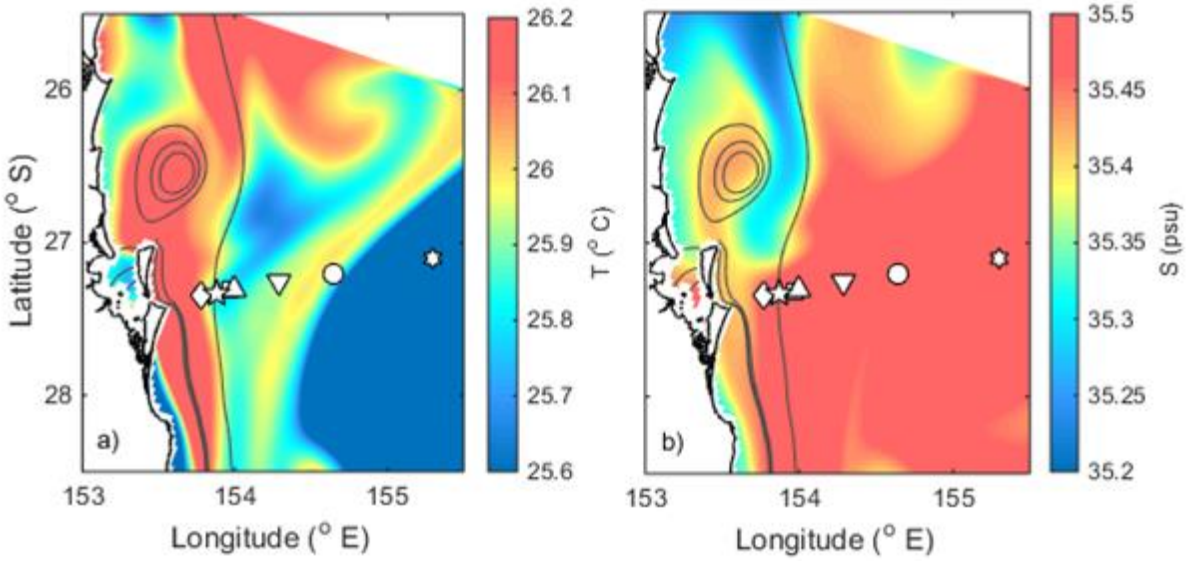

Figure 39: a) Sea surface temperature, **b)** sea surface salinity on 07/03/2013 (Scenario S3 in Figure 35b, Figure 38c) from the model output. The contour lines are 0.33, 0.34, 0.35 and 0.48 m. Mooring locations are shown by white geometric shapes, as shown in Chapter 2, Figure 4.

The offshore current on 7th March 2013 (Figure 40a) is weaker (~ 0.3 m.s^{-1}) above the continental slope, compared to the mean of the entire period analysed in Chapter 3 (Figure 23). A weak onshore current (-0.1 m s^{-1}) is observed offshore (moorings EAC4 and EAC5). The meridional velocity (Figure 40b) on 7th March 2013 is close to the mean observed for the entire period (Chapter 3 Figure 23). The southward velocity of the EAC core is -0.6 m.s^{-1} and between the moorings SEQ200 and SEQ400. No subsurface maximum is observed during this period and high southward flow (> 0.3 m s^{-1}) is observed down to 300 m depth above the continental slope.

The highest stratification occurs between 30 m and 60 m depth (N^2 ~ 4 x 10^{-4} s^{-2}) and high stratification (N^2 > 0.5 x 10^{-4} s^{-2}) extends down to 400 m depth from the continental slope to about 100 km offshore (as shown in model output, Figure 41a). The temperature (Figure 41b) is higher near the surface (>23° C) compared to the mean for the entire period (May 2012 and June 2013) described in Chapter 3 (Figure 24). Higher salinity (> 35.6) occurs below the surface (between 65 and 253 m depth) with the passage of the eddy (Figure 41c) extending from the edge of the continental shelf offshore to 154.6° E.

The root mean square (RMS) of the velocity anomaly (diurnal band) is calculated for 7th March 2013 (Scenario S3 in Figure 35b, Figure 38c) for the observations at each mooring (Figure 42). The RMS of the horizontal velocities, zonal (U_d), meridional (V_d), above the continental slope, are high (> 0.07 m s^{-1}) at isobath of 1000 m and 2000 m (moorings EAC1 and EAC2) below ~368 m depth (Figure 42a,b). Offshore

the horizontal velocities are high (> 0.07 m s^{-1}) in EAC3, above 269 m depth for U_d and below 221 m for V_d, in the isobath of 4000 m (EAC4) near the surface (~45 m depth) and in EAC5 about 194 m depth. The vertical (W) component of the velocity (Figure 42c) reaches 0.034 m s^{-1} above the continental slope (moorings SEQ200, SEQ400, and EAC2), and is higher (> 0.02 m s^{-1}) when compared to the mean for the entire period (maximum 0.013 m s^{-1}) analysed between May 2012 and June 2013 (Chapter 3, Figure 18c). The vertical velocity is also higher than 0.02 m s^{-1} near the bottom above the continental slope (moorings SEQ200 and SE400).

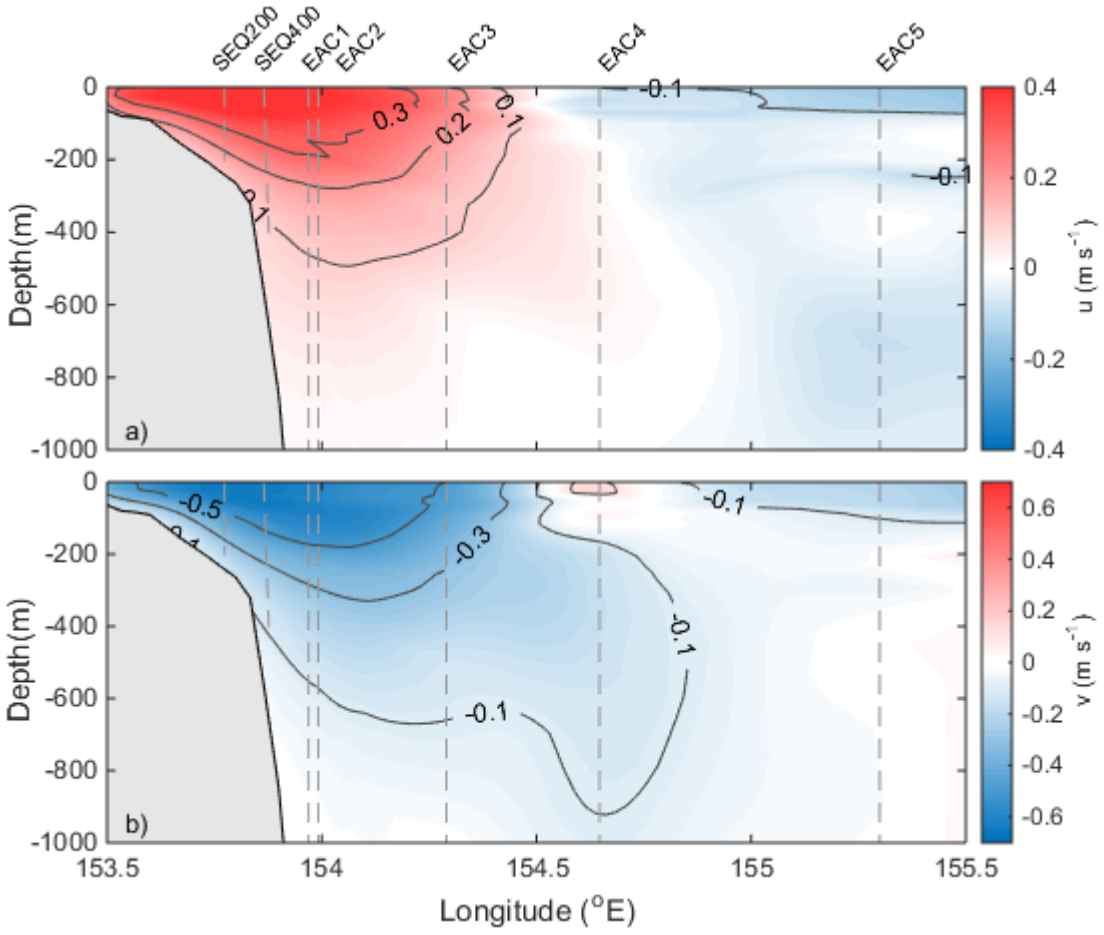

Figure 40: Cross-sections of one day mean of the components of the velocity, **a)** zonal and **b)** meridional, analysed 7th March 2013 from the EAC-ROMS model output. Mooring locations are shown by dashed lines, as shown in Chapter 2.

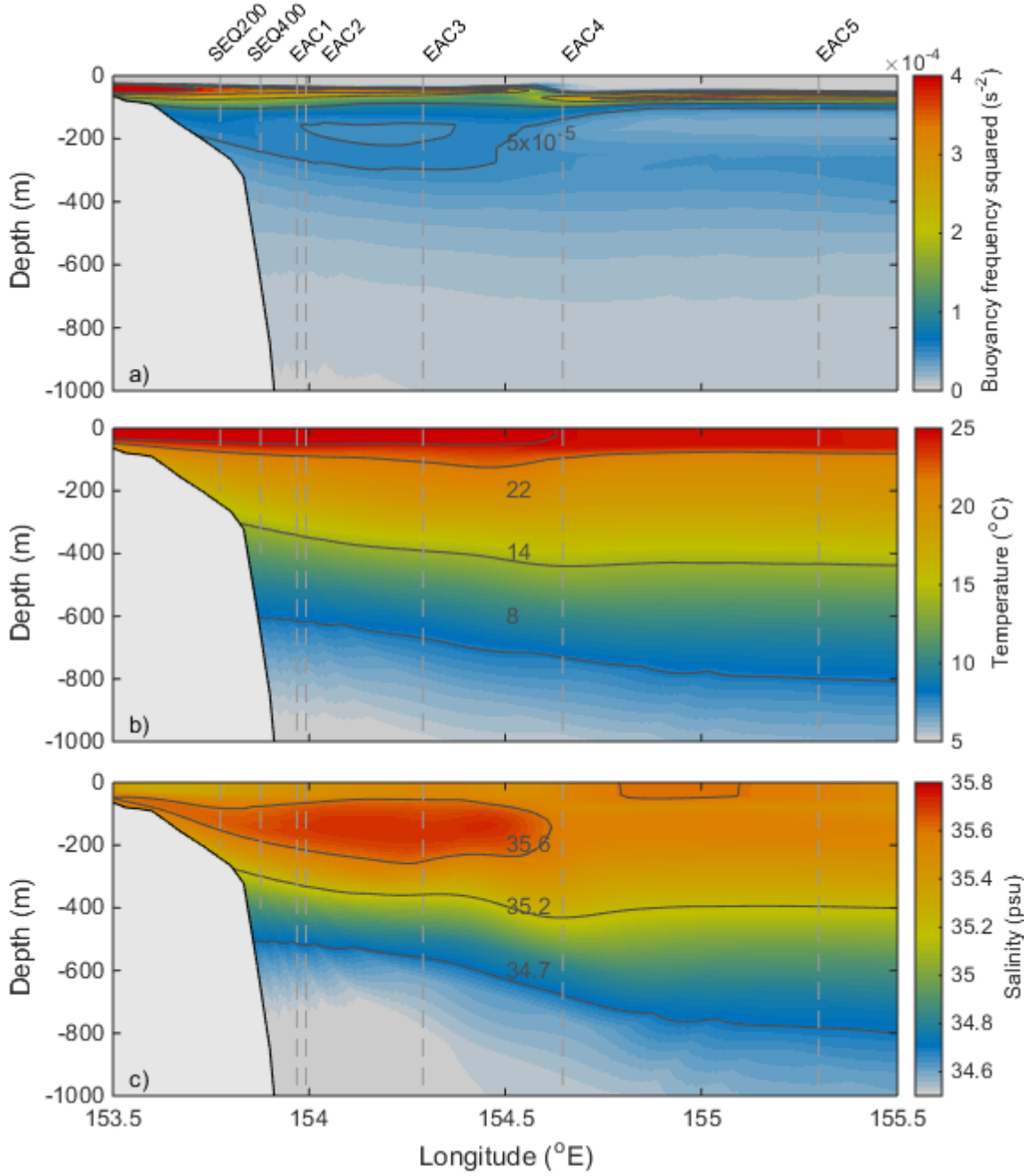

Figure 41: Cross-section of one day mean of the **a)** buoyancy frequency squared (N^2), **b)** temperature and **c)** salinity analysed on 7th March 2013 from the EAC-ROMS model output. Mooring locations are shown by dashed lines, as shown in Chapter 2 Figure 5.

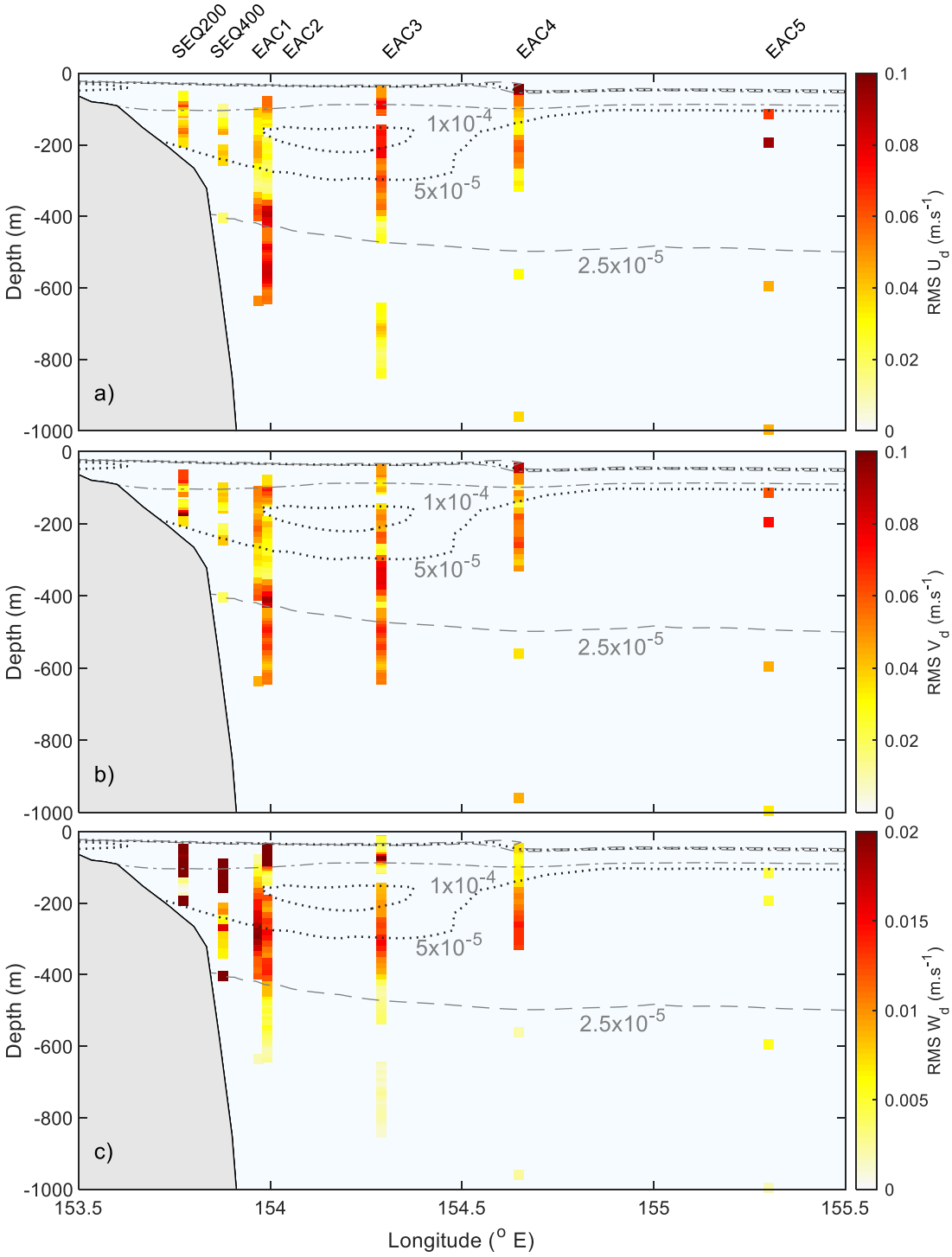

Figure 42: Cross-section of the root mean square (RMS) of the diurnal internal tide velocities anomaly in the **a)** zonal (U_d), **b)** meridional (V_d) and **c)** vertical (W_d) directions from the moored data on 7th March 2013 (Scenario S3, Figure 34). The contours are isolines of the N^2 (s^{-2}) calculated from the EAC-ROMS model output (Figure 40a).

The time series of observed data from the mooring SEQ400 (over the 400 m isobath), between 15th February 2013 and 15th March 2013, is presented in Figure 43. The eddy kinetic energy (EKE) is calculated from the moorings data to determine the passage of the eddy. The stratification near the bottom, between 270 and 364 m depth, is compared to the EKE, at 400 m, and the diurnal internal tide, pressure anomaly (~100-400 m), temperature anomaly (364 m) and vertical velocity anomaly (400 m) between the two neap-spring cycles of the tide.

The first spring tide occurs on 20th February 2012, the second occurs on 7th March 2013 and the amplitude of the tide height reaches 0.2 m during both (Figure 43a). During the first spring tide (Figure 43a), there was no evidence of the passage of an eddy (Figure 43a). The Sea Surface Height anomaly (SSHa) is lower than 0.1m, the EKE was lower than 0.1 m^2s^{-2} and the stratification of the water column above the continental slope was low ($N^2 \sim 2.10^{-5}\ s^{-2}$) with no evidence of strong internal tide generation (Figure 43b). However, at the second spring tide (7th March 2013, Scenario S3) the eddy described in Figures 38c, 38, passed through the study area. The SSHa increased (> 0.1m), the EKE (Figure 43b) reached 0.03 m^2s^{-2}, and the stratification increased ($N^2 > 4.10^{-5}\ s^{-2}$) above the continental slope. The generation of the internal tide is observed simultaneously. The pressure anomaly (diurnal) over the water column increases from ~ 0.01 to 10 db (Figure 43c), the temperature anomaly (364 m) reaches 0.9° C (Figure 43d) and the vertical velocity anomaly rises from 0.01 to 0.04 m s^{-1} at 400 m depth (Figure 43e).

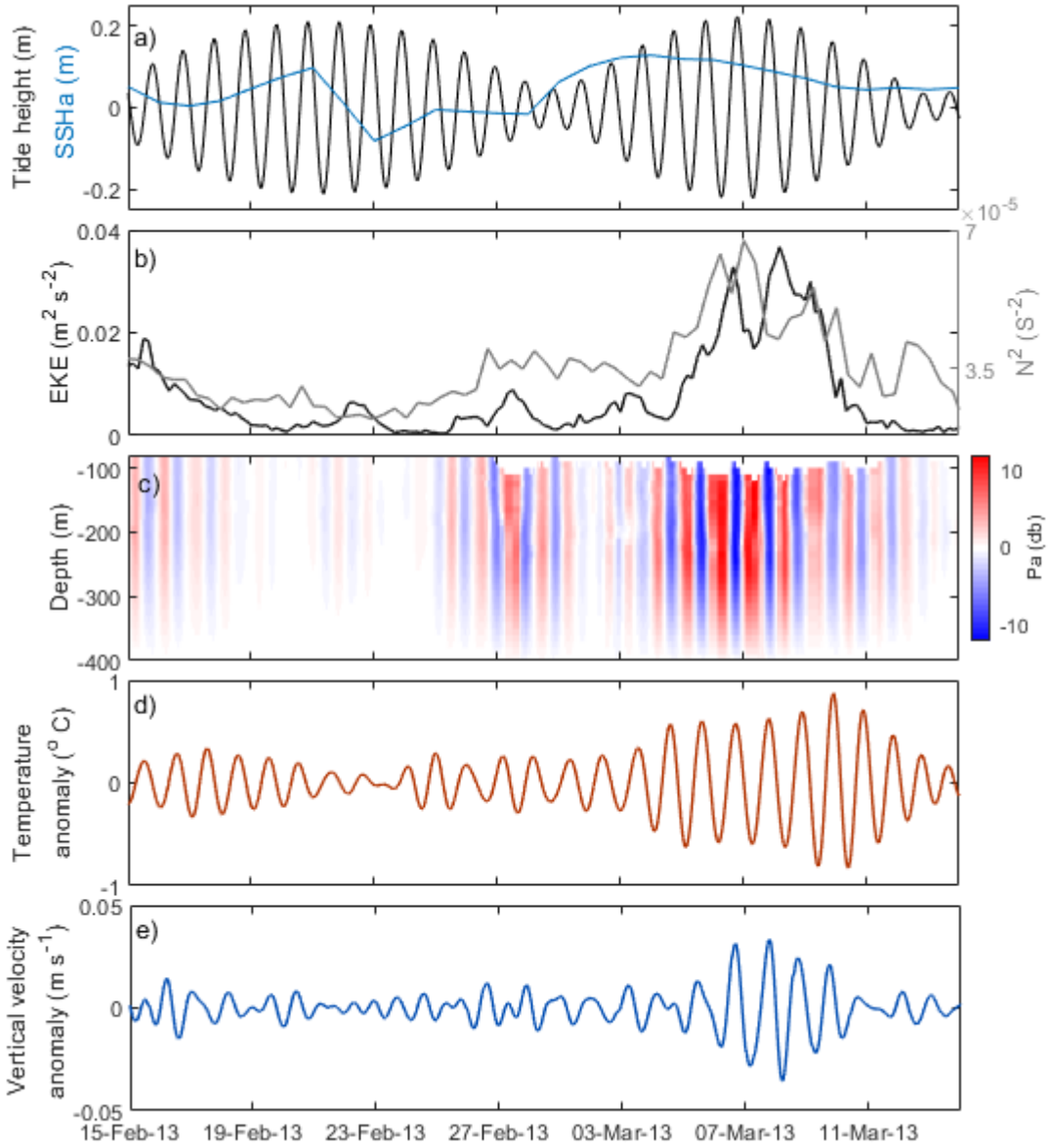

Figure 43: a) Diurnal (constituents K_1 and O_1) tide surface height (in black) estimated using TPXO and Sea Surface Height anomaly (in blue) observed from detided altimetry data. Observed data from the mooring SEQ400 is used to calculate the **b)** Eddy kinetic energy (EKE) at 400 m depth and buoyancy frequency (N^2) calculated between 270 and 364 m depth, **c)** Profile of the pressure anomaly, **d)** near-bottom (364 m depth) temperature anomaly and **e)** near-bottom (400 m depth) vertical velocity anomaly at the diurnal frequency.

4.3.2 Characteristics of the Cyclonic Eddies

Cyclonic eddies are observed in all seasons of the year analysed. Sometimes the eddies passed as a train of 3 or 4 eddies (Figure 44a). The surface temperature of the eddy field varies from eddy to eddy, and the eddies were warmer during the summer (14th December 2012 and 06th February 2013) of the period analysed with a temperature higher than 27^{o} C at the edge of the eddies.

The characteristics of the eddies are analysed using the sea surface height anomaly (SSHa) from the ROMS model. Each of the eddies have closed streamlines, are asymmetric and have different shapes (Figure 45). The sea surface height anomaly is calculated over the entire model domain, with the effect being that the anomalies presented here are all positive. The height of the core of the eddies varies from 0.25 to 0.45 cm and the diameter of the eddies range between ~30-35 km.

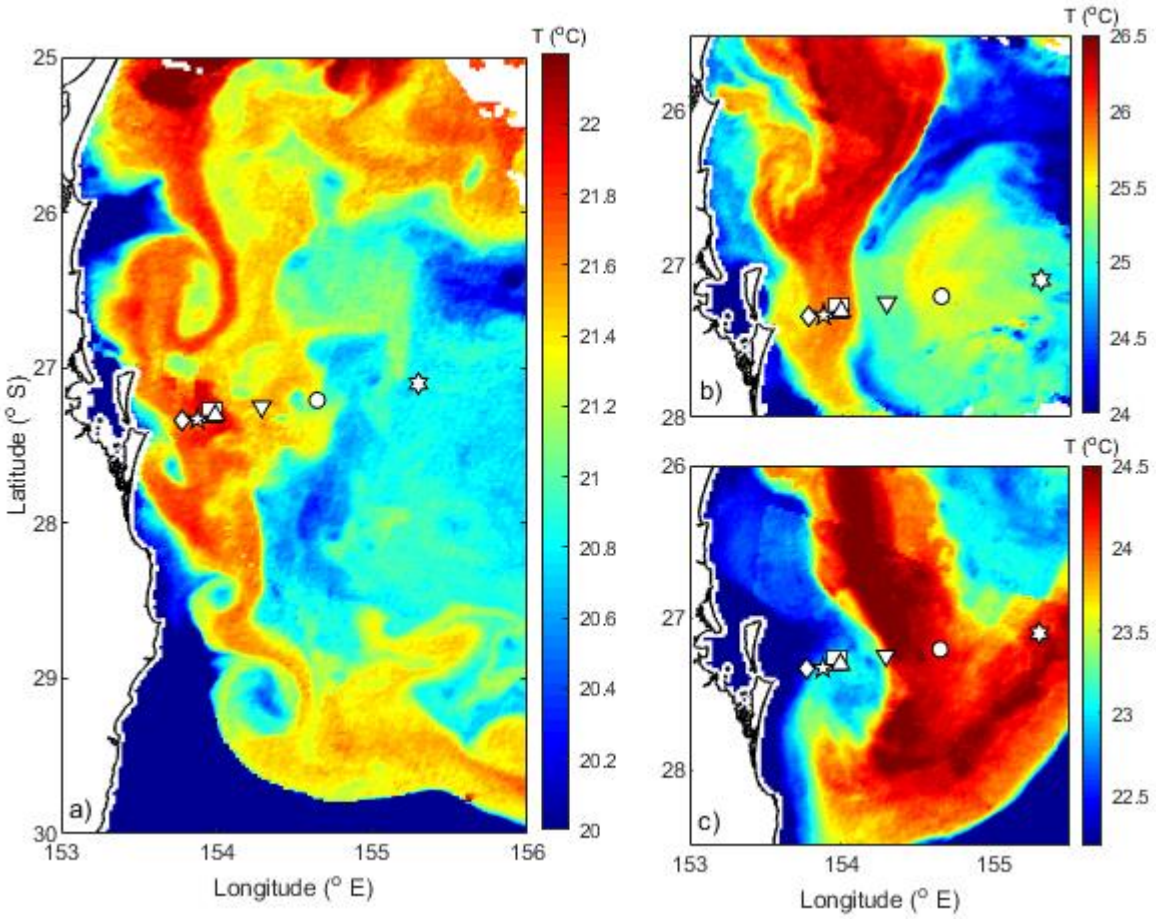

Figure 44: Snapshots of sea surface temperature (° C) from satellite showing examples of cyclonic eddies passing through the study area from **a)** 14th August 2012, **b)** 25th April 2012 and **c)** 17th October 2012. Note the colour scale changes each snapshot. Mooring locations are shown by white geometric shapes, as shown in Figure 4 (Chapter 2).

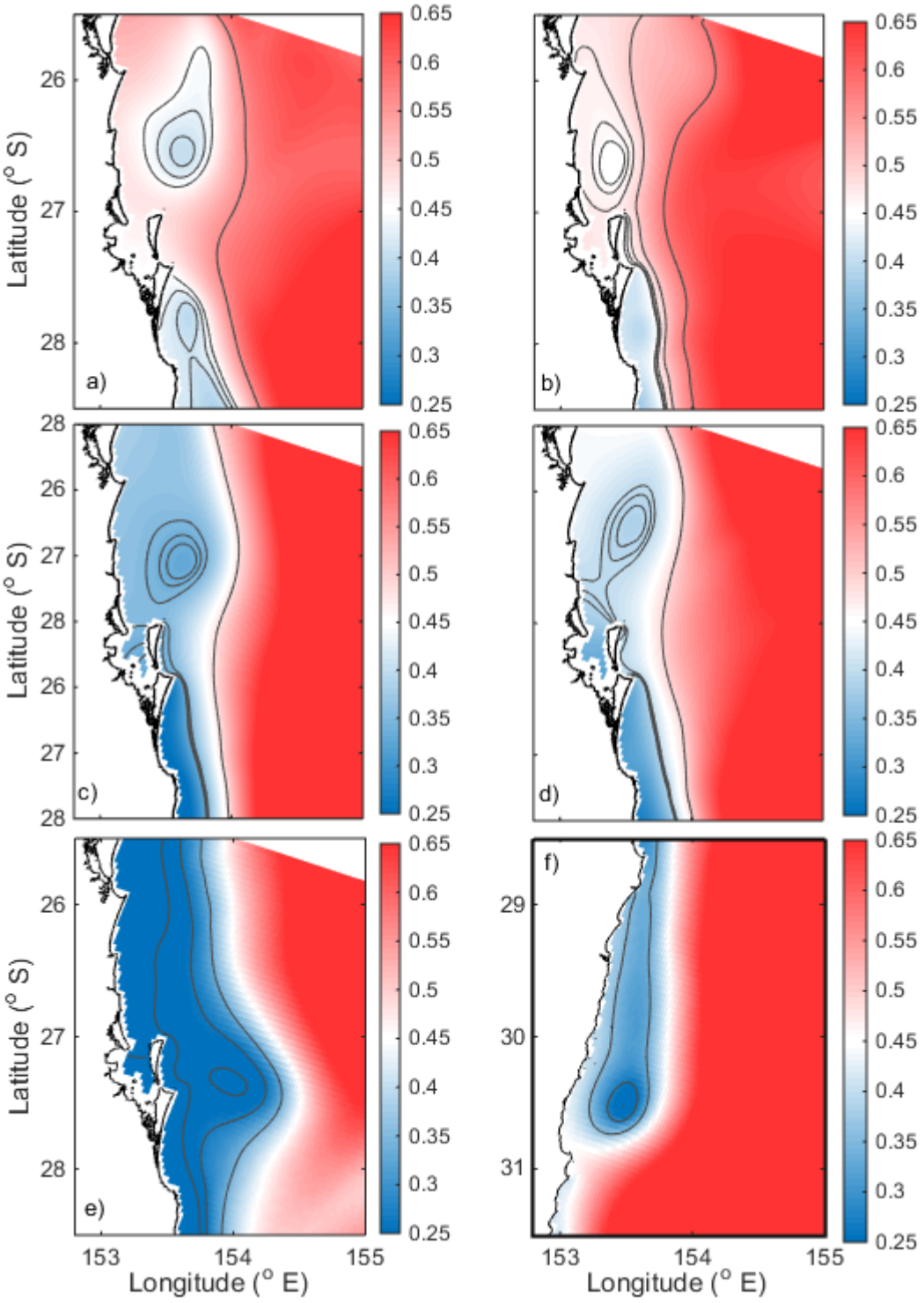

Figure 45: Snapshots of the sea surface height (m) of the frontal cyclonic eddies from the model output in the study area (27°S) on **a)** 23/07/2012, **b)** 06/02/2013, **c)** 07/03/2013, **d)** 14/04/2013, **e)** 17/10/2012; and **f)** a frontal cyclonic eddy observed south of the study area (30°S) on 03/02/2013 that was analysed by Schaeffer et al. (2017). The contour lines are 0.33, 0.34, 0.35 and 0.48 m.

4.4 Discussion

Here we use in situ data obtained from a comprehensive long-term mooring array combined with output from a high-resolution numerical model to analyse how cyclonic frontal eddies modulate internal tides by enhancing the local stratification above the continental slope. The time series of the spectral density (SD) show the temporal variability of the diurnal internal tide. The variability has a spring neap cycle and higher peaks of SD are observed with the passage of frontal eddies. We analyse the buoyancy frequency squared (N^2) to infer the stratification and eddy kinetic energy (EKE) to show the impact of the propagation of cyclonic eddies through the study site. The EAC-ROMS model output provides spatial and temporal context to the moored observations and provides insight into the ocean dynamics. The modulation of the diurnal internal tide above the continental slope at 27^{o}S is analysed and shown to be significant. The results show the relationship between the passage of frontal eddies and changes in the local stratification that reflects on the internal tide variability.

Internal tides can be generated above the continental slope because of steep topography (Baines 1982). The generation of internal tides above the continental slope occurs when the slope of the bathymetry matches the slope of the internal tide (Craig 1987). This relationship is analysed in Chapter 3 (Section 3.3.4), where high criticality above the continental slope (mean >15) in the study area is observed. Their generation depends on background stratification and barotropic tidal forcing (Holloway and Merrifield 1999; Kelly and Nash 2010). The local stratification plays an important role in the variation of the internal tide generation (Gemmrich and van Haren, 2002; Katsumata et al. 2010). Higher stratification is favourable for the generation of the internal tide above the continental slope (Baines, 1982).

The results presented here show that the vertical scales of the internal tide signal (vertical velocity, temperature, and pressure) measured near the bottom (~ 400 m) over the continental slope increase simultaneously with the increase of stratification and EKE at spring tide (Figure 43). Spatial analysis of the eddy shows that the maximum stratification is at the leading edge of the eddy (Figure 38). Where a higher horizontal gradient of temperature is observed and the amplitude of the vertical velocity and temperature of the internal tide near the bottom of the continental slope reaches 0.03 m s^{-1} and 0.9 ^{o} C respectively (Figure 43d,e). The results show evidence of the influence of the frontal cyclonic eddy on stratification and thus on the internal tide at the near bottom of the continental slope. These results are consistent with Jeon et al. (2014) who show that seasonal variation on the generation of the internal tides can be modulated by the seasonality in stratification in the Japan Sea. The authors suggested that the stratification is affected by the Tsushima Warm Current that flows from the East China Sea into the Japan Sea through the Tsushima Straits and the yearly monsoons.

The circulation along eastern Australia is variable and energetic in terms of meso and sub-mesoscale features that can affect the local stratification (Archer et al. 2017; Roughan et al. 2017; Schaeffer et al. 2017). The high coherence of the EAC at 27°S contributes to the complexity of the dynamics (Sloyan et al. 2016). While we know that the EAC is generally coherent at 27°S, little is known about the frequency of cyclonic eddy generation in the region. Furthermore, less is known on the impact on subsurface stratification and how this affects the internal tide.

Previous studies have shown the influence of stratification on the intensification of the internal tide (Townsend 1966; Baines 1982; Kelly and Nash 2010). To our knowledge, none have related this change in stratification to the passage of frontal eddies with diameters about 30 km. This study shows details of the intensification of the internal tide with the passage of small frontal eddies that occur frequently in the study area.

Studies in the EAC region have shown that cyclonic frontal eddies can form on the inshore edge of the current (Roughan et al. 2017; Shaeffer et al. 2017). Similar frontal eddies are observed in the study area with a diameter of about 30 km. Despite their small size and short life (~4 weeks), these frontal eddies are one of the main transport mechanisms of nutrients from the coastal zone to deep waters (Shaeffer et al. 2017). They can retain coastal larval species and be more ageostrophic, energetic and productive than mesoscale cyclones as observed by Roughan et al. (2017).

The generation mechanism of the eddies is still under discussion. The main source of energy for the growth of the cyclonic eddy is suggested to be barotropic instability of the EAC, rather than baroclinic or wind-driven processes (Oke and Griffin 2011; Macdonald et al. 2016), however, they intensify during strong northward wind stress (Shaeffer et al. 2017), counter to the EAC flow.

The frontal eddy observed by Roughan et al. (2017) extended to more than 1000 m depth and was tilted onto the continental slope (toward the SW) through the water column. The authors associated the tilt with an asymmetric uplift through the core of the eddy. They observed convergence and downwelling on the EAC edge and the divergence and upwelling on the coast edge observed in the frontal eddy. The mixed layer depth is deeper on the EAC edge of the cyclonic front, caused by convergence and downwelling of the water masses. This could also explain the deeper (~ 400 m) stratification ($N^2 \sim 5 \times 10^{-5}$ S^{-2}) observed with the passage of the eddies in the study area (Figure 40a). Strong temperature horizontal gradient on the edge of the frontal eddies was also observed by Schaeffer et al. (2017) at 30°S (Figure 45f). Further studies using internal tide models are suggested to quantify the role eddies play in mediating internal tide generation to explain the coherence of the internal tide.

4.5 Conclusion

Despite the high frequency of frontal eddies along the inside edge of WBCs and their importance in changing the vertical structure of the ocean, little is known about their influence on internal tides.

Here we showed an intensification of the diurnal internal tide (as represented by high spectral density (> 0.1^{o} C^{2}/(1/days)), that is related to an increase in stratification near the bottom of the continental slope during the spring tide. We showed that the increase in stratification can be attributed to the passage of small frontal cyclonic eddies that occur frequently in the region (12 times during our 13-month period). The eddies are small, with a diameter of approximately 30 km with high velocities on their eastern flank, and they enhance the near bottom stratification (> 0.5 x 10^{-5} s^{-2}) above the continental slope.

The intensification of the internal tides modulates principally the vertical displacement of the isotherms (as observed in temperature and vertical velocity). These are the first observations of a new mechanism that modulates the strength and amplitude of the diurnal internal tide off Eastern Australia.

Chapter 5: Evidence of Eddy-Barotropic Tide Interaction off Eastern Australia

5.1 Introduction

Mesoscale eddies can interact with the barotropic tide and create resonance conditions that intensify the baroclinic flux, as a triad of waves (eddy, barotropic tide and internal tide) and thereby generate internal tides (Olbers 1981). Eddy field and barotropic tide resonance can facilitate the energy transfer to the internal tide. The eddy field evolves independently of the barotropic tide and acts catalytically in facilitating energy transfer from the barotropic tide to the internal tide, without exchanging energy with the other flow components. Details of this mechanism are described by Lelong and Kunze (2013) using numerical models. They showed that internal tide generation depends on the scales (wavenumber and velocity) of the barotropic tide and the eddy field, and the best resonant conditions occur when the horizontal scale of the tidal current is close to that of the eddies.

The resonance condition depends on the spatial (wavenumber) and temporal (frequency) scales of the eddy and the barotropic tide (Lelong and Kunze 2013) following the conditions:

$$k_0 \pm k_1 = k_2 \; ; \; \omega_0 = \omega_2(k_2), \tag{29}$$

where k is the horizontal wavenumber, ω the frequency. ω_0 and κ_0 are frequency and wavenumber, respectively, of the barotropic diurnal tide. κ_1 is the wavenumber of the eddy field with time scale $1/k_1 U > 2\pi/\omega_0$, where U is an eddy velocity scale. ω_2 and κ_2 are the frequency and wavenumber, respectively, of the internal tide.

This mechanism plays a role in the ocean, but it is thought that it is not common because the length scales of a mesoscale eddy need to match to the barotropic tide. The current strength of the eddy is normally stronger than the current strength of the barotropic tide. Moreover, the mechanism is difficult to observe due to the transient nature of the eddies and a paucity of sub-surface observations.

As described earlier, the study area is located where the flow of the East Australian Current (EAC) intensifies forming a strong western boundary current (Sloyan et al. 2016). This region is also identified as having a large number of short-lived (7-28 days) cyclonic eddies (CEs), about four or five per year (Ribbe and Brieva 2016). The size of the mesoscale eddies in EAC range from 100-300 km (Everett et al.

2015; Rykova and Oke 2015), and form from meanders in the flow and instability of the barotropic and baroclinic flux that propagate in EAC (Mata et al. 2006; Roughan et al. 2017).

The CEs are cold-core eddies that form on the coastal side of the EAC (frontal eddies). They are associated with entrainment of coastal waters and generate a near-shore northward flow (Roughan et al. 2011; Everett et al. 2011; Roughan et al. 2017; Schaeffer et al. 2017). In addition to the frontal eddies that form and grow on the inside edge of the EAC, larger cyclonic eddies can propagate into the region associated with westward propagating Rossby Waves (e.g. Kerry et al. 2020). The core of these eddies is tilted through the water column to westward (Roughan et al. 2017). The uplift of the isotherms of the eddy is asymmetric and deeper in the eastern side of the eddy where the EAC is located.

Most of the eddies presented in Chapter 4 are small eddies that started as frontal eddies on the inside edge of the EAC. The core of the EAC (west side of the eddy) is above the continental slope and the velocities are stronger (more than double) compared to the barotropic tide (maximum 0.3 m s^{-1}). However, a larger frontal cyclonic eddy, with a radius of about 46 km (Ribbe and Brieva 2016), is observed in the study area with a velocity comparable to the barotropic tide (Figure 45 and Chapter 4 Figure 36b). In this chapter, we investigate if there are resonance conditions for the interaction between this eddy field and the barotropic tide resulting in the generation of internal tides at the study area. We compare the horizontal scales (velocities and wavenumbers) of the eddy field with the barotropic tide. The effect on the internal tides in both horizontal (velocity) and vertical (temperature and velocity) scales are analysed. We show observational evidence of internal tides generation in an eddy field.

5.2 Methods

We identify a mesoscale cyclonic eddy that passed through the study area using sea surface temperature (SST) and geostrophic velocity from satellite data (described in Chapter 2 Section 2.4). The eddy was first identified on May 28th, 2012 located at 155.2^{o}E and 26.3^{o}S and it had dissipated by 11th July (Figure 46). It interacted with the shallow water (< 40 m) and exported shelf waters off-shore as evident from entrained water characterised by elevated Chl-a and cooler coastal water (Ribbe and Brieva 2016). It is thought that this eddy was a frontal eddy that grew in size as it propagated south into the domain.

We compare the horizontal scales (wavenumber and current velocity) of the eddy field with the barotropic tide. We estimate the wavenumber and the velocity of the barotropic tide from a cross-

section at 27°S from the global tide model TPXO (described in Section 2.3). We use the EAC-ROMS model output (described in Section 2.5) to analyse the characteristics of the eddy (horizontal velocity and vertical structure). The spectral density of the wavenumber of the eddy field is calculated using the EAC-ROMS model during the time that the cyclonic eddy passed through the domain (5th June to 10th July 2012). The effect of the eddy on the internal tide is analysed using the mooring data (described in Section 2.2). We analyse the time series (observed data) of the eddy kinetic energy (EKE) and compare it to vertical and horizontal components of the internal tide. The vertical component is analysed using vertical velocity anomaly and temperature anomaly, and the horizontal component is analysed using zonal and meridional velocities anomaly.

The analyses are used to observe if the eddy and the barotropic tide have similar horizontal scales (wave number and velocities) favourable for resonance conditions and internal tide generation.

5.3 Results

5.3.1 Eddy characteristics

The eddy characteristics are analysed using SST and geostrophic velocity, from satellite images, eddy kinetic energy calculated from the velocity data from EAC mooring array, and the cross-section of the velocity and vertical structure (temperature, salinity, and buoyancy frequency) using the EAC-ROMS model output.

Satellite-derived SST data show the passage of the cyclonic eddy in the study area. The eddy developed north of the study area (between 25°S and 26°S) and propagated toward the south. The eddy reaches the mooring array (27°S) on 14th June observed in the SST which shows a temperature of higher than 23° C (Figure 46) encircling cooler water (~ 22 ° C). Its core passed through the mooring array (27.2°S) between 28th June and 2nd July 2012 (Figure 46c,d) and had left the study area by 10th July 2012 (Figure 46e).

The passage of the eddy is observed across the mooring array (Figure 46). The time series of the eddy kinetic energy (EKE) calculated from the detided velocity observed from the moorings (Figure 5) shows that the EKE increases between 14th June and 10th July (Figure 47). During this period the currents are relatively weak, and hence not susceptible to mooring tilt. The EKE reaches 0.2 $m^2 s^{-2}$ from close to the surface until 200 m depth. The moorings SEQ200 and SEQ400 show two periods of higher EKE, one between 24th and 29th June and other between 1st and 10th July (Figure 46a,b). The deepest EKE occurs in

the moorings EAC1, EAC2 and EAC3 (i.e., across and adjacent to the continental slope) reaching 0.06 m^2 s^{-2} at 600 m depth on 29th June 2012 (Figure 46c,d,e). The high EKE (> 0.2 m^2 s^{-2}) regions at the offshore moorings (EAC4 and EAC5) still extend down to > 200 m depths, but the data in the surface waters is missing from the dataset (Figure 46f,g).

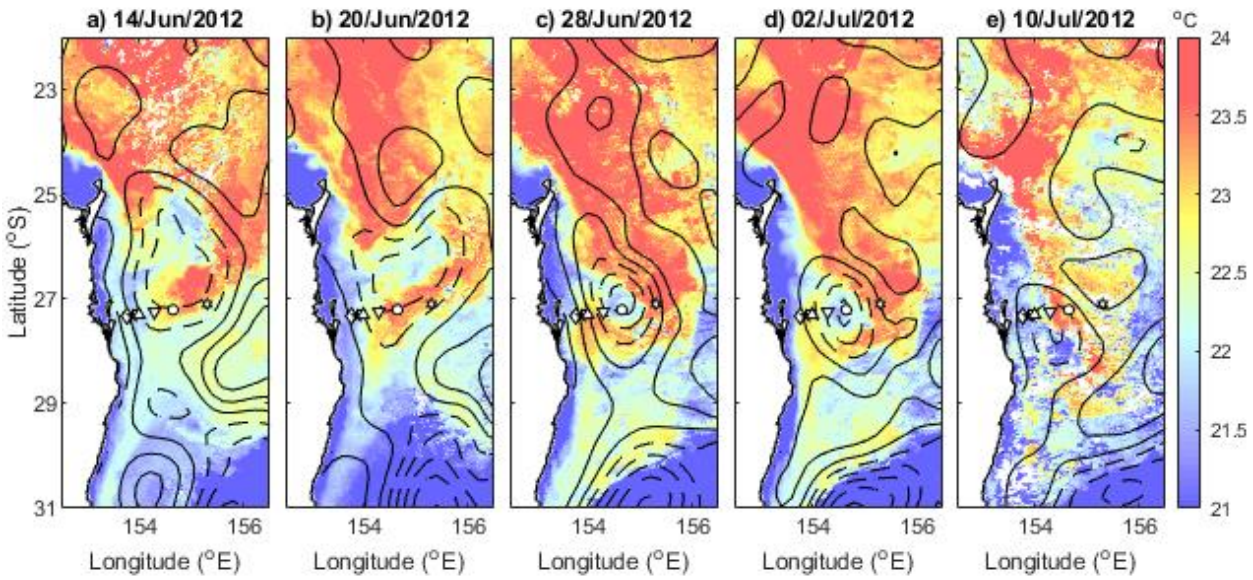

Figure 46: Satellite images of sea surface temperature (SST) showing the development and advection of the cyclonic eddy between 14th June and 10th July 2012 (**a**-**e**). The dashed contour lines are negative sea surface height anomaly (SSHa) and the continuous contour lines are positive SSHa. Mooring locations are shown by white geometric shapes, as shown in Figure 4.

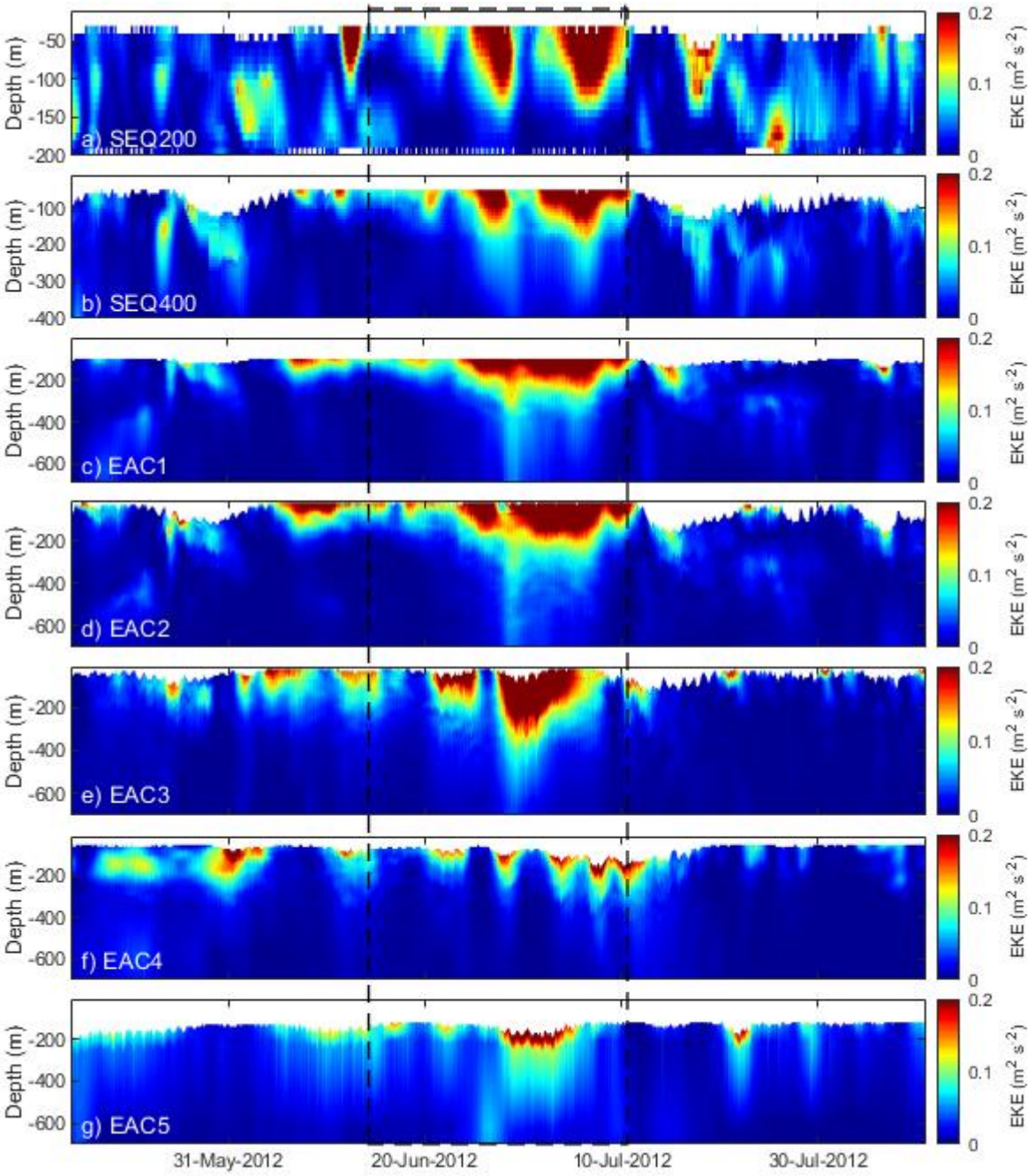

Figure 47: Time series of the eddy kinetic energy calculated from the detided velocity observed at the moorings SEQ 200, SEQ400, EAC1, EAC2, EAC3, EAC4 and EAC5 (**a**-**g**) as shown in Figure 5. The detided velocity data (EAC1) is shown in Figure 51. Note the different vertical scales on the panels as the moorings get deeper. The dashed line represents the period between 14th June and 10th July 2012 that the eddy is observed in the study area (Figure.46)

A snapshot of the SST and geostrophic velocity from satellite data shows the cyclonic eddy with the mooring array aligned at its centre on the 2nd of July 2012 (Figure 48). The surface temperature is approximately 23° C at the edge and 21.5° C in the core of the eddy. The current velocities were lower than 1 m s^{-1} and are maximum at the offshore edge of the eddy (driven by the poleward flowing EAC). The velocity at the inshore edge of the eddy is a northward flow of less than 0.5 m s^{-1}. The velocity above the continental slope (Figure 48) is weaker and can be compared to the barotropic tide.

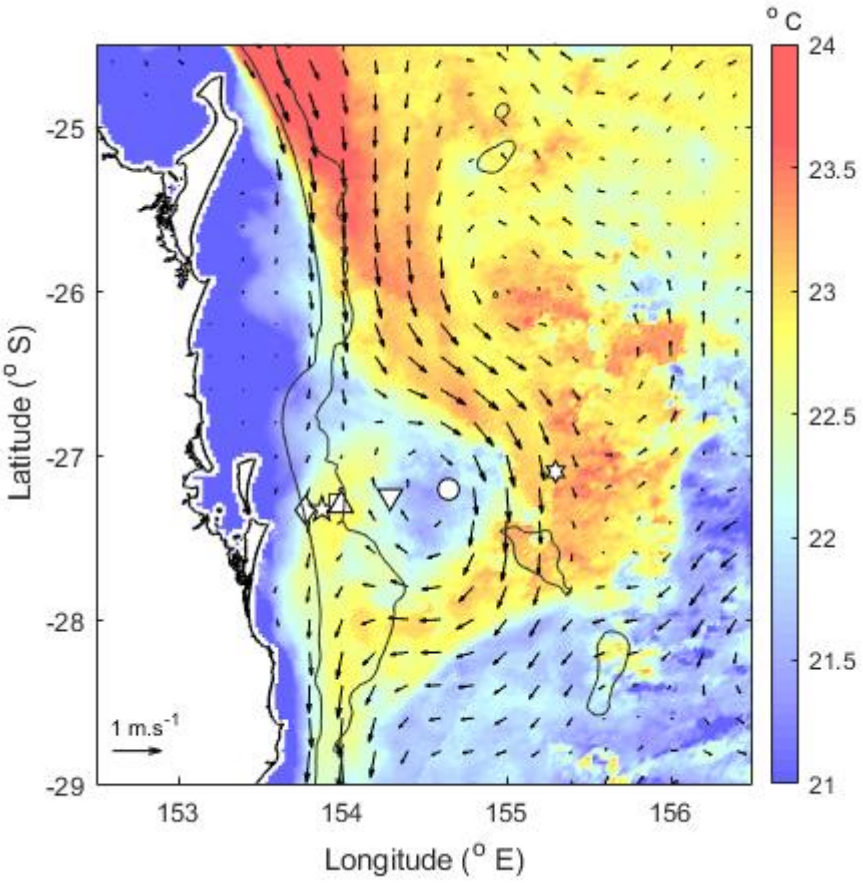

Figure 48: Sea surface temperature (SST) showing the cyclonic eddy in the study area surrounded by the poleward flowing EAC on 2nd July 2012. The arrows indicate the geostrophic velocities. Mooring locations are shown by white geometric shapes, as shown in Figure 4. The contours are 200m and 1000m isobath.

The results show a typical cyclonic eddy with southward flow located offshore and northward flow close to the coast (Figure 48). Figure 49 shows vertical cross-sections of mean (over 24 hrs) velocity components (detided), zonal (u_{dt}) and meridional (v_{dt}) on 2nd July using model output at 27^{o}S. The zonal velocity (Figure 49a) is predominantly westward 0.1 - 0.2 m s^{-1}. Eastward current is weaker (maximum 0.1 m s^{-1}) and is observed near the surface over the 200 m isobath (SEQ200). Flow is onshore, above the continental slope. The maximum southward velocity occurs near the surface (0.8 m s^{-1}) close to the mooring EAC5 (Figure 49b), i.e., more than 150 km from the coast. This indicates that the EAC has been deflected offshore by the passage of the cyclonic eddy. The maximum northward velocity of the current (0.3 m s^{-1}) occurs close to the surface over the 2000 m isobath (close to the mooring EAC2). The core of the eddy is located at Longitude 154.4^{o} E (near EAC3) where the meridional velocity is close to zero (dotted lines Figure 49b).

The buoyancy frequency squared (N^2), temperature and salinity are estimated using EAC-ROMS model output (Figure 50). N^2 is higher than 1x10^{-4} S^{-2} between 40 and 104 m depth and the highest stratification (2 x10^{-4} S^{-2}) occurs above the continental slope (66 m depth over the 200 m isobath) near the mooring SEQ200 (Figure 50a). There is an uplift between the moorings EAC3 and EAC4, where the core of the eddy is located (Longitude 154.4^{o}E). The uplift is asymmetrical, and the stratification (isoline of N^2 = 2.5x10^{-5} s^{-2}) is deeper (480 m) in the east side of the eddy (Longitude 155.5^{o}E), compared to the inshore side (334 m, Longitude 153.8^{o}E) and is shallower (221 m) in the core of the eddy (Longitude 154.5^{o}E).

The temperature is higher (> 24^{o} C) offshore (Figure 50b) in the surface waters, compared to the surface temperature recorded above the continental slope (SEQ200, SEQ400, EAC1 and EAC2) where the surface temperature is lower than 23^{o} C. The offshore high temperature is associated with the core of the EAC jet on the east side of the eddy (EAC5). The 22^{o} C isotherm is also deeper offshore (143 m depth) close to the mooring EAC5) than above the continental slope (43 m depth between the moorings SEQ200 and EAC2).

High salinity (> 35.6) occurs offshore close to EAC5, between 101 m and 229 m depth (Figure 50c). The salinity close to the moorings above the continental slope (SEQ200, SEQ400, EAC1 and EAC2) is ~ 35.5 between 61 and 128 m depth. The salinity is lower than 35.2 below 237 m close to the moorings located above the continental slope and below 338 m depth offshore, close to the mooring EAC5.

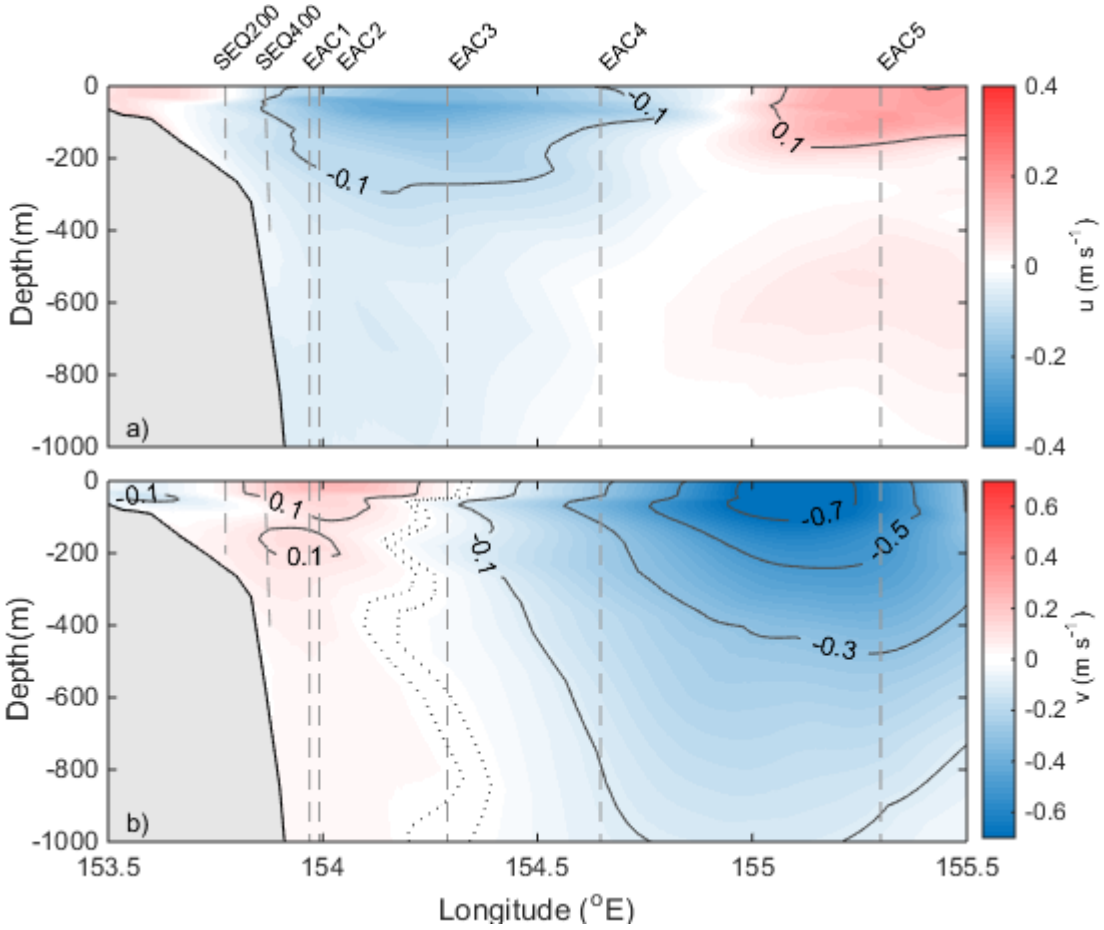

Figure 49: Cross-sections of one day mean of the components of the velocity from the ROMS model, **a)** zonal and **b)** meridional, analysed on 2nd July 2012. The dotted lines show the core of the eddy (v ~ 0). Mooring locations are indicated by dashed lines, as shown in Chapter 2 Figure 5.

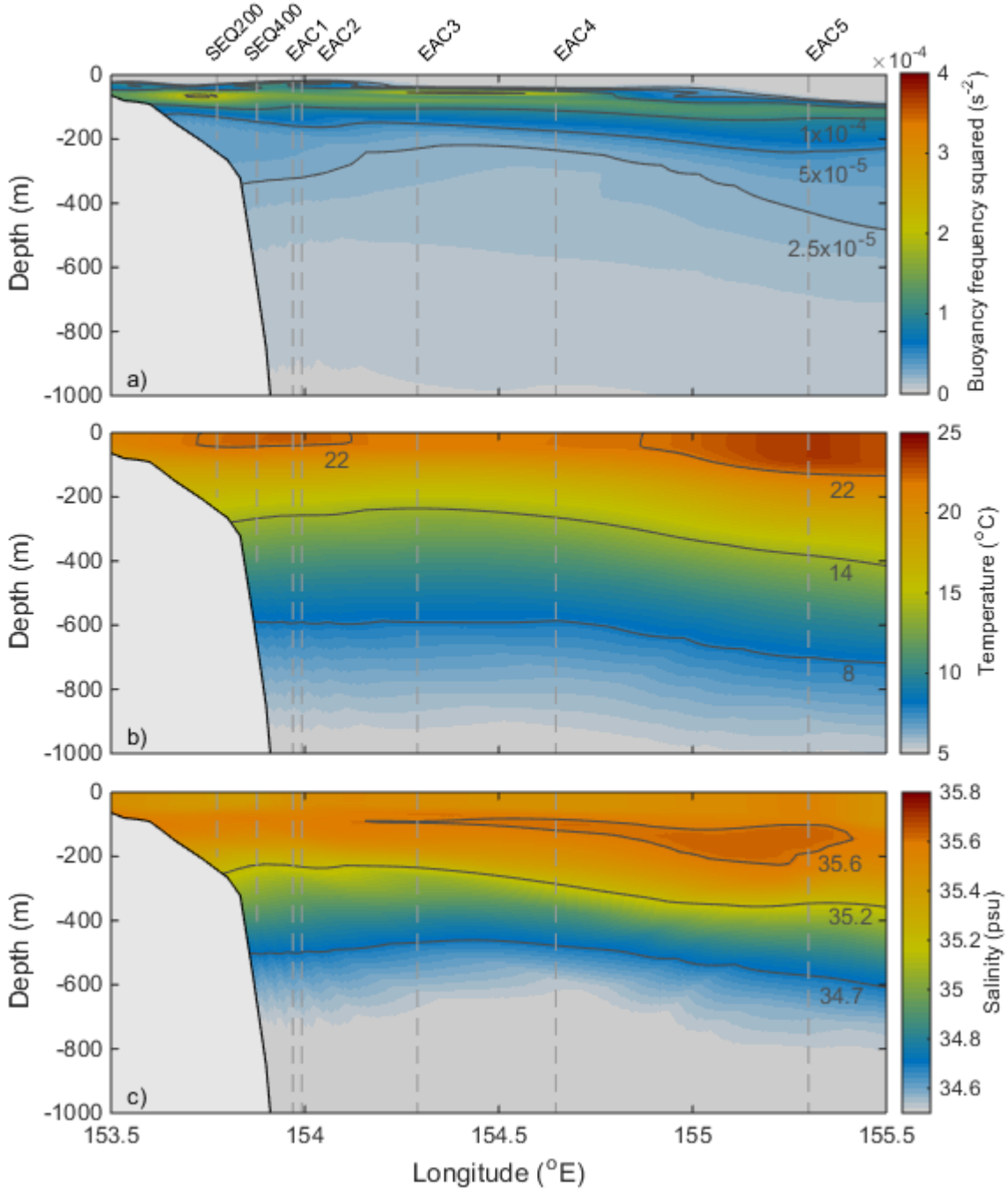

Figure 50: Cross-section of one day mean of the **a)** buoyancy frequency squared (N^2), **b)** temperature and **c)** salinity analysed on 2nd July 2012 at latitude 27°S. The data are from the EAC-ROMS model and the mooring locations are shown by dashed lines, as shown in Chapter 2 Figure 5.

5.3.2 Exploring Resonance Conditions

Since the internal tide generation depends on the scales (wavenumber and velocity) of the barotropic tide and the eddy field, we explore resonance conditions by comparing the wavenumber and the velocity of the eddy field with the barotropic tide. The wavenumber of the eddy field, calculated from SSH, using the EAC-ROMS model, is compared to the wavenumber of the barotropic tide, calculated using the TPXO model (Figure 51). The limit of the mesoscale range is between ~ 0.004 (1/250) and ~ 0.0133 (1/75) cycles per km (Rocha et al. 2016) and the spectral density of the eddy field is higher than 10^{-2} m^2/km^{-1} in this mesoscale range (Figure 51 blue line). The spectral density of the barotropic tide is higher than 10^{-4} m^2/km^{-1} between the mesoscale range (Figure 51 red line) and no spectral density is detected in the sub-mesoscale range (Figure 50). That means that the barotropic tide has spectral density in the same range as the mesoscale eddy field.

The spectral density of the wavenumber of the barotropic tide and the wavenumber of the mesoscale eddy field at 27°S are such that resonance conditions can occur (Figure 51). However, the sub-mesoscale range is not in the same wavenumber range as the barotropic tide and does not satisfy the resonance condition for internal tide generation (Figure 51).

The velocity components of the barotropic tide (zonal, U_{bt} and meridional, V_{bt}) estimated using TPXO (Figure 52a) are compared to the eddy velocity components (detided, u_{dt} and v_{dt}) observed in the mooring EAC1 (Figure 52b,c). Two tidal cycles occur during the passage of the eddy (Figure 52a). The zonal and meridional velocities of the barotropic tide (U_d and V_d) reach an amplitude of 0.1 m s^{-1} and 0.2 m s^{-1} respectively, at the spring tide (Figure 52a). They are comparable to the zonal and meridional detided velocities (u_{dt} and v_{dt}) and they are lower than ±0.2 m s^{-1} between 5th June and 10th July (Figure 52b,c). The velocity of the internal tide (diurnal frequency) increases simultaneously with the passage of the eddy reaching 0.2 m s^{-1} (Figure 52d,e). The intensification of the internal tide reaches more than 300 m depth.

The ratio between the detided current velocities (u_{dt} and v_{dt} Figure 52b,c) and the barotropic tide (U_{bt} and V_{bt} Figure 52a) is shown in Figure 53. The detided zonal velocity (u_{dt}) is proportional (ratio ~ 1) to the zonal barotropic tide (U_{bt}) most of the time. However, the detided meridional velocity (v_{dt}) above 400 m is, most of the time, in a ratio of three higher than the barotropic tide velocity (V_{bt}), except between 5th June and 10th July 2012 when the ratio is close to one (Figure 53b).

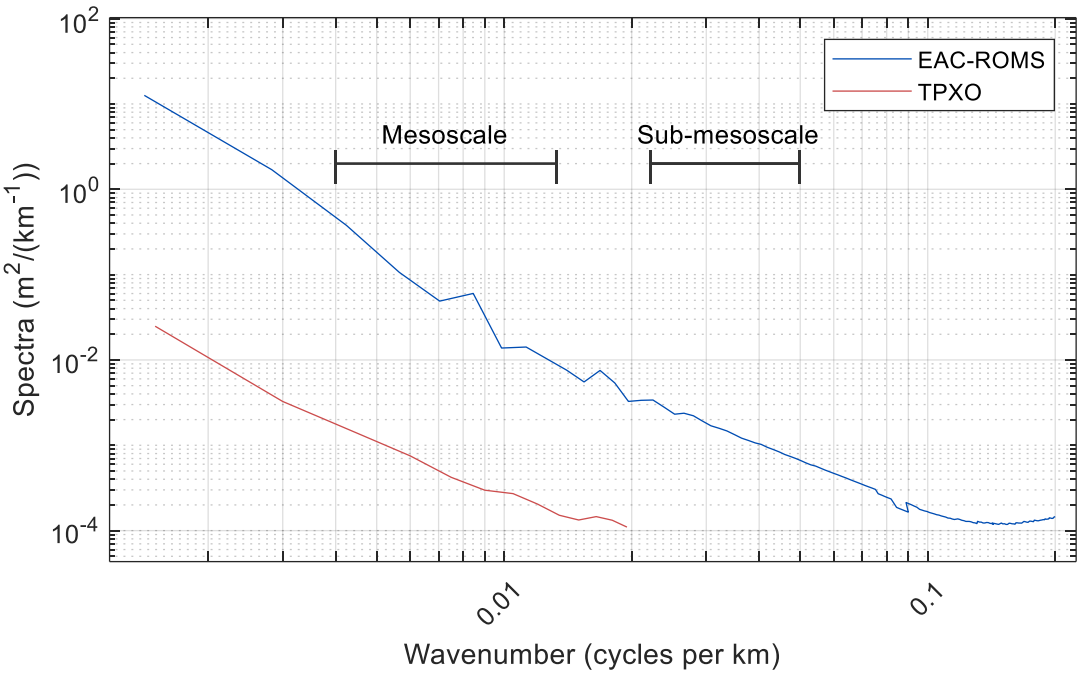

Figure 51: Wavenumber spectra of the barotropic tide from a cross-section at 27°S calculated using sea surface height from the global tide model TPXO (red line, barotropic tide) and wavenumber spectra calculated using SSH from the EAC-ROMS model (blue line, eddy field) during the time that the cyclonic eddy passed through the domain (14th June and 10th July 2012). The black horizontal bands show the range of the mesoscales (1/250 and 1/75 cycles per km) and sub-mesoscales (1/45 and 1/20 cycles per km) and highlight that the barotropic tide only has energy at wavenumber scales smaller than 1/50 cycles per km (< 0.02 cycles per km).

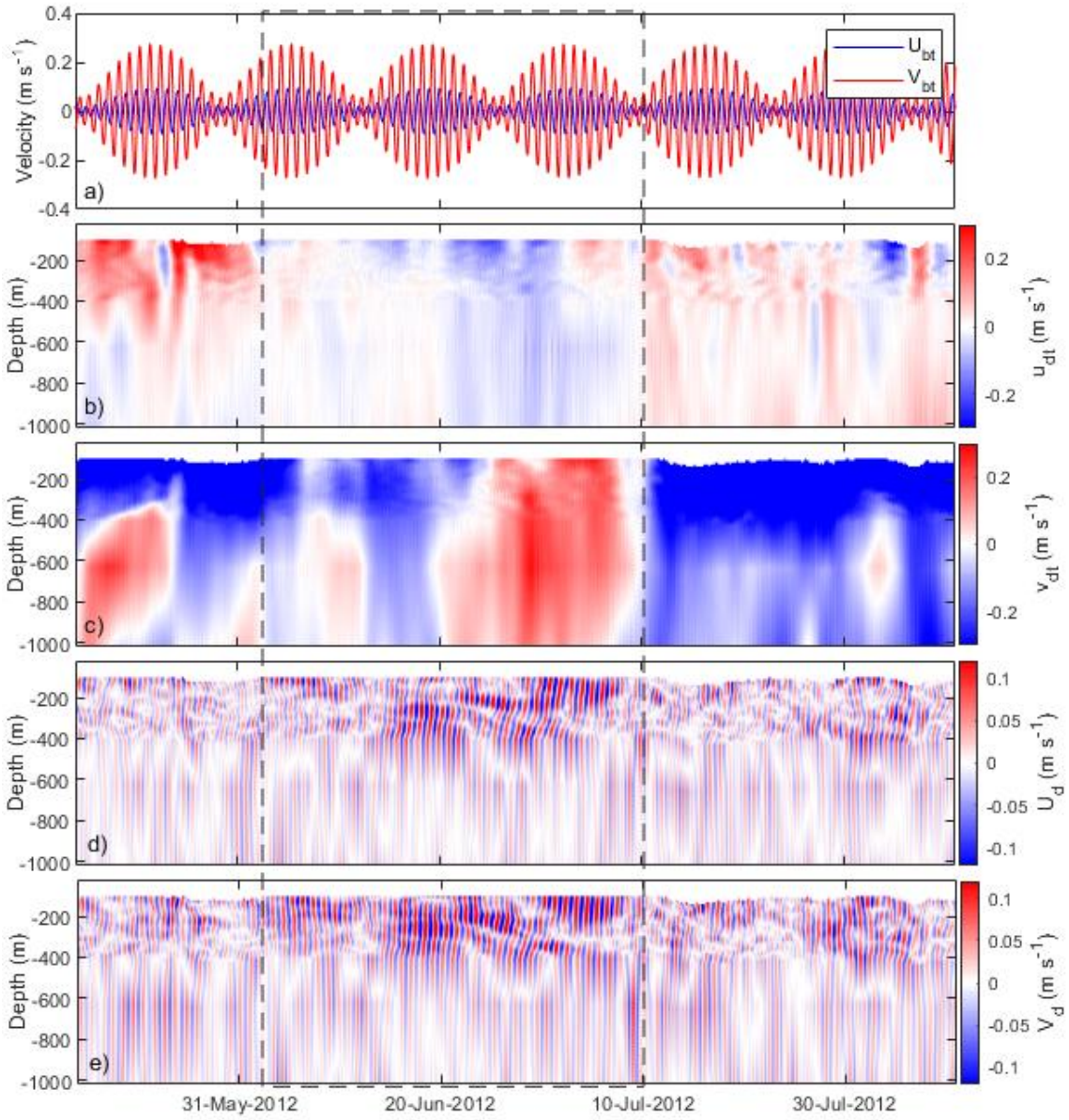

Figure 52: Time series of the velocity components, **a)** zonal (U_{bt}) and meridional (V_{bt}), of the diurnal barotropic tide calculated using TPXO model (harmonics K_1 and O_1). Detided current velocities components, **b)** zonal (u_{dt}) and **c)** meridional (v_{dt}) and velocity components of the diurnal internal tide, **d)** zonal (U_d) and **e)** meridional (V_d), observed at the mooring EAC1 (over the 1000 m isobath, EAC1). The dashed line represents the period between 5th June and 10th July 2012 that the velocity of the barotropic tide is proportional to the velocity of the current.

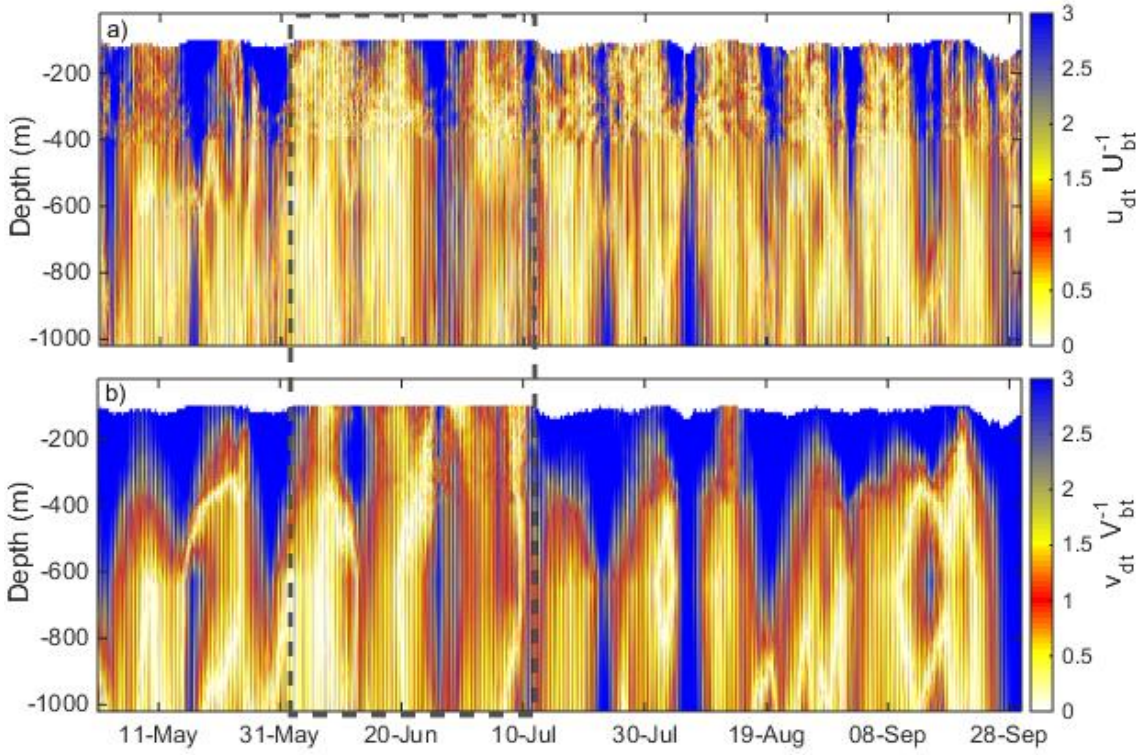

Figure 53: Time series (5 months) of the ratio of the velocities components **a)** zonal and **b)** meridional ($\frac{u_{dt}}{U_{bt}}$; $\frac{v_{dt}}{V_{bt}}$) between the detided current velocities (u_{dt} and v_{dt} Figure 52b,c) and the barotropic tide velocities (U_{bt} and V_{bt}, Figure 51a). The dashed line represents the period between 5th June and 10th July 2012 when the proportion through the water column is close to one (in red) for both, zonal and meridional components.

5.3.4 Internal Tide Characteristics

We analysed the internal tides using the velocity and temperature data from the EAC mooring array, filtered at diurnal frequency. The magnitude of the velocity of the internal tide (Figure 54c) is compared to the EKE (Figure 54b) and to the magnitude of the velocity of the barotropic tide (Figure 54a). Details of the diurnal internal tide propagation can be observed over the 1000 m isobath (mooring EAC1) where the high velocity of the internal tide (0.25 m s^{-2}) is observed at different depths from 17th June – 4th July (Figure 54c). The first and second periods are below 200 m depth suggesting that the internal tide is generated nearby, under the influence of the eddy at spring tide and propagates to the study area. The third period is related to the maximum EKE (0.33 m^2 s^{-2}) at spring tide and the internal tide is propagating from the surface suggesting that the internal tide is generated locally above the 1000 m isobath (EAC1). The velocity of propagation of the internal tide towards the bottom is ~12.2 m per day as calculated from the slope of the black dashed lines in Figure 54c.

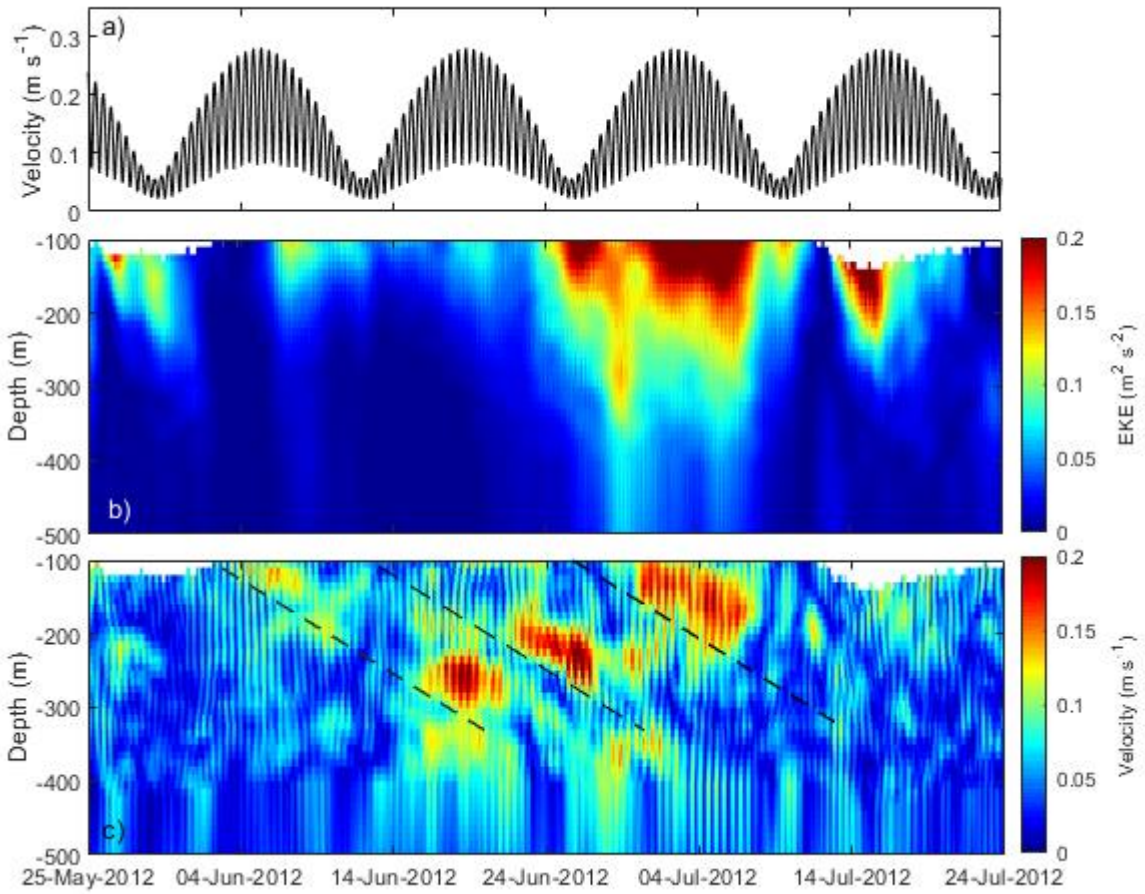

Figure 54: Time series between 24th May and 24th July 2012 of **a)** the magnitude of the horizontal velocity of the diurnal barotropic tide (from TPXO model), **b)** subtidal eddy kinetic energy (EKE) from the low pass filtered observed velocities (mooring EAC1) and **c)** magnitude of the horizontal velocity of the diurnal internal tide observed from the mooring EAC1.

The magnitude of the horizontal velocity anomaly, at diurnal band, is analysed through the water column using the mooring array data. There is an increase in the diurnal velocity near the surface, reaching 0.3 m s^{-1} on 28th June observed in the moorings SEQ200, SEQ400, EAC1, EAC2 and EAC3 (Figure 55a-e). The internal tide velocity (Figure 55) shows an increase through the water column extending to about 300 m depth (Figure 55b-e) on 5th July and near the bottom of the isobath of 200 m (mooring SEQ200, Figure 55a). Two periods of strong internal tide velocity (> 0.2 m s^{-1}) are observed between 16th and 24th June 2012 in the moorings EAC1 and EAC2 between 200 m and 300 m (Figure 55c,d). A strong diurnal velocity (> 0.2 m s^{-1}) is also observed near the bottom (150-200 m) of the 200 m isobath (mooring SEQ200) during this period (Figure 55a).

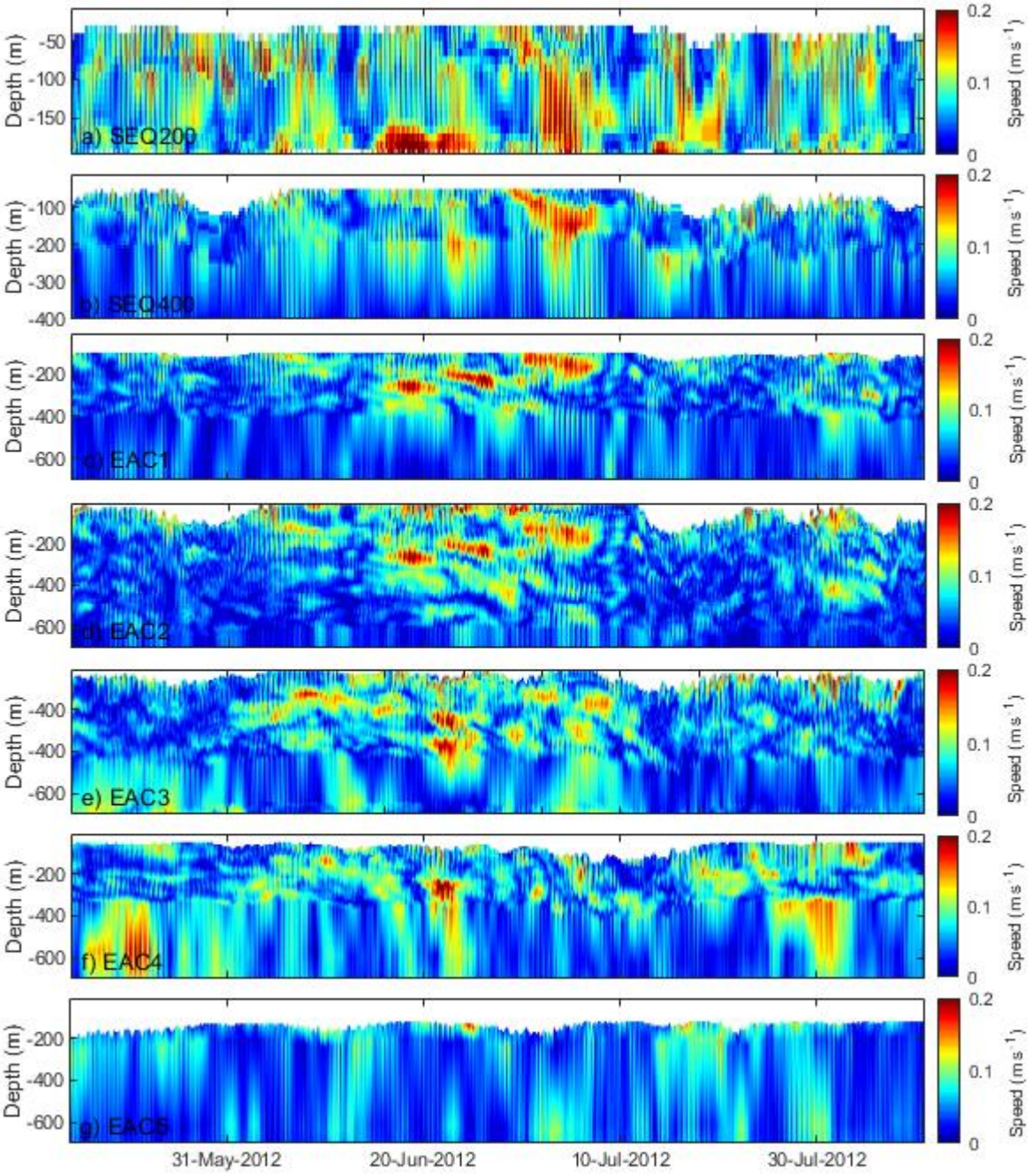

Figure 55: Time series of the magnitude of the horizontal velocity (speed) of the velocity filtered to the diurnal band. observed from the moorings SEQ200, SEQ400, EAC1, EAC2, EAC3, EAC4 and EAC5 (**a**-**g**).

Time series of temperature at 8 depths on the EAC1 mooring reveal the vertical oscillation of the internal tide (Figure 56). However, the oscillation (in the diurnal tidal band) observed at the mooring EAC1 (over the 1000 m isobath) at 123 m depth, is lower during the passage of the eddy, between 5th June and 10th July 2012, than compared to the time before (24th May) and after (14th July) the passage of the eddy (Figure 55). The oscillation of the temperature during the passage of the eddy is higher between depths of 337 and 447 m than 123 m depth. However, there is no change in the amplitude of the temperature oscillations when compared to the time before and after the passage of the eddy. The highest amplitude of the temperature oscillations during the passage of the eddy is 0.5° C at 337 m depth on 21st June 2012 (Figure 56) which is lower than the oscillation amplitude at the same depth around July 30th. The diurnal oscillations of temperature below 639 m depth are lower than 0.2° C and remain stable during the passage of the eddy.

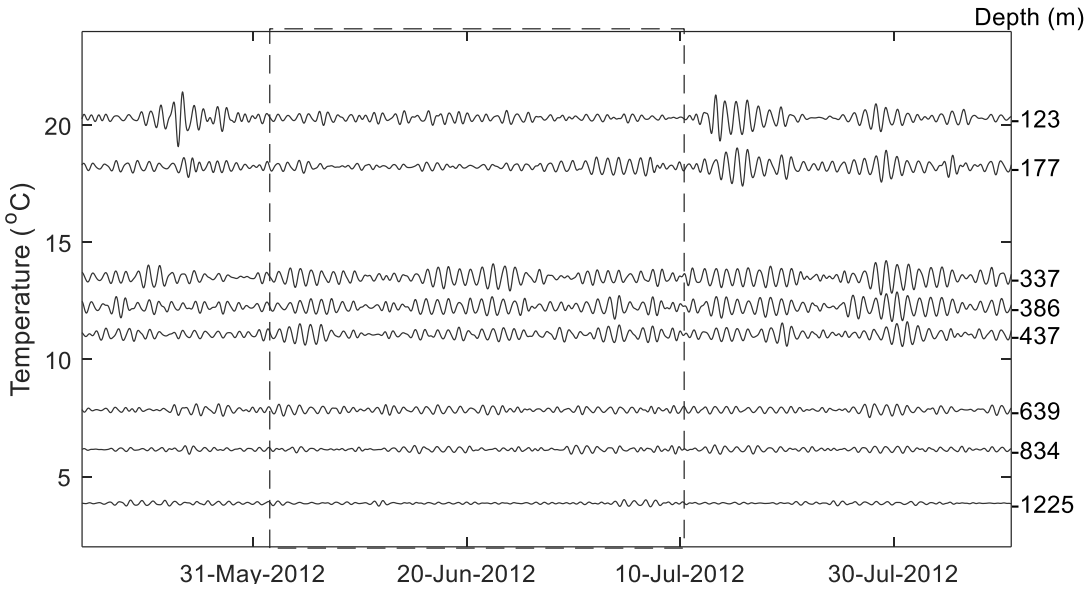

Figure 56: Time series of temperature in the diurnal tidal band through the water column observed from the mooring EAC1 over the 1000m isobath. The dashed line represents the period between 5th June and 10th July 2012.

In contrast to the case study presented in Chapter 4, in this case (Figure 57a,b) the root mean squared (RMS) of the horizontal velocities (U_d and V_d) of the diurnal internal tide are stronger than the mean between the entire period analysed, between 1st May 2012 and 1st June 2013 (Figure 18a,b). While the vertical velocity of the diurnal internal tide (Figure 57c) is lower than the mean of the entire period (Figure 18c) which indicates that it is a different mechanism of generation of the internal tide in the study area.

The horizontal velocities of the internal tide are shown to be intensified (RMS > 0.08 m s^{-1}) between 66 m and 177 m upon the passage of the eddy in the moorings SEQ400, EAC1 and EAC2 (Figure 57a,b). The intensification is shallower (66 - 144 m) in the mooring EAC3 and extends down to near the bottom over the 200 m isobath (SEQ200). The intensification of the velocity RMS (> 0.08 m s^{-1}) is limited below the isoline of N^2 = 1x10^{-4} S^{-2} and above the isoline of N^2 = 2.5 x 10-5 S^{-2} (Figure 57a,b). The uplift due to the eddy observed in the 2.5 x 10-5 S^{-2} isoline delineates the limit of the internal tide, reinforcing the influence of the eddy on the generation of the internal tide (Figure 57a,b).

Most of the vertical velocity at diurnal tidal frequency is weaker (Figure 57c) compared to the mean of the entire period analysed in Figure 18 (Chapter 3). This reinforces the idea that it is a different mechanism of generation of internal tide compared to the frontal eddies analysed in Chapter 4. The weak RMS of the vertical velocity (~ 0.01 m s^{-1}) occurs between 228 and 304 m depth over the moorings EAC1 and EAC2 and between 256 m and 288 m depth over the mooring EAC3 (Figure 57c). The isoline of N^2 = 2.5 x 10^{-5} S^{-2} also delineates the limits of the vertical velocity of the diurnal internal tide (Figure 57c).

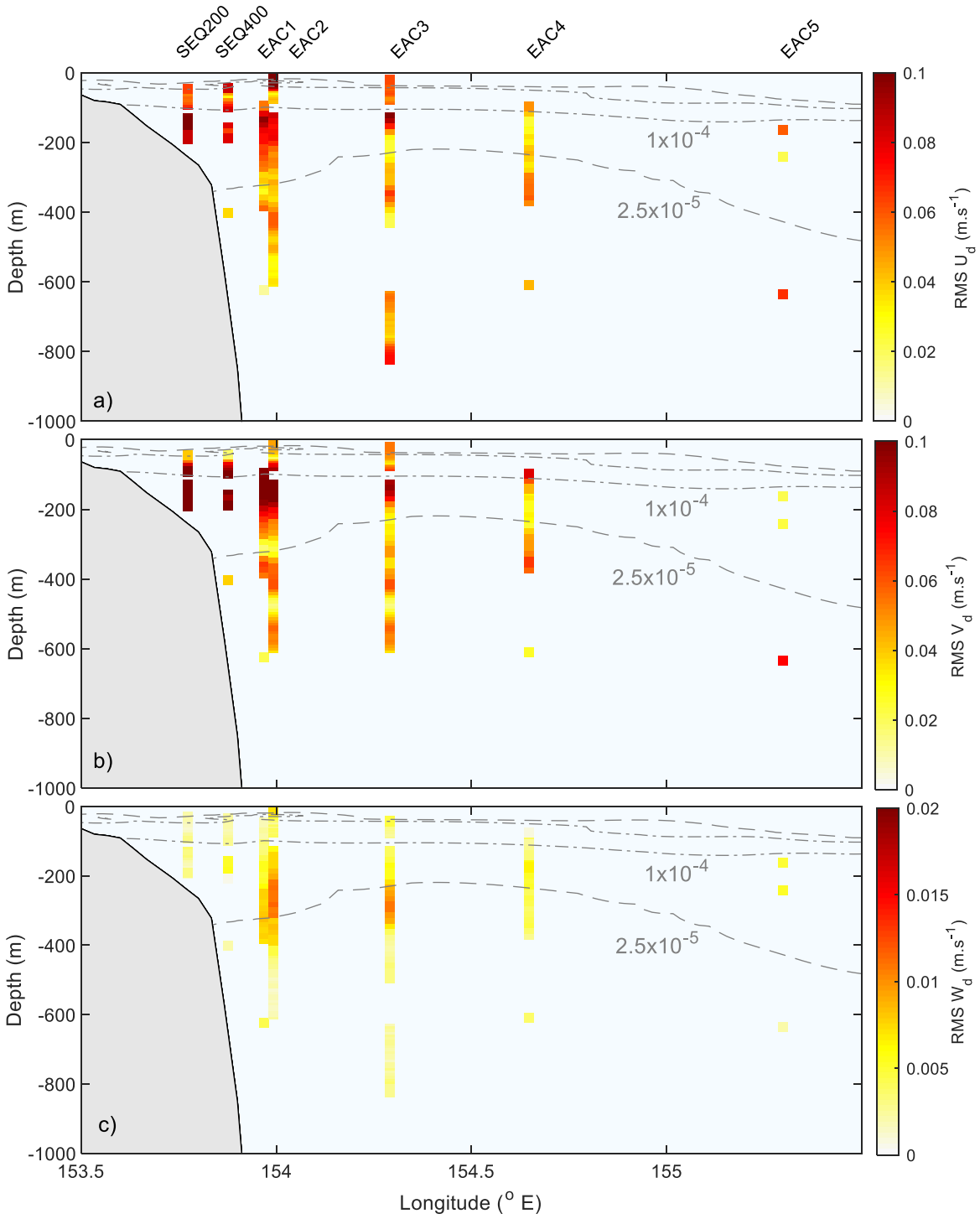

Figure 57: Cross-sections of the RMS of the velocity of the diurnal internal tide components **a)** meridional (V_d), **b)** zonal (U_d), and **c)** vertical (W_d), using velocities from the mooring array on 2nd July. The location of the moorings is in order from left to right: SEQ200, SEQ400, EAC1, EAC2, EAC3, EAC4 and EAC5 as shown in Figure 5. The dashed lines are stratification (N^2 (S^{-2})) isolines calculated from the EAC-ROMS model output.

5.3.5 Drivers of the Near-Inertial Waves

The near-inertial waves (NIWs) have several generation mechanisms, the wind blowing on the ocean surface, nonlinear wave-wave interactions, lee-wave formation by geostrophic flow over seafloor topography, and spontaneous emission through loss of balance. Wind stress is the main force that generates the NIWs in the ocean. We use the variation of the wind stress to infer about the NIWs. The wind stress observed in the study area between 5th June and 10th July is lower (< 0.003 N m^{-2}) compared to the peaks of wind stress observed between November 2012 and March 2013 when the NIWs are likely to be generated (Figure 58). There is no evidence of strong wind stress during the passage of the eddy and the wind stress is lower than 0.003 N m^{-2} (Figure 58 dashed line).

We calculate the rotary spectrum to investigate if there is evidence of the NIWs energy during the passage of the eddy, between 14th June to 10th July, (Figure 59). Since the counter-clockwise spectral density of the near-inertial wave is more energetic in the south hemisphere. The results show that the clockwise spectral density is higher than the (16x10^{-4} m^2 s^{-2} cpd^{-1}) counter-clockwise (13x10^{-4}) indicating that there is no evidence of the NIWs generation during the passage of the Eddy.

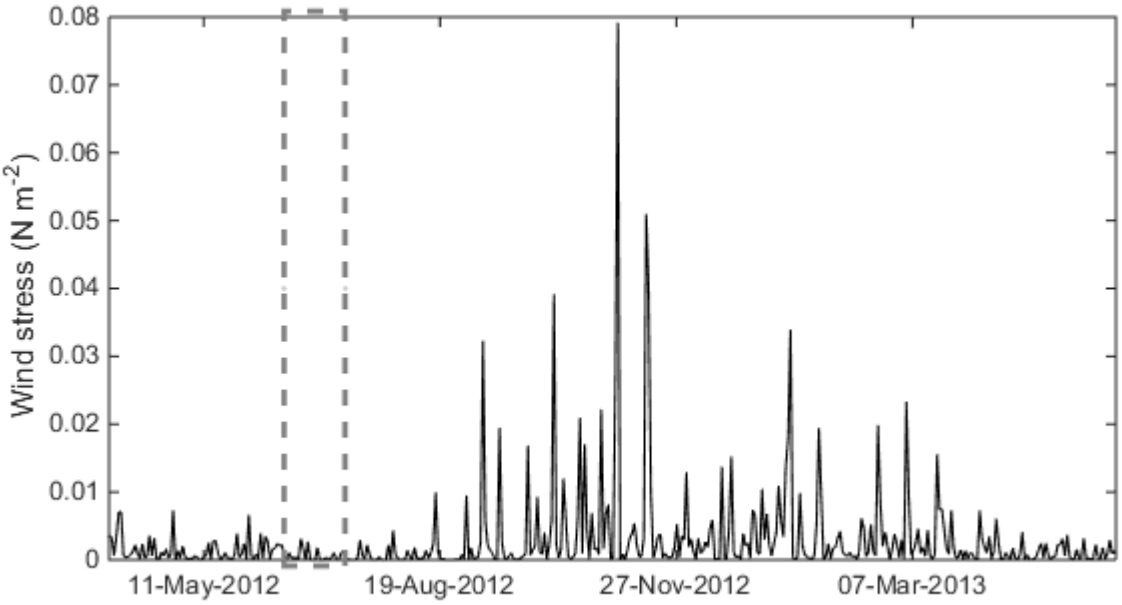

Figure 58: Time series of the observed wind stress between 1st May 2012 and 1st June 2013 collected at 10 m above the sea level at coordinates 27.53°S 153.33°E. The dashed line represents the period between 5th June and 10th July 2012 when the eddy is detected in the study area.

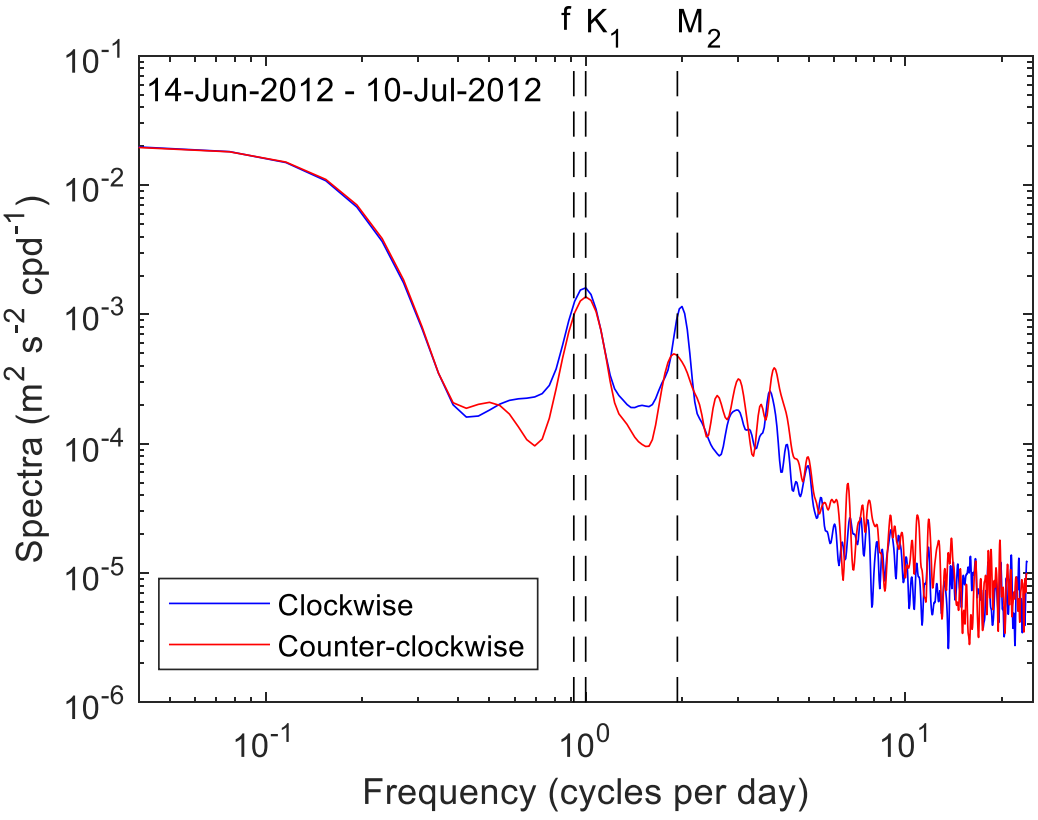

Figure 59: Rotary velocity spectrum at mooring SEQ400 (364 m) calculated during the passage of the eddy, for the period between 14th June and 10th July 2012. Blue and red represent clockwise and counter-clockwise motions, respectively. The harmonic constituents, K_1 and M_2, and near-inertial frequency (f) are plotted with a grey dashed line.

5.4 Discussion

In this chapter, we investigate if there are resonance conditions between a mesoscale cyclonic eddy and the barotropic tide that could generate internal tides in the study area. Lelong and Kunze (2013) identified this mechanism using numerical models. They conclude that the internal tide generation depends on the horizontal scales (wavenumber and velocity current) of the eddy and the barotropic tide. The best condition to generate the internal tides is if the horizontal scales of the barotropic tide is comparable to the eddy, however, this internal tide generation mechanism has not been shown observationally before.

This study presents observational evidence (to our knowledge) of a mesoscale eddy interaction with the barotropic tide that generates internal tides. We showed that the mesoscale cyclonic eddy satisfies the horizontal scales of wavenumber and the current velocity that create a resonance between the eddy and the barotropic tides. This same eddy was tracked by Ribbe and Brieva (2016) who showed that the eddy lived for about 44 days (28 May to 11 July 2012). The eddy core was located directly across the mooring array on 2nd July 2012 (Figure 46). The results show that the barotropic tide has spectral density at the same wavenumber range as the mesoscale eddy, 1/250 to 1/75 cycles per km (Figure 51). The eddy deflected the EAC core eastward to the eastern edge of the mooring array, where surface velocities were less than 0.7 m s^{-1}. This is weaker than mean EAC velocities in the core of the East Australian Current (Sloyan et al. 2016; Archer et al. 2017). The velocity of the inshore edge of the eddy, located above the continental slope, was weaker still ~ 0.3 m s^{-1} directed northward (Figures 48 and 49) and is comparable to the barotropic tide at spring tide (0.22 m s^{-1}).

This study shows an intensification of the horizontal velocity of the diurnal internal tide simultaneously with the passage of a frontal cyclonic eddy, while the temperature remains stable. The horizontal velocity of the diurnal internal tide reaches 0.2 m s^{-1} and propagates towards the bottom. This contrasts with the example of the frontal eddies propagating through the region in Chapter 4 where a strong vertical displacement (both in the vertical velocity and temperature) is observed due to an increase of the stratification above the continental slope.

In this new example here, the eddy facilitates energy transfer from the barotropic tide to the internal tide and the intensification of the internal tide (velocity) is more evident on the horizontal scales rather than vertical as predicted by Lelong and Kunze (2013).

The stratification within the eddy in this study is uplifted and asymmetric, similar to that of the mesoscale cyclonic eddy observed by Roughan et al. (2017). The internal tide limits are defined by the

stratification caused by the eddy as observed in the isolines in Figure 57 and follow the uplift of the stratification caused by the eddy (isoline $N^2 = 2.5x10^{-5}\ S^{-2}$). The higher internal tide velocity in the study area (2nd July 2012) occurs below the stratification ($N^2 >1x10^{-4}\ S^{-2}$) at about 82 m depth and above the isoline of $N^2 = 2.5x10^{-5}\ S^{-2}$, where the depth of the internal tide varies from ~ 334 to ~221 (113 m total), due to the eddy uplift.

The eddy has similar horizontal scales (wavenumber and current velocity) compared to the barotropic tide (Figures 51 and 53) and creates a resonance mechanism that generates the internal tides (Figure 54). The results show that the internal tide is generated by the surface tide under the influence of the frontal cyclonic eddy. The transfer of the energy is more effective in the horizontal parameters (zonal and meridional velocities) rather than the vertical parameters (vertical velocity and temperature) of the internal tides (Figures 56 and 57c).

Recent work has shown that a mesoscale cyclonic eddy could form or pass through the domain at 27-28°S about 10-15% of the time, or about 30-40 days per year (Sloyan pers. comm. from more recent moored data). Indeed, during the 13 months duration of this study, this was the only example of such a large cyclonic eddy passing through the domain. Hence, we suggest that this internal tide generation mechanism that while infrequent can have a significant role in mixing at the base of the water column.

Although anticyclonic eddies can also occur in the region, we hypothesise that cyclonic eddies will have a greater impact on the internal tide than anticyclonic eddies due to the magnitudes of the horizontal velocities (0.1-0.3 ms^{-1}) which is directed northward over the shelf in a cyclonic eddy. Anticyclones are typically larger and stronger in the region, with strong poleward velocities over the shelf, and thus have horizontal velocities greater than that of the barotropic tide.

The internal tides propagate horizontally and vertically toward the bottom as observed in Figure 54 and hit the continental slope (Figure 55a). A strong near-bottom velocity (~ 150-200 m), at the diurnal frequency, is observed above the continental slope at the 200 m isobath (mooring SEQ200), between 16th and 24th June 2012. This strong diurnal velocity near the bottom does not occur in the other areas located above the continental slope (isobath of 400, 1000 and 2000 m).

This turbulence can be responsible for mixing the bottom of the ocean (Munk and Wunsch 1998; Niwa and Hibiya 2011), that bring nutrients to the water column and thus affect the biological productivity (Pingree et al. 1986). The mesoscale eddy analysed here is associated with higher Chlorophyll-a due to upwelling that supplies biological productivity. The eddy increases the nutrient concentration in the water column and near the surface (Ribbe and Brieva 2016) similar to other cyclonic eddies observed in the region (Roughan et al. 2017).

Interestingly Alford et al. (2017) also investigated internal tides in the same dataset and found the depth-integrated horizontal eddy kinetic energy is a maximum in the diurnal frequency range during the same time period (see Figure 4 in Alford et al. 2017) and they attributed this to be near-inertial waves generated by storms at a higher latitude propagating towards the study area. However, no evidence of storm or wind stress were shown. The results presented here show that the horizontal velocity at the diurnal frequency is most likely forced by the local surface tide (Figure 54) rather than by the wind stress that was near 0 during the internal tide generation (Figure 58).

We have shown evidence that the interaction between a mesoscale eddy and the barotropic tide plays a role in the local internal tide generation above the continental slope of eastern Australia. Similar evidence was observed using drifters in the Subarctic Pacific Ocean where the eddy interacts with the near-inertial waves (Rogachev and Carmack 2002). This mechanism does not occur very often because of the infrequency of the cyclonic eddy generation at the appropriate scales and the mismatch in the length scales of the eddies and barotropic tides. Normally the velocity of the current under the influence of the EAC is much stronger than the barotropic tide (Figure 53). Further studies are suggested to analyse the parametric subharmonic instability of the semidiurnal internal tide. Bispectral analysis can be useful to understand the triad of waves interaction and the energy exchange and the phase relationship. Further studies are also suggested on the trapping of near-inertial waves by the vorticity of the mean currents (Rainville & Pinkel, 2004; Connolly et al. 2014) to understand if the internal wave is trapped into the eddy.

5.5 Conclusions

We conclude that a frontal cyclonic eddy and the barotropic tide have spectral density at the same mesoscale wavenumber range (1/250 to 1/75 cycles per km). The velocities of the eddy field are comparable to the barotropic tide at spring tides (about 0.2 m s^{-1}) between 5th June and 10th July 2012. The horizontal parameters of the diurnal internal tide velocity increase from near 0 to 0.2 m s^{-1} since the eddy reached the study area, while the vertical velocities and temperature remain unchanged. The spatial extent of the internal tide generation is limited by the stratification caused by the eddy, where N^2 ranges between $1x10^{-4}$ S^{-2} and $2.5x10^{-4}$ S^{-2} and the internal tide is strongest below the maximum stratification.

We show evidence that the eddy acts as a catalyst triggering interaction (energy transfer) between the barotropic tide and the internal tide. Further studies on this mechanism are suggested for conclusions and details of the interaction. This is important because the internal tide can propagate towards the

bottom and mix the stratified layers of the ocean. Moreover, the mixing near the bottom can bring nutrients to the water column that affect biological productivity.

We suggest that this mechanism does not occur very often because of the mismatch in the length scales of the eddies and barotropic tides but, it may play a role in the local internal tide generation above the continental slope of eastern Australia.

Chapter 6: Summary and Conclusions

This study has improved our understanding of the dynamics of internal tides in a vigorous western boundary current the East Australian Current (EAC) off Eastern Australia. Understanding how internal tides behave in this region is important because they can generate turbulence in the water column, leading to vertical mixing of density and erosion of stratification. Since this mixing can alter global ocean temperatures, this has implications for climate change and ocean heat content. Internal tides can also generate currents near the ocean floor, transporting nutrients up through the water column and modulating biological productivity.

For these reasons, the predictability of the internal tides is of significant practical and fundamental interest. However, their predictability can be challenging because internal tides can be generated locally or remotely. In addition, internal tides can interact with ocean circulation which can modify the background stratification that sustains the internal tide itself, and the response can be complex. In this thesis, we presented the first detailed study characterising the strength and variability, in both space and time, of the internal tide off eastern Australia (27^{o}S) deriving insight into how internal tides vary above the continental slope adjacent to the EAC. The conclusions of the research questions we addressed are:

Chapter 3

i) What are the characteristics and the origin of the diurnal and semidiurnal internal tide in a vigorous western boundary current?

The results showed that the main harmonic constituents that compose the internal tides in the study area are K_1 and O_1 (diurnal frequency) and M_2 and S_2 (semidiurnal frequency). The diurnal frequency is more energetic than the semidiurnal, with mean depth-integrated energy fluxes of the diurnal frequencies reaching 4.3 kW m^{-1} compared to 0.51 kW m^{-1} for the semidiurnal (400 m isobath). The spectral density is higher above the continental slope compared to offshore, for both the diurnal and semidiurnal frequencies, with the peak of the energy reaching 1.6°C^2/(1/days) over the 400m isobath.

The diurnal internal tides have a pronounced spring-neap tide cycle and a high coherent portion (> 70%) near the bottom indicating that the diurnal internal tide is generated locally above the continental slope. The semidiurnal internal tides, however, do not follow the spring-neap tide cycle of the barotropic tide, and they have different phases. The semidiurnal internal tide energy flux is weak, most

of the time, and we conclude that it is remotely generated. High energy flux (0.51 kW m^{-1}) of the remote semidiurnal internal tide is sporadic and occurs at neap tide.

Chapter 4

ii) How do frontal eddies influence the internal tide over the continental slope?

The results showed that the internal tide is temporally variable and the intensification of the spectral density of the diurnal internal tide is correlated to an increase in stratification near the bottom (400 m isobath), above the continental slope. Smaller (frontal) cyclonic eddies, that form on the inside edge of the EAC, with a diameter of approximately 30 km, are the main mechanism that enhances the near bottom stratification (> 0.5 x 10^{-5} s^{-2}) above the continental slope and modulates the diurnal internal tide during the study period. The intensification of the internal tides modulates the vertical displacement of the water column as observed in temperature and vertical velocity. The temperature amplitude of the internal tides reaches 1^{o} C near the bottom (400 m) with the passage of the cyclonic frontal eddies.

We suggest that this could be a common occurrence that contributes to mixing in the EAC due to the frequency with which frontal eddies have been observed in the region. Few peaks of the spectral density at diurnal frequency are not related to the local stratification. Shoaling of the internal tide and the influence of the near-inertial waves may be causing peaks in the spectral density at the diurnal frequency, and further investigation is suggested.

Chapter 5

iii) Does the interaction between mesoscale cyclonic eddies and the barotropic tide favour internal tide generation?

A case study of a mesoscale cyclonic eddy (diameter ~ 100 km) was analysed, and the velocities of the eddy field were shown to be comparable to the barotropic tide at spring tides (about 0.2 m s^{-1}). The horizontal component of the diurnal internal tide velocity increase from near 0 to 0.2 m s^{-1} as the eddy reached the study area, while the vertical velocities and temperature remain unchanged. We showed that the barotropic tide has the same wavenumber range (1/250 to 1/75 cycles per km) and velocity as the mesoscale circulation. The spatial extent of the internal tide generation is limited by the stratification caused by the eddy, where N^2 ranges between 1 x 10^{-4} S^{-2} and 2.5 x 10^{-4} S^{-2} and the internal tide is strongest below the maximum stratification. We show that the eddy may act as a catalyst triggering interaction between the barotropic tide and intensify the internal tide current horizontally, rather than vertically. This case study of one event showed that the eddy scales match with the

barotropic tide scales. The frequency of occurrence of this interaction is still unknown and further investigations are suggested. This event is related to high chlorophyll concentration indicating high primary productivity and so it is of interest.

In conclusion, this is the first comprehensive investigation into internal tides in the EAC and their interaction with eddies. This thesis showed that the locally generated diurnal internal tides are modulated by the passage of cyclonic fronts that enhance the local stratification above the continental slope and intensify the diurnal internal tides. The internal tide at the diurnal frequency can also be generated by the interaction with mesoscale eddies as a triad of waves. This mechanism does not occur very often due to the mismatch of the eddy field and barotropic tide velocities. The semidiurnal internal tides are weaker than diurnal and peaks of energy flux is observed at neap tides, which suggests that the internal tides are remotely generated coming from the distant islands of New Caledonia, Solomon Islands or Papua New Guinea as observed in global models.

This work makes a significant contribution to our understanding of the interaction of background circulation (the EAC and its eddy field) and the barotropic tide and the contribution to mixing in a vigorous western boundary current region. Studying the characteristics of internal tides and their interaction with ocean circulation helps us quantify their variability and improve their predictability, which is non-trivial in contrast to the deterministic barotropic tides that generate them.

References

Alford, M. H., 2001: Internal swell generation: The spatial distribution of energy flux from the wind to mixed layer near-inertial motions. Journal of Physical Oceanography, 31, 2359-2368, https://doi.org/10.1175/1520-0485(2001)031<2359:isgtsd>2.0.co;2.

Alford, M. H., 2003: Redistribution of energy available for ocean mixing by long-range propagation of internal waves. Nature, 423, 159, https://doi.org/10.1038/nature01628.

Alford, M. H., 2010: Sustained, Full-Water-Column Observations of Internal Waves and Mixing near Mendocino Escarpment. Journal of Physical Oceanography, 40, 2643-2660, https://doi.org/10.1175/2010jpo4502.1.

Alford, M. H., B. M. Sloyan, and H. L. Simmons, 2017: Internal Waves in the East Australian Current. Geophysical Research Letters, 44, 12,280-212,288, https://doi.org/10.1002/2017GL075246.

Alford, M. H., J. A. MacKinnon, H. L. Simmons, and J. D. Nash, 2016: Near-Inertial Internal Gravity Waves in the Ocean. Annual Review of Marine Science, 8, 95-123, https://doi.org/10.1146/annurev-marine-010814-015746.

Arbic, B. K., A. J. Wallcraft, and E. J. Metzger, 2010: Concurrent simulation of the eddying general circulation and tides in a global ocean model. Ocean Modelling, 32, 175-187, https://doi.org/10.1016/j.ocemod.2010.01.007.

Archer, M. R., M. Roughan, S. R. Keating, and A. Schaeffer, 2017: On the Variability of the East Australian Current: Jet Structure, Meandering, and Influence on Shelf Circulation. Journal of Geophysical Research: Oceans, 122, 8464-8481, https://doi.org/10.1002/2017JC013097.

Archer, M. R., S. R. Keating, M. Roughan, W. E. Johns, R. Lumpkin, F. J. Beron-Vera, and L. K. Shay, 2018: The Kinematic Similarity of Two Western Boundary Currents Revealed by Sustained High-Resolution Observations. Geophysical Research Letters, 45, 6176-6185, https://doi.org/10.1029/2018gl078429.

Armstrong, F. A., and E. C. Lafond, 1966: Chemical Nutrient Concentrations and their Relationship to Internal Waves and Turbidity off Southern California. Limnology and Oceanography, 11, 538-+, https://doi.org/10.4319/lo.1966.11.4.0538.

Baines, P. G., 1974: The Generation of Internal Tides over Steep Continental Slopes. Philosophical Transactions of the Royal Society of London. Series A, Mathematical and Physical Sciences, 277, 27-58.

Baines, P. G., 1982: On internal tide generation models. Deep Sea Research Part A. Oceanographic Research Papers, 29, 307-338, https://doi.org/10.1016/0198-0149(82)90098-X.

Boettger, D., R. Robertson, and L. Rainville, 2015: Characterizing the semidiurnal internal tide off Tasmania using glider data. Journal of Geophysical Research: Oceans, 120, 3730-3746, https://doi.org/10.1002/2015JC010711.

Bowen, M. M., J. L. Wilkin, and W. J. Emery, 2005: Variability and forcing of the East Australian Current. J. Geophys. Res.-Oceans, 110, 14, https://doi.org/10.1029/2004jc002533.

Caldwell, D. R., 1976: Fine-scale temperature structure in the bottom mixed layer on the Oregon shelf. Deep Sea Research and Oceanographic Abstracts, 23, 1025-1035, https://doi.org/10.1016/0011-7471(76)90878-0.

Cetina-Heredia, P., M. Roughan, E. van Sebille, and M. A. Coleman, 2014: Long-term trends in the East Australian Current separation latitude and eddy driven transport. Journal of Geophysical Research: Oceans, 119, 4351-4366, https://doi.org/10.1002/2014JC010071.

Chavanne, C., P. Flament, G. Carter, M. Merrifield, D. Luther, E. Zaron, and K.-W. Gurgel, 2010: The Surface Expression of Semidiurnal Internal Tides near a Strong Source at Hawaii. Part I: Observations and Numerical Predictions. Journal of Physical Oceanography, 40, 1155-1179, https://doi.org/10.1175/2010jpo4222.1.

Chuang, W. S., and D. P. Wang, 1981: Effects of Density Front on the Generation and Propagation of Internal Tides. Journal of Physical Oceanography, 11, 1357-1374, https://doi.org/10.1175/1520-0485(1981)011<1357:eodfot>2.0.co;2.

Colosi, J. A., and W. Munk, 2006: Tales of the Venerable Honolulu Tide Gauge. Journal of Physical Oceanography, 36, 967-996, https://doi.org/10.1175/jpo2876.1.

Connolly T. P., Hickey B. M., Shulman I. and Thomson R. E., 2014: Coastal Trapped Waves, Alongshore Pressure Gradients, and the California Undercurrent. Journal of Physical Oceanography, 44, 1, 319 – 342.

Cooper, L. H. N., 1947: Internal Waves and Upwelling of Oceanic Water from Mid-depths on to a Continental Shelf. Nature, 159, 579-580, https://doi.org/10.1038/159579c0.

Cowley, R., 2015: Report on the quality control of IMOS ABOS East Australian Current (EAC) Deep Water moorings array, 124 pp.

Craig, P. D., 1987: Solutions for internal tidal generation over coastal topography. Journal of Marine Research, 45, 83-105, https://doi.org/10.1357/002224087788400954.

D'Asaro, E. A., 1978: Mixed layer velocities induced by internal waves. Journal of Geophysical Research: Oceans, 83, 2437-2438, https://doi.org/10.1029/JC083iC05p02437.

DeCarlo, T. M., K. B. Karnauskas, K. A. Davis, and G. T. F. Wong, 2015: Climate modulates internal wave activity in the Northern South China Sea. Geophysical Research Letters, 42, 831-838, https://doi.org/10.1002/2014GL062522.

Duda, T. F., and Coauthors, 2004: Internal tide and nonlinear internal wave behavior at the continental slope in the northern South China Sea. Ieee Journal of Oceanic Engineering, 29, 1105-1130, https://doi.org/10.1109/joe.2004.836998.

Dunphy, M., A. L. Ponte, P. Klein, and S. Le Gentil, 2017: Low-Mode Internal Tide Propagation in a Turbulent Eddy Field. Journal of Physical Oceanography, 47, 649-665, https://doi.org/10.1175/jpo-d-16-0099.1.

Dushaw, B. D., B. D. Cornuelle, P. F. Worcester, B. M. Howe, and D. S. Luther, 1995: Barotropic and Baroclinic Tides in the Central North Pacific-Ocean Determined from Long-Range Reciprocal Acoustic Transmissions. Journal of Physical Oceanography, 25, 631-647, https://doi.org/10.1175/1520-0485(1995)025<0631:babtit>2.0.co;2.

Eckart, C., 1961: Internal Waves in the Ocean. The Physics of Fluids, 4, 791-799, https://doi.org/10.1063/1.1706408.

Egbert, G. D., and R. D. Ray, 2000: Significant dissipation of tidal energy in the deep ocean inferred from satellite altimeter data. Nature, 405, 775-778, https://doi.org/10.1038/35015531.

Egbert, G. D., and S. Y. Erofeeva, 2002: Efficient Inverse Modeling of Barotropic Ocean Tides. Journal of Atmospheric and Oceanic Technology, 19, 183-204, https://doi.org/10.1175/1520-0426(2002)019<0183:EIMOBO>2.0.CO;2.

Everett, J. D., M. E. Baird, and I. M. Suthers, 2011: Three-dimensional structure of a swarm of the salp Thalia democratica within a cold-core eddy off southeast Australia. Journal of Geophysical Research: Oceans, 116, https://doi.org/10.1029/2011JC007310.

Everett, J. D., H. Macdonald, M. E. Baird, J. Humphries, M. Roughan, and I. M. Suthers, 2015: Cyclonic entrainment of preconditioned shelf waters into a frontal eddy. Journal of Geophysical Research: Oceans, 120, 677-691, https://doi.org/10.1002/2014JC010301.

Farmer, D. M., M. H. Alford, R. C. Lien, Y. J. Yang, M. H. Chang, and Q. Li, 2011: From Luzon Strait to Dongsha Plateau: Stages in the Life of an Internal Wave. Oceanography, 24, 64-77.

Fu, L. L., 1981: Observations and Models of Inertial Waves in the Deep Ocean. Reviews of Geophysics, 19, 141-170, https://doi.org/10.1029/RG019i001p00141.

Garrett, C., and W. Munk, 1972: Oceanic mixing by breaking internal waves. Deep Sea Research and Oceanographic Abstracts, 19, 823-832, https://doi.org/10.1016/0011-7471(72)90001-0.

Garrett, C., and W. Munk, 1975: Space-time scales of internal waves: A progress report. Journal of Geophysical Research (1896-1977), 80, 291-297, https://doi.org/10.1029/JC080i003p00291.

Garrett, C., and W. Munk, 1979: Internal Waves in the Ocean. Annu. Rev. Fluid Mech., 11, 339-369, https://doi.org/10.1146/annurev.fl.11.010179.002011.

Gayen, B., and S. Sarkar, 2011: Direct and large-eddy simulations of internal tide generation at a near-critical slope. Journal of Fluid Mechanics, 681, 48-79, https://doi.org/10.1017/jfm.2011.170.

Gemmrich, J. R., and H. van Haren, 2002: Internal wave band eddy fluxes above a continental slope. Journal of Marine Research, 60, 227-253, https://doi.org/10.1357/00222400260497471.

Gerkema, T., and J. T. F. Zimmerman, 2008: An Introduction to Internal Waves. Royal NIOZ, 207 pp.

Gibbs, M. T., and J. H. Middleton, 1997: Barotropic and baroclinic tides on the Sydney continental shelf. Continental Shelf Research, 17, 1005-1027, https://doi.org/10.1016/s0278-4343(97)00004-6.

Gill, A. E., 1982: Atmosphere -Ocean Dynamics. Vol. 30, 662 pp.

Gregg, M. C., and M. G. Briscoe, 1979: Internal Waves, Finestructure, Microstructure, and Mixing in the Ocean. Reviews of Geophysics, 17, 1524-1548, https://doi.org/10.1029/RG017i007p01524.

Griffin, D., J. Middleton, and L. Bode, 1987: The tidal and longer-period circulation of Capricornia, Southern Great Barrier Reef. Marine and Freshwater Research, 38, 461-474, https://doi.org/10.1071/MF9870461.

Griffiths, S. D., and R. H. J. Grimshaw, 2007: Internal Tide Generation at the Continental Shelf Modeled Using a Modal Decomposition: Two-Dimensional Results. Journal of Physical Oceanography, 37, 428-451, https://doi.org/10.1175/jpo3068.1.

Hamon, B. V., 1965: The East Australian current, 1960–1964. Deep Sea Research and Oceanographic Abstracts, 12, 899-921, http://dx.doi.org/10.1016/0011-7471(65)90813-2.

Haurwitz, B., 1948: The Effect of Ocean Currents on Internal Waves. Journal of Marine Research, 7, 217-228.

Holloway, P. E., and M. A. Merrifield, 1999: Internal tide generation by seamounts, ridges, and islands. Journal of Geophysical Research: Oceans, 104, 25937-25951, https://doi.org/10.1029/1999JC900207.

Huang, X. D., and Coauthors, 2018: Role of Mesoscale Eddies in Modulating the Semidiurnal Internal Tide: Observation Results in the Northern South China Sea. Journal of Physical Oceanography, 48, 1749-1770, https://doi.org/10.1175/jpo-d-17-0209.1.

Ismail, M. F. A., J. Ribbe, J. Karstensen, C. Lemckert, S. Lee, and J. Gustafson, 2017: The Fraser Gyre: A cyclonic eddy off the coast of eastern Australia. Estuarine, Coastal and Shelf Science, 192, 72-85, https://doi.org/10.1016/j.ecss.2017.04.031.

Jeon, C., and Coauthors, 2014: Seasonal variation of semidiurnal internal tides in the East/Japan Sea. Journal of Geophysical Research: Oceans, 119, 2843-2859, https://doi.org/10.1002/2014JC009864.

Jithin, A. K., and P. A. Francis, 2020: Role of internal tide mixing in keeping the deep Andaman Sea warmer than the Bay of Bengal. Sci Rep, 10, 10, https://doi.org/10.1038/s41598-020-68708-6.

Johnston, T. M. S., and D. L. Rudnick, 2015: Trapped diurnal internal tides, propagating semidiurnal internal tides, and mixing estimates in the California Current System from sustained glider observations, 2006–2012. Deep Sea Research Part II: Topical Studies in Oceanography, 112, 61-78, http://dx.doi.org/10.1016/j.dsr2.2014.03.009.

Katsumata, K., S. E. Wijffels, C. R. Steinberg, and R. Brinkman, 2010: Variability of the semidiurnal internal tides observed on the Timor Shelf. Journal of Geophysical Research: Oceans, 115, https://doi.org/10.1029/2009JC006071.

Kelly, S. M., and J. D. Nash, 2010: Internal-tide generation and destruction by shoaling internal tides. Geophysical Research Letters, 37, https://doi.org/10.1029/2010GL045598.

Kerry, C., M. Roughan, and B. Powell, 2018: Observation Impact in a Regional Reanalysis of the East Australian Current System. Journal of Geophysical Research: Oceans, 123, 7511-7528, https://doi.org/doi:10.1029/2017JC013685.

Kerry, C., M. Roughan, and B. Powell, 2020: Predicting the submesoscale circulation inshore of the East Australian Current. Journal of Marine Systems, 204, 103286, https://doi.org/10.1016/j.jmarsys.2019.103286.

Kerry, C., B. Powell, M. Roughan, and P. Oke, 2016: Development and evaluation of a high-resolution reanalysis of the East Australian Current region using the Regional Ocean Modelling System (ROMS 3.4) and Incremental Strong-Constraint 4-Dimensional Variational (IS4D-Var) data assimilation. Geoscientific Model Development, 9, 3779-3801, https://doi.org/10.5194/gmd-9-3779-2016.

Kerry, C. G., B. S. Powell, and G. S. Carter, 2013: Effects of Remote Generation Sites on Model Estimates of M2 Internal Tides in the Philippine Sea*. Journal of Physical Oceanography, 43, 187-204, https://doi.org/10.1175/JPO-D-12-081.1.

Kerry, C. G., B. S. Powell, and G. S. Carter, 2014: The Impact of Subtidal Circulation on Internal Tide Generation and Propagation in the Philippine Sea. Journal of Physical Oceanography, 44, 1386-1405, https://doi.org/10.1175/JPO-D-13-0142.1.

Klymak, J. M., and Coauthors, 2016: Reflection of Linear Internal Tides from Realistic Topography: The Tasman Continental Slope. Journal of Physical Oceanography, 46, 3321-3337, https://doi.org/10.1175/jpo-d-16-0061.1.

Large, W. G., and S. Pond, 1981: Open Ocean Momentum Flux Measurements in Moderate to Strong Winds. Journal of Physical Oceanography, 11, 324-336, https://doi.org/10.1175/1520-0485(1981)011<0324:oomfmi>2.0.co;2.

Lee, T. N., 1975: Florida Current Spin-Off Eddies. Deep-Sea Research, 22, 753-765, https://doi.org/10.1016/0011-7471(75)90080-7.

Lelong, M. P., and E. Kunze, 2013: Can barotropic tide-eddy interactions excite internal waves? Journal of Fluid Mechanics, 721, 1-27, https://doi.org/10.1017/jfm.2013.1.

Lim, K., G. N. Ivey, and N. L. Jones, 2010: Experiments on the generation of internal waves over continental shelf topography. Journal of Fluid Mechanics, 663, 385-400, https://doi.org/10.1017/S002211201000354X.

Liu, J., Y. He, D. Wang, T. Liu, and S. Cai, 2015: Observed enhanced internal tides in winter near the Luzon Strait. Journal of Geophysical Research: Oceans, 120, 6637-6652, https://doi.org/10.1002/2015JC011131.

Macdonald, H. S., M. Roughan, M. E. Baird, and J. Wilkin, 2016: The formation of a cold-core eddy in the East Australian Current. Continental Shelf Research, 114, 72-84, https://doi.org/10.1016/j.csr.2016.01.002.

MacKinnon, J., 2013: Mountain waves in the deep ocean. Nature, 501, 321-322, https://doi.org/10.1038/501321a.

Martini, K. I., M. H. Alford, S. M. Kelly, and J. D. Nash, 2011: Observations of Internal Tides on the Oregon Continental Slope. Journal of Physical Oceanography, 41, 1772-1794, https://doi.org/10.1175/2011jpo4581.1.

Martini, K. I., M. H. Alford, E. Kunze, S. M. Kelly, and J. D. Nash, 2013: Internal Bores and Breaking Internal Tides on the Oregon Continental Slope. Journal of Physical Oceanography, 43, 120-139, https://doi.org/10.1175/jpo-d-12-030.1.

Mata, M. M., S. E. Wijffels, J. A. Church, and M. Tomczak, 2006: Eddy shedding and energy conversions in the East Australian Current. J. Geophys. Res.-Oceans, 111, 18, https://doi.org/10.1029/2006jc003592.

Maze, R., 1987: Generation and Propagation of Nonlinear Internal Waves Induced by the Tide Over a Continental-Slope. Continental Shelf Research, 7, 1079-1104, https://doi.org/10.1016/0278-4343(87)90100-2.

Mazloff, M. R., B. Cornuelle, S. T. Gille, and J. B. Wang, 2020: The Importance of Remote Forcing for Regional Modeling of Internal Waves. J. Geophys. Res.-Oceans, 125, https://doi.org/10.1029/2019jc015623.

Middleton, J. H., D. Cox, and P. Tate, 1996: The oceanography of the Sydney region. Marine Pollution Bulletin, 33, 124-131, http://dx.doi.org/10.1016/S0025-326X(96)00170-1.

Mooers, C.N.K. (1973). A technique for the cross-spectrum analysis of pairs of complex-valued time series, with emphasis on properties of polarized components and rotational invariants. Deep Sea Research and Oceanographic Abstracts 20, 1129-1141. https://doi.org/10.1016/0011-7471(73)90027-2.

Munk, W., and C. Wunsch, 1998: Abyssal recipes II: energetics of tidal and wind mixing. Deep-Sea Research Part I-Oceanographic Research Papers, 45, 1977-2010, https://doi.org/10.1016/s0967-0637(98)00070-3.

Munk, W. H., 1941: Internal waves in the Gulf of California. Journal of Marine Research, 4, 81-91.

Munk, W. H., 1950: Origin and Generation of Waves. Proceedings 1st International Conference on Coastal Engineering, Long Beach, California, ASCE, 1-4.

Nan, F., H. Xue, F. Chai, L. Shi, M. Shi, and P. Guo, 2011: Identification of different types of Kuroshio intrusion into the South China Sea. Ocean Dynamics, 61, 1291-1304, https://doi.org/10.1007/s10236-011-0426-3.

Nash, J. D., M. H. Alford, and E. Kunze, 2005: Estimating Internal Wave Energy Fluxes in the Ocean. Journal of Atmospheric and Oceanic Technology, 22, 1551-1570, https://doi.org/10.1175/jtech1784.1.

Nash, J. D., S. M. Kelly, E. L. Shroyer, J. N. Moum, and T. F. Duda, 2012: The Unpredictable Nature of Internal Tides on Continental Shelves. Journal of Physical Oceanography, 42, 1981-2000, https://doi.org/10.1175/JPO-D-12-028.1.

Nikurashin, M., and R. Ferrari, 2013: Overturning circulation driven by breaking internal waves in the deep ocean. Geophysical Research Letters, 40, 3133-3137, https://doi.org/10.1002/grl.50542.

Niwa, Y., and T. Hibiya, 2011: Estimation of baroclinic tide energy available for deep ocean mixing based on three-dimensional global numerical simulations. Journal of Oceanography, 67, 493-502, https://doi.org/10.1007/s10872-011-0052-1.

Oke, P. R., and D. A. Griffin, 2011: The cold-core eddy and strong upwelling off the coast of New South Wales in early 2007. Deep Sea Research Part II: Topical Studies in Oceanography, 58, 574-591, https://doi.org/10.1016/j.dsr2.2010.06.006.

Oke, P. R., and Coauthors, 2019: Revisiting the circulation of the East Australian Current: Its path, separation, and eddy field. Progress in Oceanography, 176, 102139, https://doi.org/10.1016/j.pocean.2019.102139.

Olbers, D. J., 1981: The Propagation of Internal Waves in a Geostrophic Current. Journal of Physical Oceanography, 11, 1224-1233, https://doi.org/10.1175/1520-0485(1981)011<1224:tpoiwi>2.0.co;2.

Pawlowicz, R., B. Beardsley, and S. Lentz, 2002: Classical tidal harmonic analysis including error estimates in MATLAB using T_TIDE. Computers & Geosciences, 28, 929-937, http://dx.doi.org/10.1016/S0098-3004(02)00013-4.

Pingree, R. D., G. T. Mardell, and A. L. New, 1986: Propagation of internal tides from the upper slopes of the Bay of Biscay. Nature, 321, 154-158.

Polzin, K., 2010: Mesoscale Eddy-Internal Wave Coupling. Part II: Energetics and Results from PolyMode. Journal of Physical Oceanography, 40, 789-801 https://doi.org/10.1175/2009JPO4039.1.

Prinsenberg, S. J., and M. Rattray, 1975: Effects of Continental Slope and Variable Brunt-Vaisala Frequency on Coastal Generation of Internal Tides. Deep-Sea Research, 22, 251-263, https://doi.org/10.1016/0011-7471(75)90030-3.

Rainville, L., and R. Pinkel, 2004: Observations of energetic high wavenumber internal waves in the Kuroshio. Journal of Physical Oceanography,34, 1495–1505, https://doi.org/10.1175/1520-0485(2004) 034,1495:OOEHIW.2.0.CO;2.

Rayson, M. D., G. N. Ivey, N. L. Jones, M. J. Meuleners, and G. W. Wake, 2011: Internal tide dynamics in a topographically complex region: Browse Basin, Australian North West Shelf. J. Geophys. Res.-Oceans, 116, https://doi.org/10.1029/2009jc005881.

Ribbat, N., M. Roughan, B. Powell, S. Rao, and C. G. Kerry, 2020: Transport variability over the Hawkesbury Shelf (31.5–34.5°S) driven by the East Australian Current. PLOS ONE, 15, e0241622, https://doi.org/10.1371/journal.pone.0241622.

Ribbe, J., and D. Brieva, 2016: A western boundary current eddy characterisation study. Estuarine, Coastal and Shelf Science, 183, 203-212, https://doi.org/10.1016/j.ecss.2016.10.036.

Ridgway, K. R., R. C. Coleman, R. J. Bailey, and P. Sutton, 2008: Decadal variability of East Australian Current transport inferred from repeated high-density XBT transects, a CTD survey and satellite altimetry. Journal of Geophysical Research: Oceans, 113, https://doi.org/10.1029/2007JC004664.

Rigozo, N. R., E. Echer, D. J. R. Nordemann, L. E. A. Vieira, and H. H. de Faria, 2005: Comparative study between four classical spectral analysis methods. Applied Mathematics and Computation, 168, 411-430, https://doi.org/10.1016/j.amc.2004.09.031.

Robertson, R., J. Dong, and P. Hartlipp, 2017: Diurnal Critical Latitude and the Latitude Dependence of Internal Tides, Internal Waves, and Mixing Based on Barcoo Seamount. Journal of Geophysical Research: Oceans, 122, 7838-7866, https://doi.org/10.1002/2016JC012591.

Roder, C., L. Fillinger, C. Jantzen, G. M. Schmidt, S. Khokiattiwong, and C. Richter, 2010: Trophic response of corals to large amplitude internal waves. Marine Ecology Progress Series, 412, 113-128, https://doi.org/10.3354/meps08707.

Rocha, C.B., Chereskin, T.K., Gille, S.T., and Menemenlis, D., 2016: Mesoscale to Submesoscale Wavenumber Spectra in Drake Passage. Journal of Physical Oceanography 46**,** 601-620, https://doi.org/10.1175/jpo-d-15-0087.1.

Rogachev, K. A., and E. C. Carmack, 2002: Evidence for the trapping and amplification of near-inertial motions in a large anticyclonic ring in the Oyashio. Journal of Oceanography, 58, 673-682, https://doi.org/10.1023/a:1022842306586.

Roughan, M., H. S. Macdonald, M. E. Baird, and T. M. Glasby, 2011: Modelling coastal connectivity in a Western Boundary Current: Seasonal and inter-annual variability. Deep Sea Research Part II: Topical Studies in Oceanography, 58, 628-644, https://doi.org/10.1016/j.dsr2.2010.06.004.

Roughan, M., and Coauthors, 2017: A tale of two eddies: The biophysical characteristics of two contrasting cyclonic eddies in the East Australian Current System. Journal of Geophysical Research: Oceans, 122, 2494-2518, https://doi.org/10.1002/2016JC012241.

Rudnick, D. L., and Coauthors, 2003: From Tides to Mixing Along the Hawaiian Ridge. Science, 301, 355-357, https://doi.org/10.1126/science.1085837.

Rykova, T., and P. R. Oke, 2015: Recent freshening of the East Australian Current and its eddies. Geophysical Research Letters, 42, 9369-9378, https://doi.org/10.1002/2015gl066050.

Schaeffer, A., M. Roughan, and J. E. Wood, 2014: Observed bottom boundary layer transport and uplift on the continental shelf adjacent to a western boundary current. Journal of Geophysical Research: Oceans, 119, 4922-4939, https://doi.org/10.1002/2013JC009735.

Schaeffer, A., A. Gramoulle, M. Roughan, and A. Mantovanelli, 2017: Characterizing frontal eddies along the East Australian Current from HF radar observations. Journal of Geophysical Research: Oceans, https://doi.org/10.1002/2016JC012171.

Seiwell, H. R., 1941: Summary of some results of internal wave investigations in the North Atlantic. Transactions-American Geophysical Union, 22, 494-498.

Shchepetkin, A. F., and J. C. McWilliams, 2005: The regional oceanic modeling system (ROMS): a split-explicit, free-surface, topography-following-coordinate oceanic model. Ocean Modelling, 9, 347-404, https://doi.org/10.1016/j.ocemod.2004.08.002.

Shriver, J., B. Arbic, J. Richman, R. Ray, E. Metzger, A. Wallcraft, and P. Timko, 2012: An evaluation of the barotropic and internal tides in a high-resolution global ocean circulation model. Journal of Geophysical Research. Oceans, 117, https://doi.org/10.1029/2012JC008170.

Sloyan, B. M., K. R. Ridgway, and R. Cowley, 2016: The East Australian Current and Property Transport at 27°S from 2012 to 2013. Journal of Physical Oceanography, 46, 993-1008, https://doi.org/10.1175/JPO-D-15-0052.1.

Stokes, G. G., 1847: On the theory of oscillatory waves. Transactions of the Cambridge Philosophical Society, 8, 441.

Storlazzi, C. D., O. M. Cheriton, R. van Hooidonk, Z. X. Zhao, and R. Brainard, 2020: Internal tides can provide thermal refugia that will buffer some coral reefs from future global warming. Sci Rep, 10, 9, https://doi.org/10.1038/s41598-020-70372-9.

Stride, A. H., and M. J. Tucker, 1960: Internal Waves and Waves of Sand. Nature, 188, 933-933.

Thorpe, S. A., 1992: The Generation of Internal Waves by Flow over the Rough Topography of a Continental Slope. Proceedings: Mathematical and Physical Sciences, 439, 115-130 https://doi.org/10.1098/rspa.1992.0137.

Townsend, A. A., 1965: Excitation of Internal Waves by a Turbulent Boundary Layer. Journal of Fluid Mechanics, 22, 241-252, https://doi.org/10.1017/s002211206500071x.

Vallis, G. K., 2017: Atmospheric and Oceanic Fluid Dynamics: Fundamentals and Large-Scale Circulation. 2 ed. Cambridge University Press.

Wang, X., S. Peng, Z. Liu, R. X. Huang, Y.-K. Qian, and Y. Li, 2016: Tidal Mixing in the South China Sea: An Estimate Based on the Internal Tide Energetics. Journal of Physical Oceanography, 46, 107-124, https://doi.org/10.1175/jpo-d-15-0082.1.

Wood, J. E., A. Schaeffer, M. Roughan, and P. M. Tate, 2016: Seasonal variability in the continental shelf waters off southeastern Australia: Fact or fiction? Continental Shelf Research, 112, 92-103, https://doi.org/10.1016/j.csr.2015.11.006.

Wunsch, C., 2000: Moon, tides and climate. Nature, 405, 743-744, https://doi.org/10.1038/35015639.

Zavala-Garay, J., J. L. Wilkin, and H. G. Arango, 2012: Predictability of Mesoscale Variability in the East Australian Current Given Strong-Constraint Data Assimilation. Journal of Physical Oceanography, 42, 1402-1420, https://doi.org/10.1175/JPO-D-11-0168.1.

Zhao, Z. X., M. H. Alford, J. B. Girton, L. Rainville, and H. L. Simmons, 2016: Global Observations of Open-Ocean Mode-1 M-2 Internal Tides. Journal of Physical Oceanography, 46, 1657-1684, https://doi.org/10.1175/jpo-d-15-0105.1.